Spring 2009

Fatigue of friction stir welded lap joints with sealants

Kenneth Doering

Department:

FATIGUE OF FRICTION STIR WELDED LAP JOINTS WITH SEALANTS

by

KENNETH THOMAS NATHANIEL DOERING

A THESIS

Presented to the Faculty of the Graduate School of the

MISSOURI UNIVERSITY OF SCIENCE AND TECHNOLOGY

In Partial Fulfillment of the Requirements for the Degree

MASTER OF SCIENCE IN METALLURGICAL ENGINEERING

2009

Approved by

D. C. Van Aken, Advisor
K. Chandrashekhara
M. J. O'Keefe
M. E. Schlesinger

ABSTRACT

A lack of understanding of corrosion fatigue in friction stir welded aluminum joints prevents friction stir welding from being implemented in aerospace applications. Fatigue testing reveals a 60-75 % reduction in the fatigue life of friction stir welded aluminum lap joints immersed in 3.5 % NaCl solution (corrosion fatigue) compared with that of lap joints tested in ambient air. The loss in fatigue life is attributed to accelerated fatigue cracking due to hydrogen environment embrittlement. Two polymer sealant candidates are investigated: silicone rubber and nylon-11. Both sealant candidates can be applied prior to welding and seal the faying surface gaps in lap joints upon welding. The rubber sealant cures at room temperature after welding and can be welded with the same parameters as without the sealant. The 50 % sample population corrosion fatigue life is increased by 22 % with the use of the rubber sealant, but the effectiveness of the rubber sealant is limited by its cohesive mechanical properties, e.g. elongation to failure. In ambient fatigue, the nylon sealed welds exhibit twice the 50 % sample population fatigue life of other welds. Finite element modeling predicts a reduction in the stresses in the weld due the stiffness contribution of the nylon sealant. The effectiveness of the nylon sealant is limited by its adhesive bond strength. When immersed in water, as in corrosion fatigue, the adhesive bond strength is reduced, the sealant bond fails within 500 fatigue cycles, and the mechanical benefits of the nylon sealant are negated. The corrosion fatigue life of nylon sealed welds is 26 % less than that of welds without sealant because of the more severe hook defect associated with hotter welding conditions required to melt the nylon. Finite element modeling results indicate an increase in stress intensity factors of about 10 % in welds with more severe hook defects.

ACKNOWLEDGEMENTS

I would like to gratefully acknowledge the Center for Aerospace Manufacturing Technologies operating under the Air Force Research Lab contract no. FA8650-04-C-5704 for providing funding for the project on which this thesis is based. I would especially like to thank my advisor, Dr. David C. Van Aken, for his guidance, advice, encouragement, and particularly for his confidence in me. Richard J. Lederich from the Boeing Company deserves special acknowledgment for sharing his experience, clarifying much of my confusion, and serving as an additional advisor particularly with regards to friction stir welding. I would also like to thank the friction stir welding operators at the Boeing Company, Chris Weingart and Herb Bommer.

I would like to thank Dr. Thomas Schuman and Dr. William Fahrenholtz for their advice and technical discussion, Dr. Matthew O'Keefe for the use of his labs and his role as a committee member, Dr. Schlesinger and Dr. Chandrashekhara also for serving as committee members, and Eric Bohannan for conducting the differential scanning calorimetry experiments. I would also like to thank Jack Jones, Nathanial Inskip, and Jimmie Taylor in the machine shop for their frequent assistance and Nicholas Batts, an undergraduate research assistant, for his help in specimen preparation and fabrication of custom equipment. Other students who have helped me in various ways include William Peach, Ravi Mokirala, Jared Teague, Maj. Ryan Howell, Edward Druschitz, Steven Webb, and Manasij Yadava. I would like to mention the contributions from students previously on this project including Yoshi Kato, Zach Royer, and Brandon Brinkmeyer.

My wife deserves special mention. Her patience, love, prayers and support all these months have been priceless and very encouraging and likely to what my persevering sanity can be attributed. Lastly, I would like to thank God who has sustained me countless times. No matter what happens, I can trust that He has everything under control. He has never failed me.

TABLE OF CONTENTS

LIST OF ILLUSTRATIONS

LIST OF TABLES

NOMENCLATURE

Symbol	Description
da/dN	Fatigue Crack Growth Rate per Cycle
ΔK	Stress Intensity Factor Amplitude
ΔK_{th}	Threshold Stress Intensity Factor Amplitude
R	Stress Ratio
K_{max}	Maximum Stress Intensity Factor
K_{min}	Minimum Stress Intensity Factor
f	Fatigue Cycling Frequency
f_{crit}	Critical Cycling Frequency
W_a	Work of Adhesion
γ_α	Surface Tension of the Adhesive
γ_β	Surface Tension of the Adherend
$\gamma_{\alpha\beta}$	Interfacial Surface Tension of Adhesive and Adherend
η	Viscosity
K_I	Mode I Stress Intensity Factor
K_{II}	Mode II Stress Intensity Factor
K_{III}	Mode III Stress Intensity Factor
J	Energy Release Rate (J-Integral)
θ_p	Crack Propagation Direction
x	Half-Weld Width
y	Hook Intrusion Depth
θ_h	Hook Intrusion Angle
t	Sealant Layer Thickness
T_g	Glass Transition Temperature
E	Young's Elastic Modulus
v	Poisson's Ratio
θ_w	Equilibrium Wetting Angle

1. INTRODUCTION

1.1 PURPOSE STATEMENT

Friction Stir Welding (FSW) of aluminum alloys for aerospace applications offers unique advantages over riveting in weight reduction and structural continuity. A lack of understanding of corrosion and corrosion fatigue of friction stir welded aluminum joints prevents the process from being implemented. Studies have revealed a severe loss in fatigue life of friction stir welded aluminum joints when immersed in 3.5 % NaCl solution [1-3]. This is attributed to hydrogen environment embrittlement consistent with findings in the literature regarding corrosion fatigue of aluminum immersed in 3.5 % NaCl solution [4-9]. The purpose of this thesis is to investigate the use of a sealant to protect a friction stir welded lap joint from corrosive media and reduce the loss in fatigue life. Sealant candidates are considered in light of such factors as the sealant properties, effect of the sealant on weld properties, and feasibility of pre-weld application.

1.2. FRICTION STIR WELDING

Friction Stir Welding (FSW) has been a promising substitute for conventional welding, riveting, and other joining techniques since its inception in 1991 at the Welding Institute in Cambridge, England. In high-strength aerospace aluminum alloys, particularly the 2xxx and 7xxx series, conventional welding is not feasible due to their high risk of solidification cracking [10]. The main alloying elements that contribute to the solidification cracking tendency are Cu [11], Mg [12], and Li [13]. Riveting has remained the only feasible joining operation available for aerospace structures for these

alloys. Friction stir butt welds of these alloys offer a stronger joint than conventional welds with fatigue properties similar to those of riveted joints [14]. A significant weight reduction can be achieved with the removal of riveting hardware in addition to the reduction in damage associated with riveting hardware breaking loose within the aircraft structure. Even though FSW does not involve any melting, the heat generated by the process produces significant changes in the microstructure and produces residual stresses on the order of 10-100 MPa [15-16]. With these microstructural changes and residual stresses is associated a potentially deleterious effect on mechanical properties and corrosion resistance. Most research has been limited to butt welds joining plates of the same alloy.

In FSW, a rotating pin is inserted down into the materials to be joined and stirs the material with the aid of frictional heat (see Figure 1.1). The pin is then passed across the material forming a weld seam. FSW yields a thermomechanically affected zone surrounded by a heat affected zone (HAZ) as opposed to conventional welding that

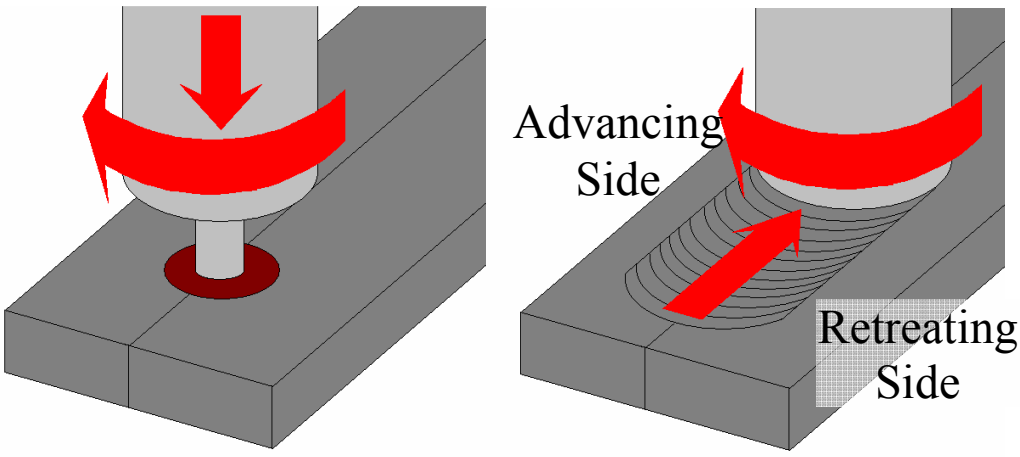

Figure 1.1. FSW process showing (a) plunge and (b) traverse of tool across seam.

produces a weld nugget and an HAZ (see Figure 1.2). The intense mechanical deformation combined with the high temperatures of FSW produces recrystallization within about 30 – 50 % of the thermomechanically affected zone [1, 14, 17-19]. The region that recrystallizes is referred to as the "weld nugget." The region above the weld nugget is the flow arm and is formed behind the tool shoulder as it passes over the weld.

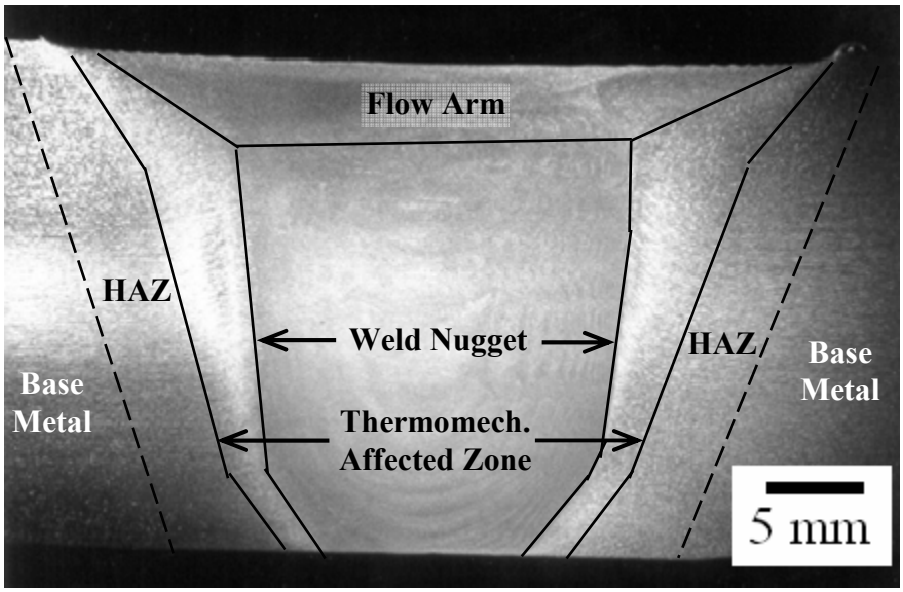

Figure 1.2. Friction stir welded butt joint of 7050-T7451 plates showing various regions of weld.

A relative quantification of heat input to the weld can be estimated by calculating pseudo heat index using the welding parameters [20]

$$HI = \frac{\omega^2}{v} \tag{1}$$

where ω is tool rotation speed in rotations per minute (rpm) and v is feed rate in mm/s (in/min). The mechanical properties of the various zones of the weld are dependent on the type of aluminum alloy (heat-treatable or non heat-treatable) and in some cases on the base metal heat treatment condition. High strength aerospace aluminum alloys are of the heat-treatable type and derive their improved tensile strength from strengthening particles that precipitate while aging after solution treatment. The spacing between particles is inversely related to the strength contribution [21]. Therefore, the strength contribution is increased for a given volume fraction of precipitates by decreasing particle size. This can be achieved by aging at lower temperatures, which increases precipitate nucleation rate and reduces precipitate growth rate. Increasing homogeneity of dispersion also improves the strength contribution. Cold work prior to aging increases dislocation density and therefore increases the homogeneity of dispersion if the particles nucleate on dislocations, as with 2xxx series Al-Cu-Mg alloys.

Dixet et al. compared the effects of welding at various heat indices between 9,800 and 39,400 $(\text{rpm})^2/(\text{mm/s})$ on the mechanical properties of butt welds from 2024-T3 and 2024-T8 [17]. Tempers T3 and T8 involve solution treatment followed by cold work, after which T3 is naturally aged and T8 is artificially aged. The strength of the weld nugget increases with increasing heat index and the weld nugget strength and microstructure are independent of the base heat treatment condition. The strength of the HAZ increases above that of 2024-T8 with increasing heat index for the naturally aged temper (T3) and decreases below that of 2024-T8 with increasing heat index for the artificially aged temper (T8). Therefore, for the T3 condition, the HAZ is the strongest region and the base metal is the weakest. For the T8 condition, the base metal is slightly

stronger than the weld nugget, and the HAZ is the weakest region. The effective heat treatment in the HAZ is similar to increasing the aging time or temperature. Therefore, an artificially peak-aged material will likely be overaged in the HAZ while a naturally aged material will likely have elevated properties in the HAZ.

Pao et al. [1] examined the effects of FSW on the microstructure of 2519-T87 (peak-aged condition) in different locations of each zone. Friction stir butt welds were made with a rotation speed of 275 rpm and a traverse rate of 1.69 mm/s (heat index = 44,800 $rpm^2/mm*s$). Microstructures of each weld zone are shown in Figure 1.3. In all regions of the material affected by FSW, the hardness is significantly lower than that of the peak-aged parent material with very fine θ' precipitates. Higher heat input is experienced at the top of the weld nugget than at the bottom resulting in a variance in microstructure and properties through the depth in the weld. This variance includes a gradient of recrystallized grain size, decreasing from 12 μm at the top to 2 μm at the bottom of the weld nugget. However, the effect of grain size on hardness is

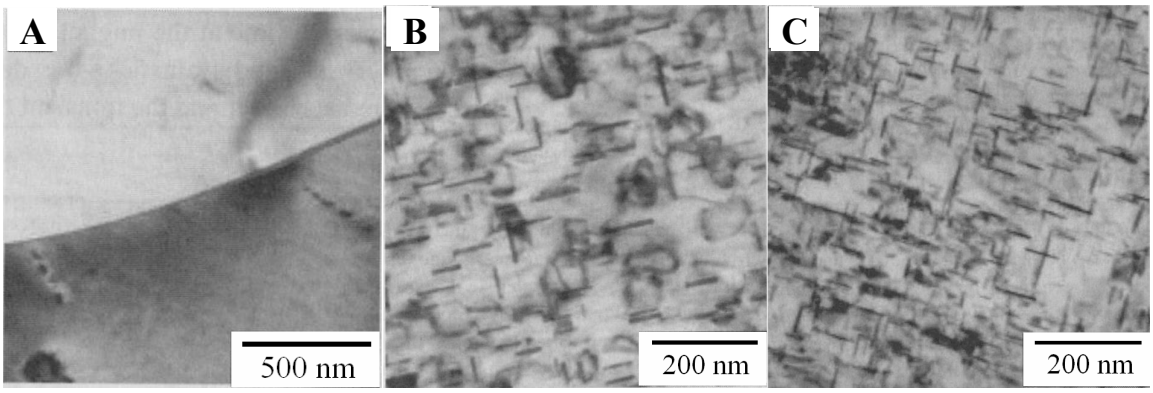

Figure 1.3. Microstructure in (a) weld nugget, (b) HAZ, and (c) base metal of friction stir welded butt joint of 2519 plates. Figure from Pao et al. [1].

overshadowed by the influence of strengthening precipitates. The precipitates in the top region of the weld nugget dissolve completely and re-precipitate resulting in higher hardness than the surrounding HAZ (see Figure 1.4). Complete dissolution is not achieved in the bottom of the weld nugget resulting in an overaged microstructure of coarse θ particles (~250 nm). The HAZ is composed of coarsened θ' particles and the degree of overaging depends on the distance from the weld. Similar microstructures have been reported for friction stir welded 7050-T7451 [2, 16]. Precipitate-free zones along sub-grain boundaries as well as strengthening precipitates increase in size in the HAZ [2].

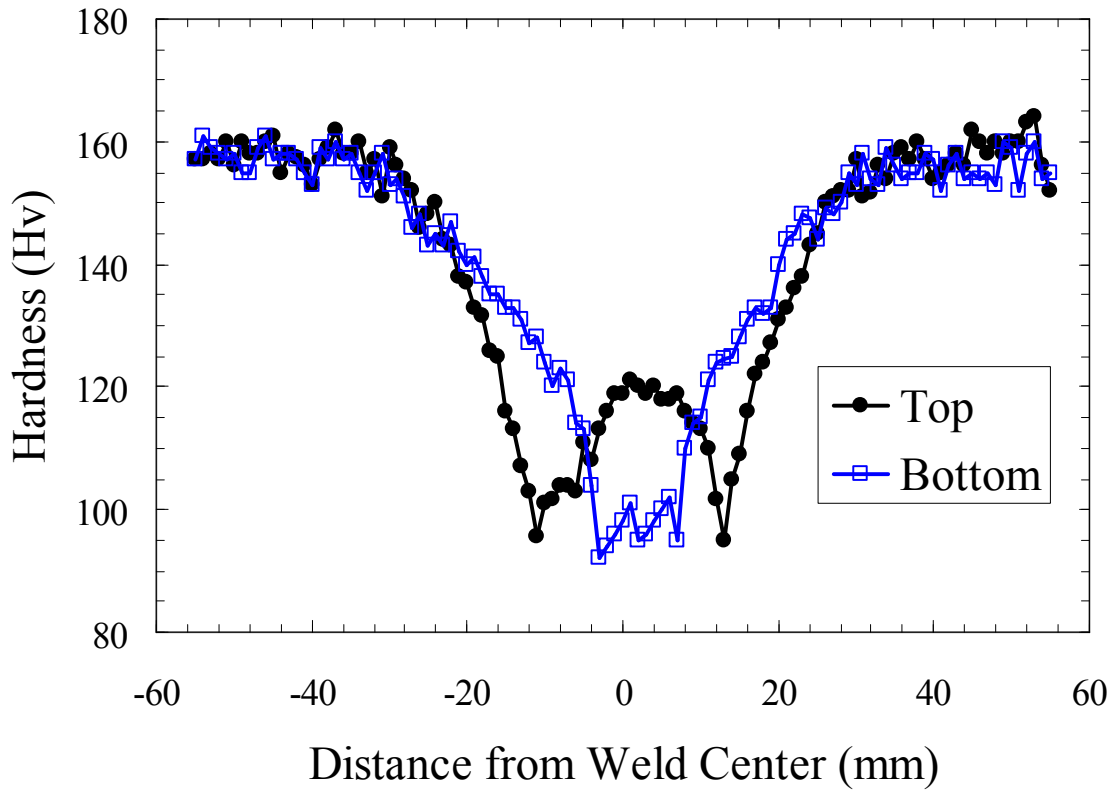

Figure 1.4. Hardness profile across the top region and bottom region of friction stir welded 2519 plates [1].

Compressive residual stresses 20 to 120 MPa were observed in the weld nugget and HAZ with corresponding tensile residual stresses less than 120 MPa in the adjacent parent metal [16]. Comparable residual stress distribution is reported for plasma arc welding of 2219 of similar thickness (7 mm) [22].

FSW offers a unique ability to join dissimilar metals. Successful combinations include the union of wrought aluminum alloys of different alloy series [15, 23], wrought aluminum to cast aluminum [3, 18], and copper to aluminum [23]. Stirring results in heterogeneous mixtures in which alternating layers of each material form what has been referred to as an "onion ring" pattern (see Figure 1.5). The weld nugget strength tends to be somewhere between those of the two base metals. Butt joining of 7050 to 2024

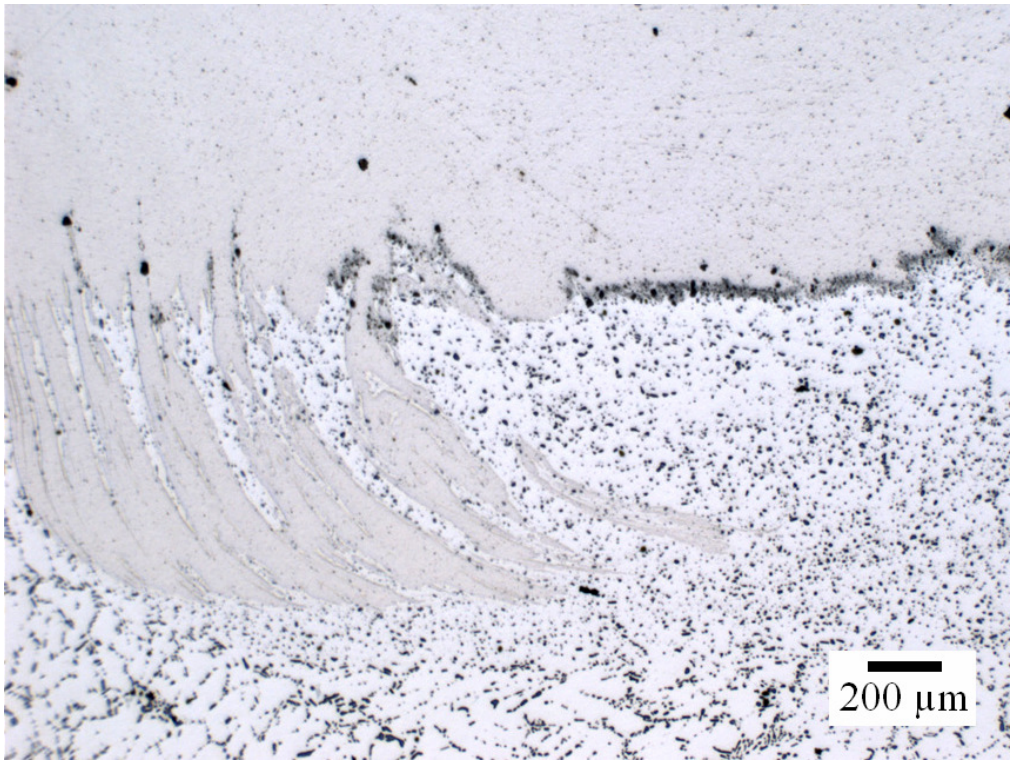

Figure 1.5. Weld nugget "onion ring" pattern in a friction stir welded lap joint of 2024 to 357 aluminum.

aluminum revealed low tensile residual stresses (~40 MPa) in the HAZ and low compressive residual stresses in the weld nugget (~30 MPa) and adjacent parent materials (~20 MPa) [15]. The reduced residual stresses compared with those of joining similar materials may be related to the use of different welding parameters. Butt joining results in the highest weld strength when the stronger material is welded on the retreating side of the weld (the side at which tool rotation is contrary to tool traverse direction as shown in Figure 1.1) [15].

1.3 MECHANICAL FATIGUE

1.3.1 Mechanical Fatigue of Aluminum. Fatigue crack growth of aluminum alloys can be modeled by Paris law

$$da/dN = C\,(\Delta K)^n \tag{2}$$

where da/dN is crack growth rate per cycle, ΔK is stress intensity factor amplitude, C and n are material parameters. This relationship only fits in stage II, or the Paris regime, of fatigue cracking (see Figure 1.6). Stage I is characterized as an increasing growth rate that occurs above a threshold stress intensity factor amplitude ΔK_{th}, and stage III is unstable crack growth preceding overload failure at the critical stress intensity factor K_c. Paris parameters for fatigue in air are generally independent of the microstructure and type of aluminum alloy but are influenced by stress ratio R and maximum stress intensity factor K_{max} (see Figure 1.7). These are interrelated by

$$\Delta K = K_{max} - K_{min} \tag{3}$$

$$R = K_{min}/K_{max} \tag{4}$$

An approach to using the Paris law was developed by Sadananda et al. that incorporates stress ratio by estimating *da/dN* versus a combined ΔK and K_{max} factor [24-25]. In their work, the need to quantify crack growth rates in terms of both K_{max} and ΔK was emphasized due to the competing role of each parameter at low and high R. At $R < 0.5$, fatigue is controlled by ΔK, and at $R > 0.5$, fatigue is controlled by K_{max}. These competing modes were observed in both ductile cast iron and nickel-based superalloys [25]. Stress ratio influences crack growth rates and ΔK_{th} presumably due to the effect of crack closure [26] and/or residual stress [24, 27]. Both of these effects are amplified at low R. Plasticity-induced crack closure is the effect of isolated crack-tip plasticity 'holding' the crack open at low K, effectively increasing the experienced K_{min} and decreasing ΔK. Another type of crack closure, roughness-induced crack closure, can occur when mode II stress intensity factor displacement prevents a torturous crack surface from realigning during unloading, also reducing effective ΔK. Meanwhile, hysteresis can produce compressive residual stress in the crack tip region during unloading, which reduces the effective ΔK upon reloading. Sadananda et al. argue that the compressive residual stress effect dominates crack growth retardation in ambient air fatigue rather than crack closure [24].

Stress ratio effects can be accounted for to some extent by using ΔK^+ in the Paris law equation (eq. 2) where $\Delta K^+ = K_{max}$ when $K_{min} < 0$ and $\Delta K^+ = \Delta K$ when $K_{min} > 0$. Kujawski describes an extension of the unified approach developed by Vasudevan et al. in which crack growth is driven by $\sqrt{\Delta K^+ * K_{\max}}$ [28]. By this method, crack closure data can be disregarded, and all crack growth data for an aluminum material fall roughly

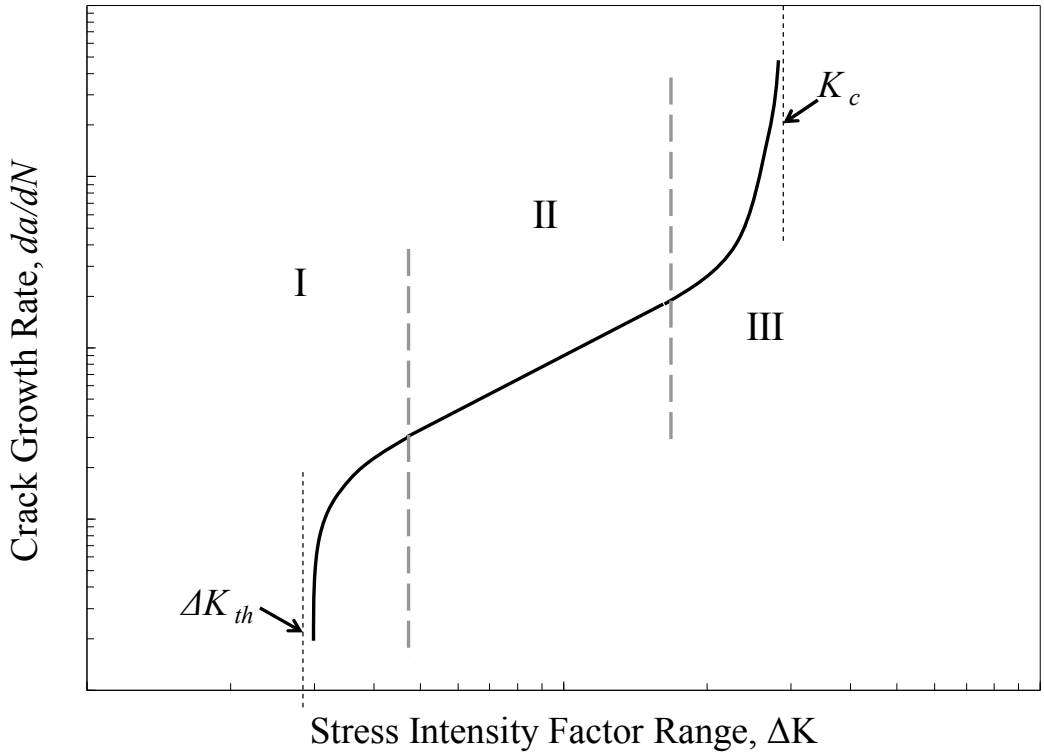

Figure 1.6. Schematic of typical fatigue crack growth obeying Paris law. Region II denotes where Paris law fits, $da/dN = C\,(\Delta K)^n$.

under the same curve, regardless of stress ratio. The data in Figure 1.7 is shown in terms of the unified parameter (see Figure 1.8). Kujawski showed this approach fits for 2324, 2024, 6013, 7055, and 7075 aluminum alloys. This approach was explored in depth for 2024-T351 by Maymon, and a linear relationship between ΔK_{th} and $K_{max,th}$ was observed [29].

The presence of two linear regimes in Figure 1.8 may be related to long and short crack growth. Traditional fracture mechanics predicts crack growth for long cracks in which the fatigue process zone exceeds the size of microstructural features such as precipitates and grain size [31-32]. In short cracks, the process zone is smaller, crack growth rates tend to be higher than those predicted by long crack data and crack growth is

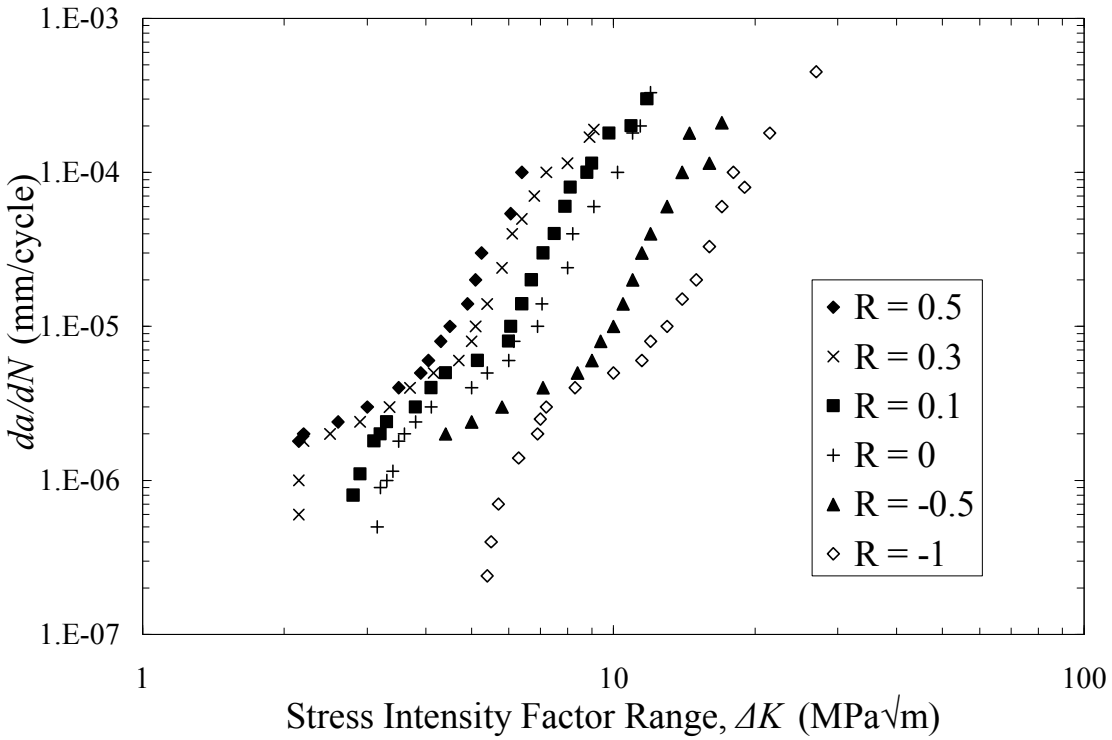

Figure 1.7. Fatigue crack growth data in ambient air of 2024-T351 at various stress ratios [30].

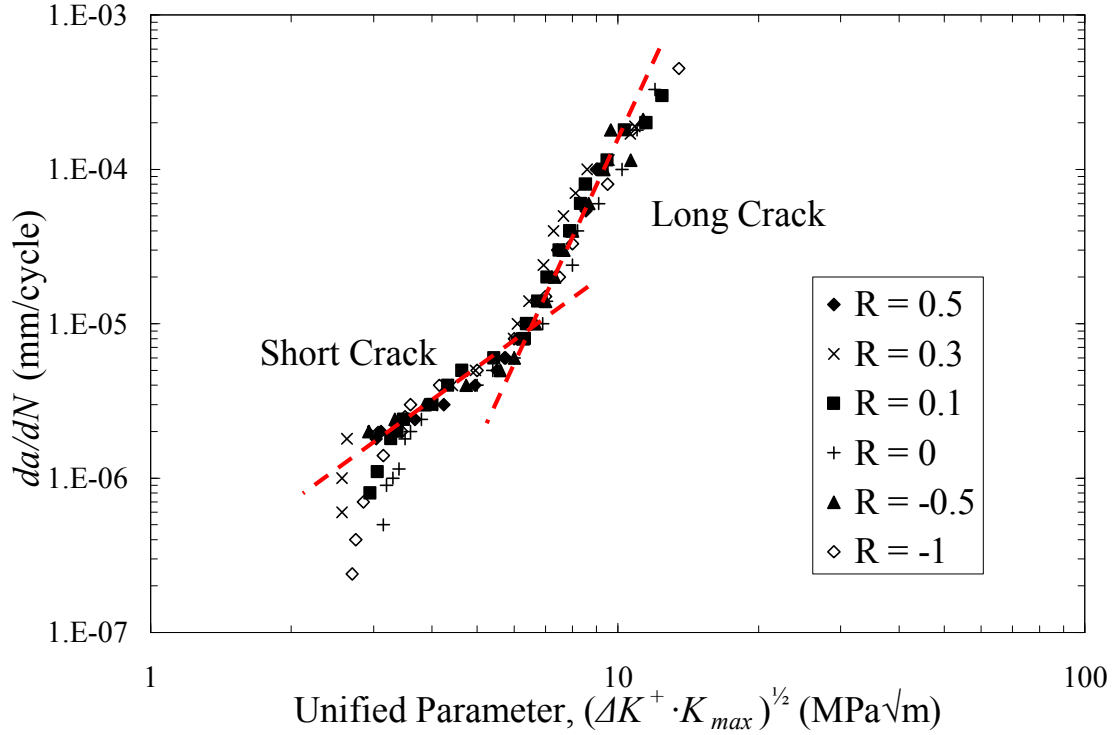

Figure 1.8. Fatigue crack growth data in ambient air of 2024-T351 at various stress ratios versus the unified parameter, $\sqrt{\Delta K^{+} * K_{max}}$ [30].

observed below ΔK_{th} for long crack growth. Therefore, the first linear regime may be related to short cracks and blends into the long crack regime as the crack grows.

1.3.2. Mechanical Fatigue of Friction Stir Welded Aluminum. Fatigue crack growth of friction stir welded 2024 butt joints is predominantly controlled by residual stress rather than microstructure and hardness changes due to FSW [16, 33]. The crack growth rate in the friction stir welded joints compared with the base metal is either higher or lower depending on the residual stress. Fatigue in the HAZ is comparable in crack path and fatigue life to the parent metal [34]. The crack path in the thermomechanically affected zone, especially in the weld nugget, tends to follow the "onion ring" flow pattern. Hardness variations between these bands suggest a mechanical explanation for this crack path in which the crack is directed along the softer bands and deflected by the harder bands. In friction stir welded butt joints, a low-plasticity burnishing technique has been shown to improve fatigue life in ambient conditions and in corrosive environments with 7050-T7451 [35] and with 2219-T8751 [36-37] by inducing a compressive residual stress. Low-plasticity burnishing is a treatment in which a freely rotating ball tool applies a load as it passes across the surface imparting a deep layer (one quarter to one third plate thickness) of consistent compressive residual stress (400-500 MPa at the surface) with minimal plastic deformation [35, 37-38]. Similar to shot-peening, this is a superficial treatment and not likely applicable to T-lap joints in which fatigue nucleation occurs at the faying surface notches.

Fatigue initiation is controlled by defects in the weld in friction stir welded lap joints of 2024 to 357 [3]. The notches formed where the faying surface gaps meet the weld act as fatigue pre-cracks (see Figure 1.9). On the advancing side of the weld, the

notch tends to form a hook defect in which the notch is upturned into the top-skin. The oxide surface layer produces a debris field or oxide seam defect across the weld nugget emanating from the retreating side faying surface notch. The extent of these defects is controlled by the oxide layer thickness. Therefore, prior anodization of welded parts exacerbates these defects and reduces the joint strength. However, fatigue life is not significantly affected by prior anodization.

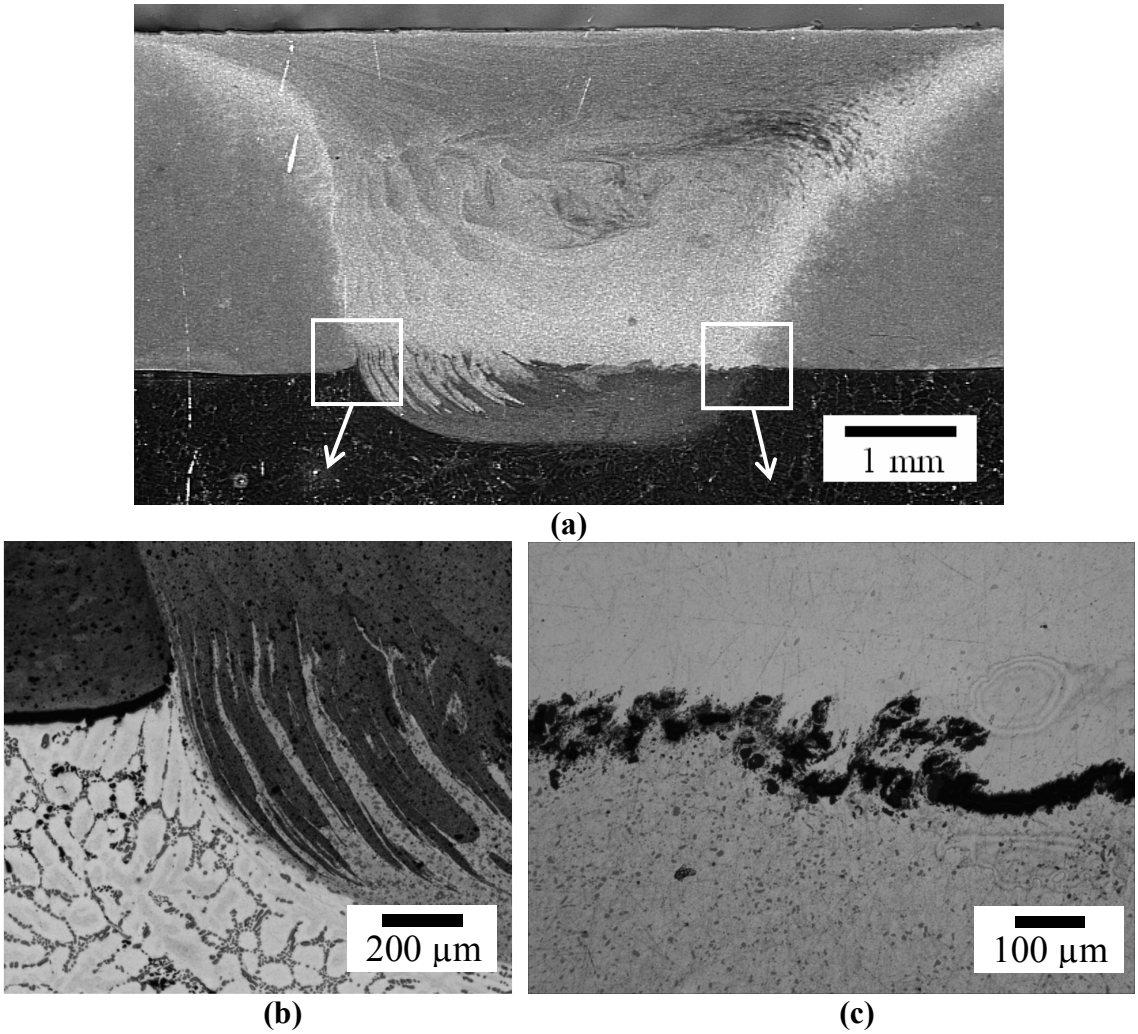

Figure 1.9. (a) Friction stir welded lap joint cross-section with anodized parts prior to welding. Exploded views of (a) show (b) hook defect at the advancing side faying surface notch and (c) oxide seam defect at the retreating side faying surface notch. Figure from Van Aken et al. [3].

1.4. CORROSION AND CORROSION FATIGUE

1.4.1. Corrosion Fatigue of Aluminum. The presence of a corrosive medium drastically increases the crack propagation rate in fatigue of aerospace aluminum alloys, particularly in aqueous chloride solutions. The exact mechanism of environmentally assisted fatigue crack propagation is unclear, but the effect of a corrosive medium is thought to be related to hydrogen-environment embrittlement in the crack-tip region. It has been suggested in the literature that stress-corrosion cracking mechanisms are similar to those in environmentally assisted fatigue cracking [39-41]. A similarity in intergranular crack morphology is in strong support of this hypothesis [5, 8]. At the current level of understanding, it is difficult to discern between static hydrogen-induced cracking (with hydrogen embrittlement mechanism) and classical stress corrosion cracking (involving the direct effect of material loss due to localized corrosion) and similar mechanisms may be at work in each case. For the purpose of this thesis, stress corrosion cracking and static hydrogen-induced cracking in aluminum alloys will be regarded collectively as static environmentally assisted cracking with the assumption that similar mechanisms operate in corrosion fatigue (particularly the hydrogen embrittlement mechanism).

Models have been developed based on an additive effect of environmentally assisted cracking on mechanical fatigue [39-41]. In early stage environmentally assisted fatigue cracking, ΔK is low and environmental effects are amplified resulting in intergranular or flat transgranular crack morphologies (for both short and long cracks) [8]. Although these crack morphologies are indistinguishable with those of static environmentally assisted cracking, Holroyd and Hardie compare such a model with crack

growth data and find it to be invalid. Instead, a synergistic effect of combined environmentally assisted cracking and mechanical fatigue is suggested, since crack propagation rates can be significantly higher than the sum of crack growth velocities in mechanical fatigue and static environmentally assisted cracking under similar conditions. The increased crack growth velocity in corrosion fatigue compared with static environmentally assisted cracking may be related to the higher strain rates at the crack tip in fatigue loading.

The mechanism of hydrogen embrittlement in cyclically loaded aluminum alloys is controversial. One explanation suggests that increased dislocation movement from excess hydrogen concentration results in localized plasticity and ductile fracture at lower stresses [42]. Another explanation suggests that the presence of hydrogen reduces cohesive strength and promotes decohesion [43-45]. A third theory suggests embrittlement is due to hydride formation at grain boundaries [46-47]. All three theories agree that hydrogen concentration at the crack tip is a controlling factor.

Hydrogen embrittlement theories are supported by findings relating corrosion fatigue cracking rates to hydrogen diffusion [6-8, 48-49]. Holroyd and Hardie found that accelerated corrosion fatigue rates in seawater are controlled by hydrogen diffusion along grain boundary paths in 7xxx series alloys [8]. The rate of flat transgranular corrosion fatigue propagation predicts about 10^{-13} m^2/s hydrogen diffusion rate at room temperature, consistent with grain boundary diffusion in 7xxx series alloys [50-51]. This finding suggests that the primary classical corrosion fatigue mechanism, that is the anodic dissolution promoted by mechanical destruction of the passive layer at the crack tip, promotes crack propagation indirectly in aluminum in corrosive environments.

Corrosion at the crack tip promotes the cathodic production of hydrogen which increases the hydrogen concentration in the crack tip.

As crack growth occurs, bare aluminum metal is exposed to and reacts with H_2O whether in water vapor or in solution, the products of which form hydrogen ions that diffuse into the crack tip [52]. This reaction has shown dependence on pH and Cl^- concentration; it is promoted by the presence of NaCl solute and a reduction in pH [53]. Hydrogen diffusion is driven by hydrogen concentration and hydrostatic tensile stress at the crack tip [48, 54] and is expected to be accelerated due to the high dislocation density in the deformed metal at the crack tip. In Ni, increased dislocation density due to deformation increases the apparent diffusivity of hydrogen from 10^{-14} to 10^{-9} m^2/s [55-56].

In addition to aqueous solutions, environmentally assisted fatigue cracking is observed in ambient air fatigue due to the presence of water vapor. Wei reported that the crack propagation rates in both 2xxx and 7xxx series alloys in gaseous environments at a given ΔK are proportional to the product of partial pressure of water vapor and the inverse of crack opening frequency [49]. In a vacuum, short and long crack growth rates are dependent of microstructure, particularly grain size and whether or not the strengthening precipitates are shearable [57-58]. This microstructural dependency may be related to the difference in crack path roughness and roughness-induced closure due to enabling of planar slip and slip reversibility (reduced persistent slip bands). In contrast, long fatigue crack growth rates in humid air in the Paris regime are generally microstructure independent [28, 57]. It is thought that the embrittlement due to the presence of hydrogen in moist air negates the beneficial effects of microstructural

features such as slip reversibility due to shearable strengthening precipitates. The crack morphology in a vacuum has been characterized as ductile, striated transgranular at all *da/dN*, whereas that of fatigue in moist air is dependent on *da/dN* [58]. At near threshold *da/dN* in moist air, fatigue is brittle transgranular; at higher *da/dN*, fatigue is ductile transgranular.

Holroyd and Hardie evaluated the effect of cycling frequency *f* between 0.1 and 70 Hz for 7017 in natural seawater [8]. It was found that a combination of long crack tip exposure time per cycle (low *f*) and low ΔK (early stage crack growth) for a constant *R* results in intergranular crack morphology, similar to that in static environmentally assisted cracking of the same alloy. As crack growth continues and ΔK increases, the crack propagation progresses to a brittle transgranular mode. The ΔK at which this transition takes place decreases with increasing frequency and corresponds with the transition from stage I crack growth to Paris regime crack growth. Further increase in frequency resulted in another transition of crack morphology to one characterized as ductile, striated transgranular, similar to that in dry air [8]. The ΔK at which this transition takes place also decreases with increasing frequency. This implies that at high frequencies the crack propagation is likely dominated by mechanical fatigue mechanisms, whereas at low frequencies, environmentally assisted cracking modes dominate. Similar progression in environmentally assisted fatigue crack morphology during crack growth has been observed in 2024 [5].

Gasem and Gangloff [6-7] explored the dependence of cycling frequency on environmentally assisted fatigue crack propagation rates for various environments and alloys. For a given environmental hydrogen concentration in moist air and aqueous

solutions, a critical frequency f_{crit} exists at which crack growth rate per cycle *da/dN* is maximized because of hydrogen saturation at the crack tip. *da/dN* decreases with increasing frequency at frequencies higher than f_{crit} and hydrogen diffusion becomes a controlling factor. A plateau in *da/dN* exists for a range of frequencies below f_{crit} but at very low frequency, *da/dN* decreases presumably due to crack closure with increasing corrosion product in the crack wake (see Figure 1.10) [6-7, 48]. It should be noted that the decline in *da/dN* at low frequency is not observed for moist air fatigue presumably because insufficient oxide is produced to induce crack closure [59]. Studies on 7xxx have shown the crack growth rate at various ΔK at frequencies above f_{crit} is proportional

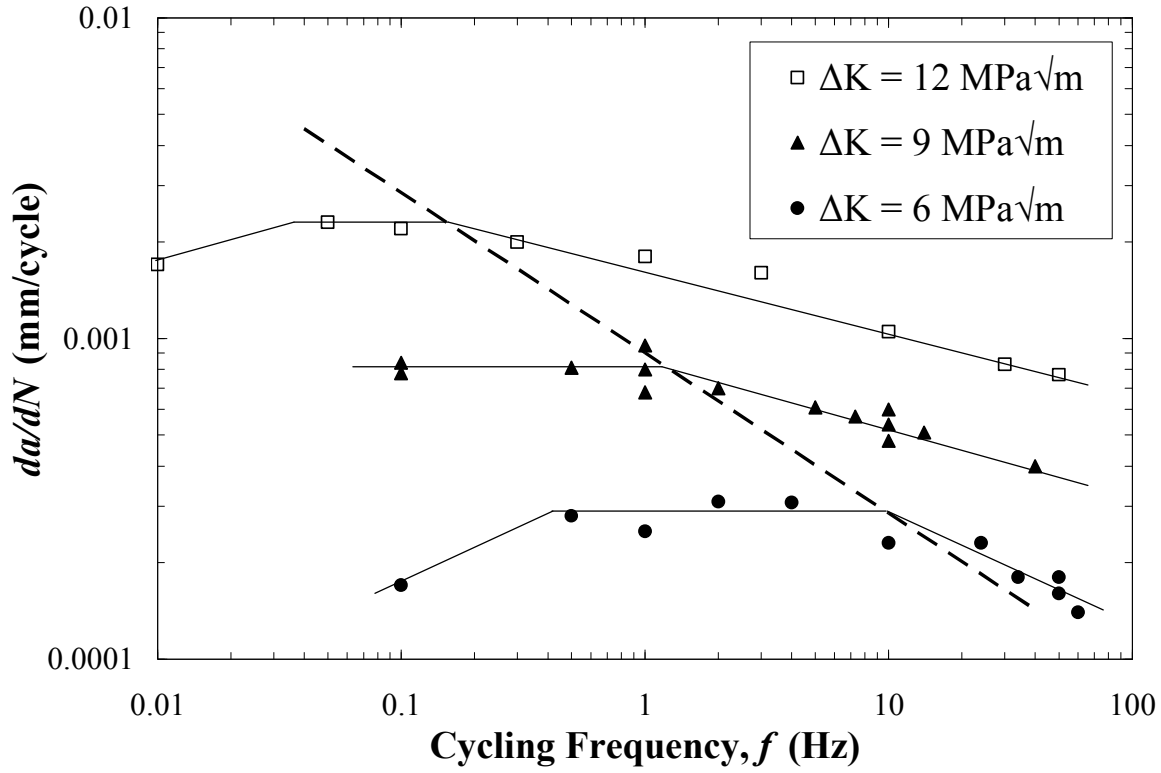

Figure 1.10. Crack growth rate versus cycling frequency at various ΔK for 7075-T651 in 3.5 % NaCl solution at R = 0.1 [6]. Dotted line denotes critical frequency trend: $da/dN \propto 1/\sqrt{f_{crit}}$. The plateaus at f below f_{crit} represent regions of crack tip hydrogen saturation.

to $1/\sqrt{f}$, consistent with hydrogen diffusion controlled, environmentally assisted fatigue cracking [6-8]. However, a similar study of environmentally assisted fatigue cracking in 2090 showed no such frequency dependence [9]. This study was limited to frequencies between 0.1 and 20 Hz and ΔK of only 2 MPa$\sqrt{m}$. At low ΔK in 7075 alloys, f_{crit} is expected to increase far above 20 Hz. Gangloff suggests these findings illustrate the plateau region of frequency and support a similar frequency dependence of environmentally assisted fatigue in 2xxx series alloys [4].

Age hardening effects on environmentally assisted fatigue crack propagation rates are unclear and research is incomplete. Lin and Starke reported that overaging or increasing Cu content in Al-6Zn-2Mg-xCu (similar to 7075) reduces hydrogen embrittlement effects on fatigue crack growth rates in distilled water versus dry air [60]. Lin and Starke attribute this to the formation of noncoherent precipitates during overaging that produce a more homogeneous slip and reduce hydrogen transport via dislocations through the crack tip region [39]. However, Gasem and Gangloff reported a higher critical frequency for overaged versus peak-aged in 7075, or in other words, less time per cycle required to saturate the crack tip with hydrogen, implying a higher diffusivity in the overaged condition [6]. Therefore, the role of planar slip in the peak-aged condition (promoted by coherent and shearable precipitates) in destroying the crack tip passive layer and promoting corrosion activity should be considered. It was previously noted that overaging increases crack growth rates in a vacuum by reducing slip reversibility, crack path roughness, and thus crack closure [57, 61]. Aging studies on 2024-T351 show no dependence of environmentally assisted fatigue crack propagation rates for fatigue in moist air [61], consistent with common observations regarding

microstructural effects on ambient air fatigue crack growth rate and crack roughness of long cracks [57]. Before hydrogen embrittlement effects can be successfully mitigated by metallurgical means, a more thorough investigation is necessary to separate the environmentally assisted fatigue cracking modes involved with different environments.

1.4.2. Corrosion of Friction Stir Welded Aluminum. FSW in aluminum alloys alters the microstructure [1-2, 16-17] and incorporates residual stresses [15-16, 33]. Both of these results are detrimental to corrosion resistance and cause increased corrosion in the metal affected by the weld. In the case of 2024, Davenport et al. [62] reported a dependence of anodic activity on welding parameters where increased localized intergranular corrosion in the weld nugget is associated with slow tool rotation speed (lower heat index) and in the HAZ with fast tool rotation speed (higher heat index). Cathodic activity in the weld nugget increases with higher speeds due to fragmentation and re-precipitation of intermetallic particles, thus, protecting the weld nugget from corrosion, and resulting in increased corrosion in the HAZ instead. A study on FSW of dissimilar 2024 to 7010 reported increased cathodic activity in the 2024 portion of the weld nugget and corresponding intergranular corrosion in the 7010 portion of the weld nugget [63].

Van Aken et al. investigated the effects of anodizing prior to FSW of 2024 to 357 [3]. Lap joints were immersed in a lap joint simulant solution developed by Kelly and Ferrer [64]. It was found that the anodized lap joints exhibited improved corrosion protection. Although corrosion of both anodized and bare welds reduced fatigue life of the lap joints, the extent was less severe for the anodized welds.

1.4.3. Corrosion Fatigue of Friction Stir Welded Aluminum. A study on friction stir welded 7050-T451 investigated the effects of pre-corrosion on mechanical fatigue properties [19]. The fatigue endurance limit was reduced by 50 % after exposure for 100, 500, or 1000 hours in wet/dry salt fog cycling described in Annex 5 of ASTM G 85 [65]. For samples exposed 0 or 100 hours, fatigue initiation occurred at the interface between the thermomechanically affected zone and weld nugget. For samples exposed 500 or 1000 hours, fatigue initiated at pits in the HAZ. Electrochemistry studies showed the HAZ and thermomechanically affected zone act as anodes to the base metal and weld nugget. This is supported by the observation of deeper pits in the HAZ and thermomechanically affected zone of corroded specimens.

Pao et al. [1] compared the fatigue crack growth of friction stir welded 2519-T87 butt joints through the base metal, weld nugget, and HAZ. Specimens were fatigued in ambient air and 3.5 % NaCl solution. In both the NaCl solution and air, fatigue crack growth rates were highest in the base metal, followed by the HAZ, and lowest in the weld nugget. An opposite trend was observed for ΔK_{th}, that is, lowest for the base metal and highest for the weld nugget. An investigation on friction stir welded 7050-T7451 aged after welding reported that crack growth rates in the weld nugget were nearly as high as those in the base metal and were lowest in the HAZ [2]. It is suggested that the reduced crack growth rates in the weld region for both 7050 [2] and 2519 [1] alloys is related to the presence of compressive residual stresses, since the strength and hardness of weld regions are actually lower than those of the base metal. Fatigue crack growth rates for each region in the 3.5 % NaCl solution are roughly twice those in ambient air in the intermediate and high ΔK regimes for both alloy systems. However, at low ΔK,

corrosion-product induced closure reduces crack growth rates in 3.5 % NaCl solution. As a result, the effective ΔK_{th} in the 3.5 % NaCl solution is higher than that in air and at ΔK below about 5 MPa$\sqrt{m}$ for both 2519 and 7050, crack growth rates in 3.5 % NaCl solution are actually lower than those in air.

Stress-life fatigue testing in air of friction stir welded 2519 revealed that the fatigue life and fatigue threshold are lower than those of the base metal alone [1]. Fatigue specimens were machined in the transverse direction and contain in the gage section the weld and surrounding parent metal. Fatigue occurs through the softest region in this configuration, the HAZ. The fatigue life in 3.5 % NaCl solution of the base metal and that of weld are comparable and much lower than those observed for fatigue in air.

Fatigue crack surfaces through the base metal and HAZ in both air and 3.5 % NaCl solution were reportedly transgranular in nature in friction stir welded 7010 [2]. In the weld nugget, crack surfaces were transgranular for fatigue in air and intergranular for fatigue in 3.5 % NaCl solution. The difference in crack path in the weld nugget may be related to the depletion of Cu and Zn at subgrain boundaries, as was observed in friction stir welded 7075, which could sensitize the grain boundaries and promote intergranular environmentally assisted cracking [66]. This transition from transgranular to intergranular crack path was also observed as frequency is decreased below f_{crit} in parent metal [8, 48] indicative of a transition from predominantly mechanical fatigue to environmentally assisted fatigue.

Fatigue in 3.5 % NaCl solution of friction stir welded lap joints revealed severely reduced fatigue lives regardless of whether the parts were anodized prior to welding [3].

It is thought that the bare aluminum surface of the weld scroll acts as a path for hydrogen transport to the weld nugget and fatigue crack tip.

1.5. SEALANTS FOR FRICTION STIR WELDED LAP JOINTS

One method of mitigating corrosion is to protect the lap joint gaps via a sealant (see Figure 1.11). The size of the gap (< 1 mm) does not lend itself well to a post-weld, sealant application. Therefore, a sealant must be applied prior to welding. The sealant must be welded through without being retained in the weld or affecting the weld properties. Sealants for conventionally welded lap joints have been investigated and developed, particularly for steels [67-69]. FSW involves heat evolution which can be used similarly for conventional welding to cure or melt a sealant. Because the process is fairly rapid and heat dissipation rates are quick, a curing step after welding may be necessary to allow enough time at elevated temperatures. This additional heat treatment is not desirable for large aerospace structural components. Therefore, a room temperature curing material or a material that hardens by solidification is preferred.

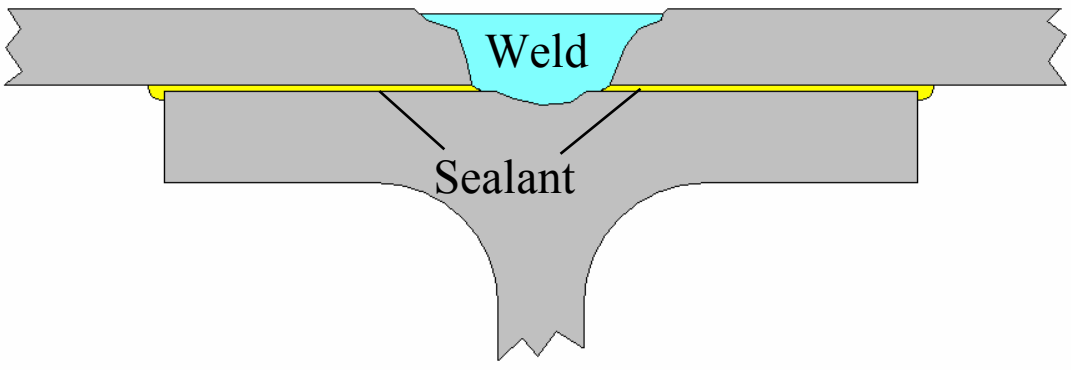

Figure 1.11. Cross-section schematic of friction stir welded lap joint with sealant for corrosion protection.

Investigation of sealants for friction stir welded lap joints has been limited to low temperature melting Al-Ge alloy [70], curable elastomers [71], and nylons [72]. A friction stir welded lap joint sealant for aerospace applications requires chemical stability, mechanical strength, and a low process temperature (melting or curing temperature). These properties can be met with a polymer or a metal, but for the purposes of this thesis, only polymeric candidates will be addressed.

Chemical stability can be broken down into oxidation and corrosion resistance, electrochemical inertness with joint metal, and low water absorption. Mechanical strength of interest comprises primarily adhesive and cohesive strength. Cohesive strength is related to bulk tensile properties of the material. Adhesive strength of a polymer on a metal is limited by cohesive strength of the polymer [73]. Adhesive strength is also proportional in an ideal sense to the work of adhesion W_a between the polymer and metal by

$$W_a = \gamma_\alpha + \gamma_\beta - \gamma_{\alpha\beta} \tag{5}$$

where γ_α is the surface tension of the adhesive (polymer), γ_β is the surface tension of the adherend (metal), and $\gamma_{\alpha\beta}$ is the interfacial tension between the components. The surface and interfacial tensions also influence interfacial void size as they determine wettability. A polymer with high strength and good wettability with the joint metal is ideal for adhesive strength. These properties need to be weighed with chemical stability and low process temperature. For aerospace applications, a polymer should have a melting point above the range of expected exposure and retain its properties throughout the range.

Nylon polymers fit the requirements of chemical and mechanical stability and the structure can be varied to achieve an appropriate melting temperature. The chemical

structure of a Nylon–6 is shown in Figure 1.12. Nylon–*n* is composed of (*n* – 1) consecutive ethylene groups separated by an amide group.

Nylon can also have an alternating structure in which each amide group is oriented oppositely as in Nylon–6/6 (see Figure 1.13) and can have alternating quantities of ethylene groups between amide groups as in Nylon–4/6 (see Figure 1.14).

With increasing nylon number, the density of amide groups in each polymer chain decreases and the structure of the polymer approaches that of polyethylene. It follows that the physical properties also approach those of polyethylene, particularly the melting point [74]. Bonding between chains in nylon is dominated by hydrogen bonding between amide groups of adjacent chains [75]. This bonding gives nylon high crystallinity and high stiffness. As the amide group density decreases (increasing nylon number) the crystalline interactions are reduced and the melting temperature and glass transition temperature decrease [74, 76].

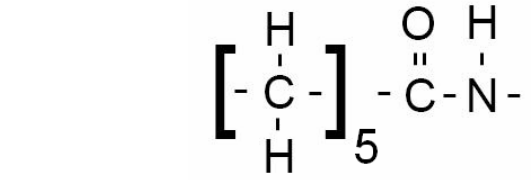

(a)

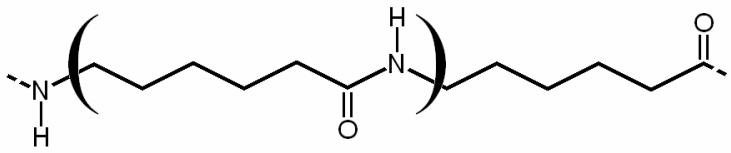

(b)

Figure 1.12. (a) Structure of Nylon–6 monomer bearing six consecutive C atoms per monomer: five in the ethylene groups and one in the amide group. (b) Alternative representation of Nylon–6 monomer in a chain (denoted by parentheses).

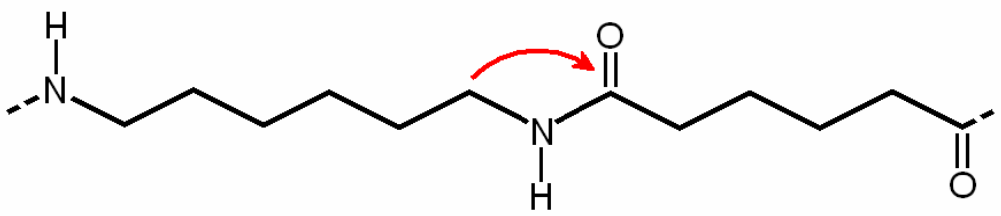

Figure 1.13. Structure of Nylon–6/6 monomer, similar to Nylon–6 except for position of oxygen double-bond which yields an alternating orientation of amide groups.

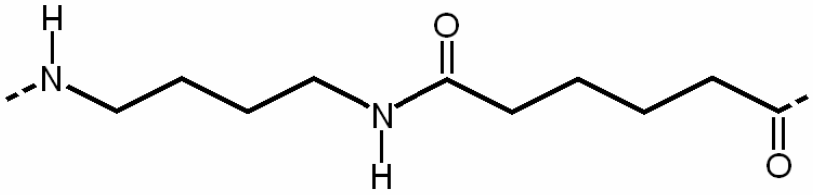

Figure 1.14. Structure of Nylon–4/6 monomer. Note only four C atoms between N atoms.

Because water is a highly polar liquid, water absorption in nylons varies proportionately with polarity of the nylon [75]. As the nylon number decreases and the polar amide group density increases, the polarity of the nylon increases and greater water absorption is expected. Water absorption reduces the elastic modulus, strength, and elongation of nylons [77-80]. For the sake of avoiding water absorption, the amide group density should be minimized by using a high nylon number.

In addition to amide group density, there is also an effect of even versus odd nylon number on bond density as shown by Slichter [81]. In a nylon crystal, chains can either be aligned parallel or anti-parallel. The arrangement occurs during solidification and is not purely random. There is a tendency for a nylon crystal to associate one way or the other. In odd nylons, a parallel structure is favored. However, because of the

arrangement of amide groups, the bond density is the same whether in a parallel or anti-parallel structure (see Figure 1.15). The reason for the preference may be related to the parallel structure providing a stronger association due to collinearity of the dipoles. In even nylons, the parallel structure has half the bond density of the anti-parallel structure, and so the anti-parallel structure is favored (see Figure 1.16). The anti-parallel structure lacks the dipole collinearity of the parallel structure and so even number nylons presumably have weaker crystalline association than odd number nylons with similar amide group density (i.e. less efficient crystalline bonding). Since the hydrogen bonds between amide groups of adjacent chains are responsible for the high strength and toughness of nylons, the density of these bonds will likely influence the mechanical properties. Therefore, an odd number nylon is expected to possess a superior ratio of strength to amide group density than an even number nylon.

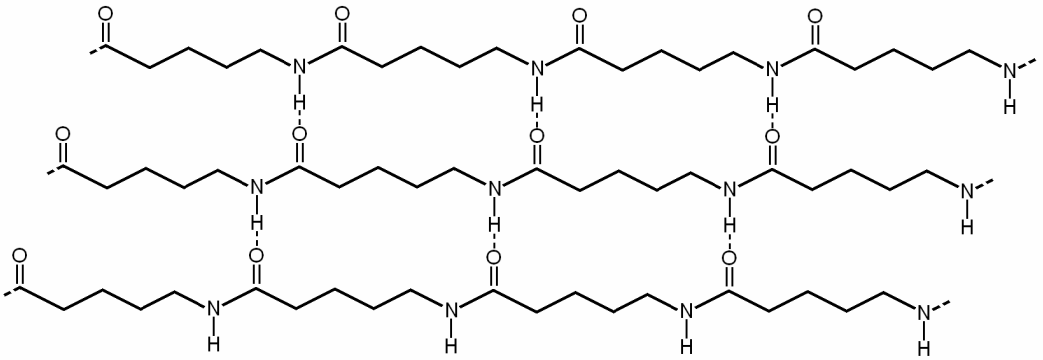

(a)

Figure 1.15. (a) Parallel and (b) anti-parallel crystal alignment in an odd nylon (Nylon–5). Parallel alignment is favored in odd nylons [81].

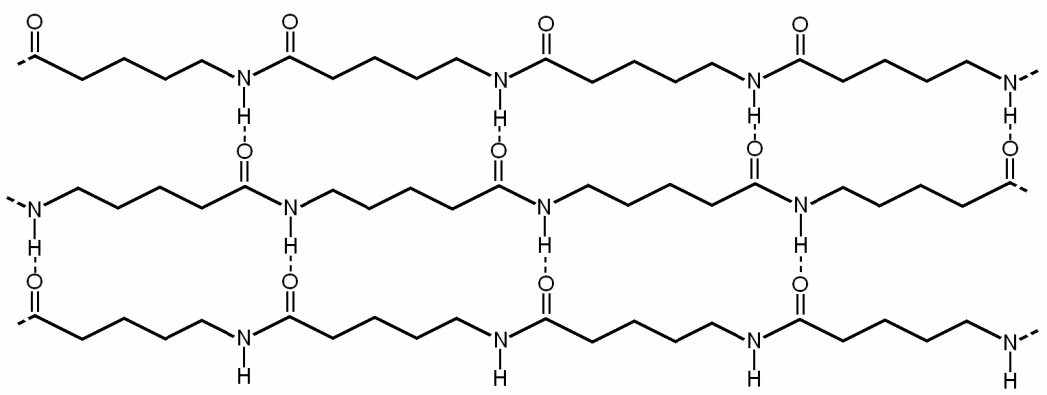

(b)

Figure 1.15. (cont.) (a) Parallel and (b) anti-parallel crystal alignment in an odd nylon (Nylon–5). Parallel alignment is favored in odd nylons [81].

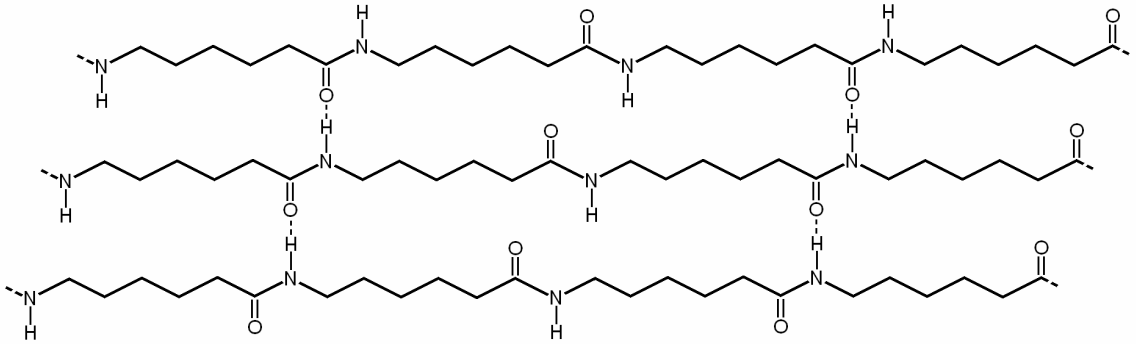

(a)

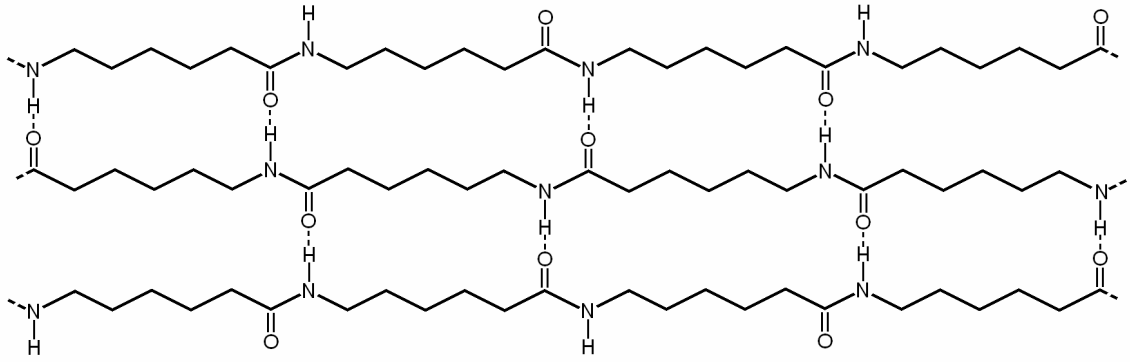

(b)

Figure 1.16. (a) Parallel and (b) anti-parallel crystal alignment in an even nylon (Nylon–6). Anti-parallel alignment is favored in even nylons [81].

The more efficient hydrogen bonding associated with odd number nylons versus even number nylons has implications with respect to melting temperature. Each series, even and odd, follows a trend of increasing melting temperature with decreasing nylon number but the odd number nylons have a higher melting point for a given amide group density, as observed by Holmes et al. [74] (see Figure 1.17). Nylon glass transition temperatures also tend to increase with decreasing nylon number [76], but a distinction between glass transition temperature and nylon number trends for even and odd nylons does not exist. This implies a higher dependency of glass transition and enabling of viscoelastic movement on chemical structure rather than crystalline structure.

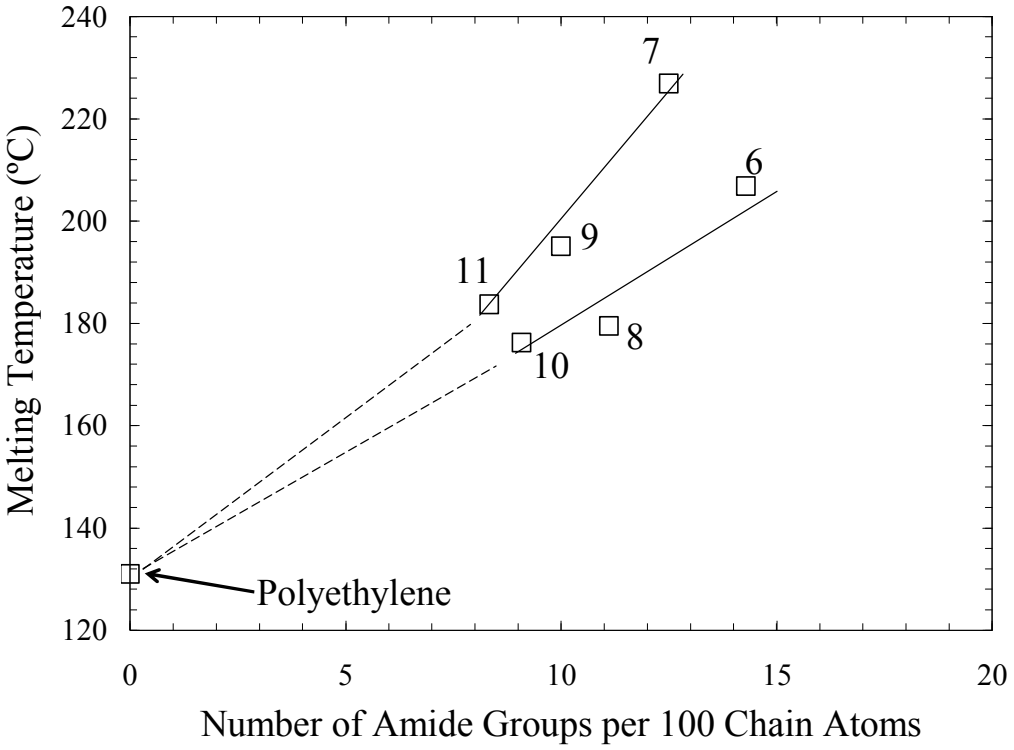

Figure 1.17. Melting point of various nylons, designated by nylon number [74]. Melting point decreases with increasing nylon number (decreasing amide group density) approaching that of polyethylene. Odd number nylons follow a steeper trend than even number nylons.

An odd number nylon will have a lower amide group density and more efficient bonding than an even number nylon with a similar melting point. Therefore, water absorption should be lower in an odd number nylon than an even number nylon of similar strength. By this justification, an odd number nylon is preferred as a sealant. Further selection of nylon should be based on melting temperature to fit FSW processes and still retain its properties throughout exposure ranges. On this basis, Nylon–11 (melting point ~195 ºC) was selected and pursued as a lap joint sealant candidate.

Addition of strong, solid fillers to polymers tends to increase the stiffness and tensile strength while decreasing the elongation to failure [82-89]. The ability to increase the stiffness and strength requires strong adhesion of the filler particles to the polymer matrix [86, 88, 90-92] and can be improved by pre-treating the filler material, such as with a silane treatment, to improve wettability of the polymer to the filler [85-86, 92]. Fillers investigated for nylons include mica [83], calcium carbonate [84], glass beads [85, 89], and silicates [86]. Reported properties are listed in Table 1.1 and filler effects on polypropylene and polyvinyl chloride are included for comparison.

Friction stir lap joining is a fairly rapid process with tool speeds typically on the order of 1 – 6 mm/s. As the tool passes, the structures being joined act as heat sinks and heat dissipation occurs rapidly. The polymer sealant is melted by the heat generated but only has a brief time window in which to thoroughly wet the rough surfaces of the adjoining metal structure before re-solidification.

Table 1.1. Summary of Mechanical Properties of Filled Polymers

Polymer	Additive	Size	Shape	Volume Fraction	Tensile Strength (MPa)	Elastic Modulus (GPa)	Elong. (%)	Ref.
Nylon - 6	None	-	-	-	26.5	0.92	-	85
	Glass	45 μm	Beads	0.05	25	0.98	-	85
				0.25	28	1.9	-	85
				0.40	21	2.8	-	85
Nylon - 6	None	-	-	-	71.7	1.07	120.6	84
	Calcium Carbonate	0.7 μm	Particles	0.05	66.3	1.22	61.3	84
				0.10	61	1.36	42.4	84
				0.15	54.4	1.55	32.7	84
				0.20	48.1	1.62	47	84
				0.25	44.5	1.95	30.2	84
				0.28	38.9	1.68	48.4	84
		3.5 μm		0.10	57.9	1.47	49.2	84
				0.20	50.8	1.82	38	84
				0.28	40	1.75	43	84
				0.40	28.6	2.85	11.8	84
Nylon - 6	None	-	-	-	-	1.37	-	83
	Mica	0.9-180 μm	Particle	0.05	-	1.5	-	83
				0.10	-	2	-	83
				0.20	-	4.2	-	83
Nylon - 6/6	None	-	-	-	79.3	-	-	89
	Glass	-	Beads	0.40	97.9	-	-	89
Poly-propylene	None	-	-	-	26	1.24	-	82
	Graphite	200 nm (diam.)	Fibers	0.15	30	2.72	-	82
Poly-propylene	None	-	-	-	32	1.57	-	85
	Glass	45 μm	Beads	0.05	30	1.8	-	85
				0.10	28	2	-	85
				0.20	22	2.4	-	85
				0.40	17	3.1	-	85
				0.50	10	3.8	-	85
PVC	None	-	-	-	19.5	0.0103	365	87
	Calcium Carbonate	-	-	0.20	19.5	0.0115	375	87
				0.33	17.1	0.0111	320	87
				0.66	8.6	0.0067	225	87

In wetting of an uncured or molten polymer onto a smooth surface, wetting becomes a dynamic process related to the polymer viscosity. For liquids with high viscosity, the dynamic wetting angle θ_d is increased per

$$\tan\theta_d = m\left(\frac{\eta v_f}{\gamma}\right)^n \tag{6}$$

where η is viscosity, γ is the liquid surface tension, v_f is the velocity of the advancing liquid film, and m and n are constants [93]. Wetting of a liquid on a rough surface is benefited by capillary action in crevices and pores [94] (additionally, adhesion to a rough surface is stronger because of mechanical gripping and increased surface area [73]). The filling of pores and crevices may be aided by increasing the driving pressure behind the liquid. However, this too is limited by the viscosity of the liquid in that additional force is required to push a more viscous liquid per Newton's law of viscous flow

$$\tau = \eta * \frac{d\gamma}{dt} \tag{7}$$

where $d\gamma/dt$ is shear rate and τ is shear stress. Adhesion and wetting are rate-sensitive and the factors influencing this rate, such as viscosity and equilibrium wettability, should be considered for the dynamic process of sealing a friction stir welded lap joint.

The effect of fillers on adhesive bond strength is complicated. The addition of ceramic fillers may reduce the interfacial surface tension of the polymer with a ceramic surface (such as anodized aluminum) and thus improve the equilibrium wettability. However, the addition of fillers also increases the viscosity of a suspension of rigid particles η_s as per Einstein's equation [95]

$$\eta_s = \eta(1 + k_E\phi) \tag{8}$$

where η is the viscosity of the liquid without particles, Φ is the volume fraction of spherical particles, and k_E is a positive constant related to the shape of the particles equal to 2.5 for spheres.

Fillers may improve equilibrium wettability while increasing viscosity. These properties have conflicting effects on dynamic wettability. The effect of fillers on the mechanical properties and therefore the adhesive bond strength (per eq. 5) is highly varied depending on strength of the filler and wetting of the polymer to the filler material. Therefore, the effect of a filler in lap joint sealants is difficult to predict and may be situation dependent.

2. EXPERIMENTAL PROCEDURE

2.1. FABRICATION OF FRICTION STIR WELDS

Friction stir welded lap joints used for this investigation are equivalent to those used in a study by Van Aken et al. [3]. Lap joints were made by welding 2024-T8 top-skin of 20.3 cm (8 in) width, 0.9 m (3 ft) length, and 3.18 mm (0.125 in) thickness to 357-T6 cast T-rails of 0.9 m (3 ft) length (see Figure 2.1). The region of material that is joined occupies a portion of the faying surfaces leaving faying surface gaps on either side of the weld (see Figure 2.1b). Aluminum components were sulfuric acid anodized prior to welding. Two anodization procedures were investigated (Boeing specification PS13201): a standard sulfuric acid anodization (type 2, class 1); a thin film sulfuric acid anodization (type 2A, class 1). The flat top of the T-rail onto which the top-skin is joined is milled to improve flatness prior to anodization and welding.

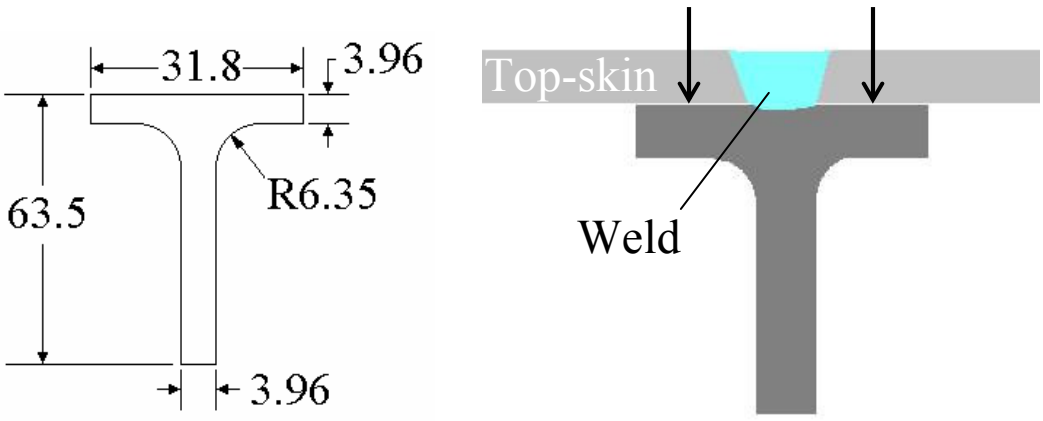

Figure 2.1. (a) Cross-section schematic with dimensions in mm of 357-T6 T-rail. (b) Cross-section schematic of friction stir welded lap joint. Arrows denote faying surface gaps.

Linear welds were made using an FSW tool (FSW0033-2003) designed by the Boeing Company. The tool is designed for 3.18 mm (0.125 in) thick top-skins and for welding with 0º tool tilt. A custom FSW unit owned and operated by the Boeing Company was used and is capable of maintaining constant downward force during welding. Top-skins were clamped to the T-rails using a series of evenly spaced pneumatic finger clamps (see Figure 2.2). Finger clamps were spaced every 19 cm (7.5 in) along the weld direction and each applied an estimated 4.5 kN (1,000 lbs).

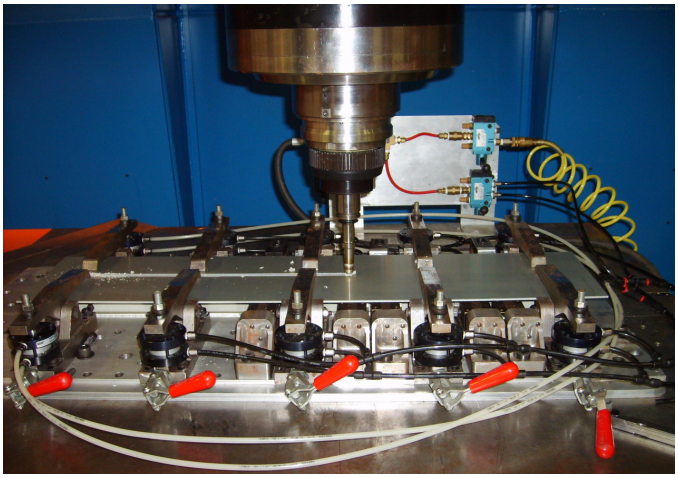

Figure 2.2. Finger clamp arrangement that applies direct pressure over faying surface gaps during welding.

Some welds were formed with a sealant material to fill the faying surface gaps. Corvel™ White nylon-11 and DAPCO™ rubber were used as sealants. Corvel™ White was supplied by Rohm and Haas Powder Coatings (product code 78-1001) and is an electrostatic spray grade powder composed of nylon-11 with 10-15 % TiO_2 and 1-5 % amorphous SiO_2. The average particle size of Corvel™ powder is 65 µm as reported by the manufacturer. DAPCO™ silicone rubber is a two-part room temperature vulcanizing

elastomer manufactured by Cytec Industries as a high temperature ablative sealant (product code 2900).

The nylon-11 sealant was applied to the T-rail prior to welding as a pre-fabricated sheet. The method for fabricating sealant sheet is described in Appendix A. Sealant sheet thickness prior to welding was 150 - 200 μm (0.006 - 0.008 in) for welds with prior thin film sulfuric acid anodization. For bare welds and welds with prior standard sulfuric acid anodization, sealant thickness prior to welding was 100 – 130 μm (0.004 – 0.005 in). The rubber sealant was applied to the T-rail prior to welding in the uncured state and allowed to cure after welding.

The following welding parameters were varied in order to achieve proper welds with minimal flash and controlled heat input: tool rotation speed; feed rate; downward force. Baseline welds (without sealant) and welds with DAPCO^{TM} rubber sealant were performed at feed rate of 4.2 mm/s (10 in/min), 900 rotations per minute (rpm), and 6.9 kN (1550 lbs) downward force. For welds containing nylon-11 sealant, a significantly higher heat index was used by reducing feed rate to 3.6 mm/s (8.5 in/min) and increasing rotation speed to 1100 rpm (see eq. 1). One or two welds of 61 – 76 cm (24 – 30 in) length were made with each combination of anodization and sealant used for testing. A metallographic specimen of the each weld was prepared from a section 25 – 38 cm (10 – 15 in) from the weld plunge for microstructural analysis. Nomarski optical images were used to estimate grain size.

2.2. MECHANICAL TESTING OF LAP JOINTS

2.2.1. Tensile Testing. Tensile testing was conducted on 2-4 specimens of each weld. Lap joints were sectioned into 2.5 or 3.8 cm (1 or 1.5 in) weld coupons for tensile testing. The top-skin ears were clamped on both sides of the weld and were separated by a distance of 3.68 cm (1.45 in) as shown in Figure 2.3. The T-rail was clamped and displacement-controlled tension was applied at 0.02 mm/s. The load cell was calibrated per ASTM E 74 – 06 [96] and grips were aligned such that the fixture complies with ASTM E 1012 – 05 [97] for tensile and fatigue testing. Calibration and alignment was maintained throughout all mechanical testing. Maximum tensile load per length of weld and load required to break sealant bonds were determined via tensile testing. Nylon sealed welds with prior thin film sulfuric acid anodization were tested in both the as-welded condition and after a heat treatment at 200 ºC for 10 min to repair the nylon-aluminum adhesive bonds.

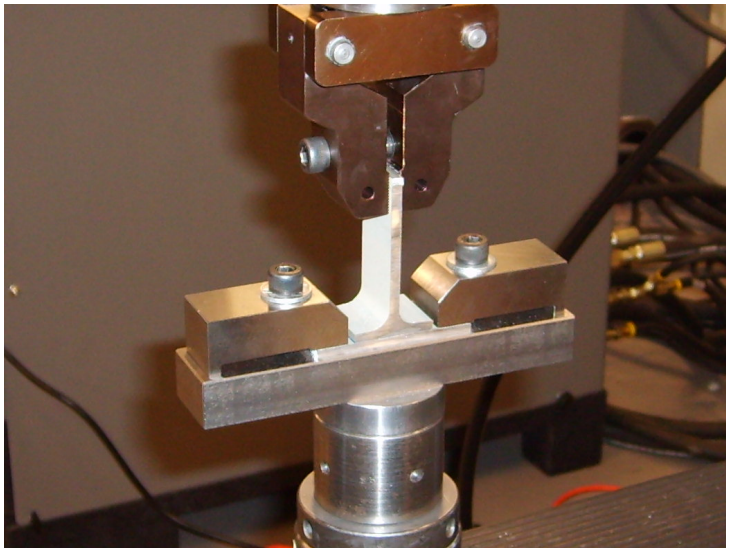

Figure 2.3. Arrangement for tensile testing of weld coupons. Top-skins are clamped via ear clamps.

2.2.2. Ambient Fatigue Testing. Preliminary ambient fatigue testing was conducted using 3.8 cm (1.5 in) weld coupons. The preliminary fatigue fixture elements were made of steel. Loading and clamping was performed similarly to tensile testing with 3.68 cm (1.45 in) clamp separation (see Figure 2.4a). Subsequent fatigue testing was conducted on 2.5 cm (1 in) weld coupons using aluminum ear clamps in an aluminum fixture designed for immersion testing (see Figure 2.4b). The T-rail grip was made of 17-4 Ph stainless steel and is attached via a universal joint to minimize misalignment effects (in contrast to the rigid upper grip used with the steel test fixture).

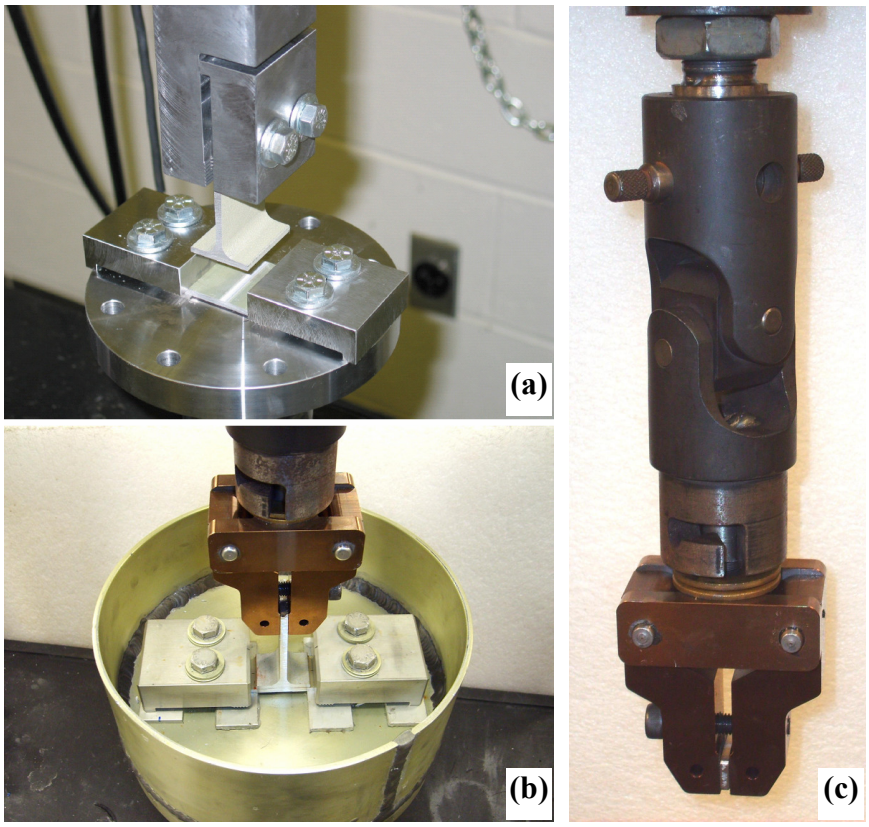

Figure 2.4. (a) Preliminary ambient fatigue tests were conducted with steel fixture with rigid upper clamp. (b) Subsequent ambient fatigue tests and corrosion fatigue tests were conducted with aluminum fixture with (c) steel upper clamp on universal joint.

Ambient fatigue testing was conducted at 8 Hz cycling frequency with a stress ratio R = 0.1 (ratio of minimum load to maximum load). Preliminary tests were performed at maximum cycling load of 78.8 N/mm (450 lbs/in) of weld on 3.8 cm (1.5 in) weld coupons using the steel fixture with rigid upper grip. Preliminary testing was conducted on welds with Corvel™ nylon-11 sealant that received standard sulfuric acid anodization prior to welding. Eight to nine specimens were tested for each condition. A 2-parameter Weibull statistics method was used to analyze the fatigue life for all fatigue testing conditions. Crack initiation life was estimated by observing the first deviation in loop displacement (displacement at maximum load minus displacement at minimum load). Results of ambient fatigue testing are compared with those reported by Van Aken et al. [3] using equivalent welding and testing practice without sealant comparing welds with no prior anodization to those with standard sulfuric acid anodization. A complete list of the fatigue experimental design is shown in Table 2.1.

Subsequent ambient fatigue testing was conducted using the aluminum test fixture, 2.5 cm (1 in) weld coupons, and a maximum cycling load of 52.5 N/mm (300 lbs/in) of weld. All other parameters were maintained with respect to preliminary tests. Testing was conducted to compare three welding conditions all with thin film sulfuric acid anodization prior to welding: no sealant; Corvel™ nylon-11 sealant; DAPCO™ rubber sealant. Eight specimens were tested from each condition and the fatigue life data was analyzed using Weibull statistics. Nylon sealed welds were tested after a repair heat treatment at 200 ºC for 10 min.

A study was conducted to compare the fatigue testing fixtures used for preliminary and subsequent testing. Welds fabricated with DAPCO™ rubber sealant and

thin film sulfuric acid anodization were used. Welding was conducted with the same parameters as welds without sealants: 4.2 mm/s (10 in/min); 900 rpm; 6.9 kN (1550 lbs). 2.5 cm (1 in) coupons of these welds were tested at 78.8 N/m (450 lbs/in) of weld at 8 Hz cycling frequency and 0.1 stress ratio. Six specimens were tested with the steel fixture and six were tested with the aluminum fixture. For each fixture, three specimens were tested with the universal grip and three with the rigid grip.

Table 2.1. Fatigue Testing Experimental Design

Sulfuric Acid Anodization	Sealant	Fixture	Peak Load (lbs/in weld)	Environment	Mask
*Bare**	*None**	*Steel**	*450**	*Ambient**	
*Standard**	*None**	*Steel**	*450**	*Ambient**	
Standard	Corvel™	Steel	450	Ambient	
Thin Film	DAPCO™	Steel	450	Ambient	
Thin Film	DAPCO™	Aluminum	450	Ambient	
Thin Film	None	Aluminum	300	Ambient	
Thin Film	Corvel™	Aluminum	300	Ambient	
Thin Film	DAPCO™	Aluminum	300	Ambient	
Thin Film	None	Aluminum	300	3.5 % NaCl	
Thin Film	None	Aluminum	300	3.5 % NaCl	X
Thin Film	Corvel™	Aluminum	300	3.5 % NaCl	
Thin Film	Corvel™	Aluminum	300	3.5 % NaCl	X
Thin Film	DAPCO™	Aluminum	300	3.5 % NaCl	
Thin Film	DAPCO™	Aluminum	300	3.5 % NaCl	X

**Experiment by Van Aken et al.* [3]

2.2.3. Corrosion Fatigue Testing. In situ corrosion fatigue tests were conducted using neutral 3.5 % NaCl solution prepared per ASTM G 44 – 99 [98]. Each specimen was immersed in fresh solution during the fatigue testing and tested until failure at a maximum cycling load of 52.5 N/mm (300 lbs/in) of weld and cycling frequency of 4 Hz. All other testing parameters matched those of ambient fatigue testing. Corrosion fatigue testing was conducted using 2.5 cm (1 in) weld coupons and some coupons were masked in order to protect aluminum surfaces exposed from specimen sectioning and the exposed weld scroll surface (see Figure 2.5a). A low modulus polyurethane DAP® aquarium sealant manufactured by Dow Corning® was used for the mask. Three welding conditions were compared, and all were thin film sulfuric acid anodized: no sealant; Corvel™ nylon-11 sealant; DAPCO™ rubber sealant. Nylon sealed welds were tested after a repair heat treatment at 200 ºC for 10 min. Eight specimens of each condition were tested, six of which were masked and two of which remained unmasked. Of the six masked nylon sealed weld coupons, two received additional masking across the sealant fillet (see Figure 2.5b). Weibull statistics were used to analyze the fatigue life data.

Sample fatigue fractures from failed weld coupons without sealant were examined in a Hitachi S-570 scanning electron microscope. Images were obtained with secondary electron detection at 15 kV accelerating voltage and 20 mm working distance. Two fracture surfaces were examined: one of a specimen tested in ambient fatigue conditions; one of a specimen tested in corrosion fatigue conditions.

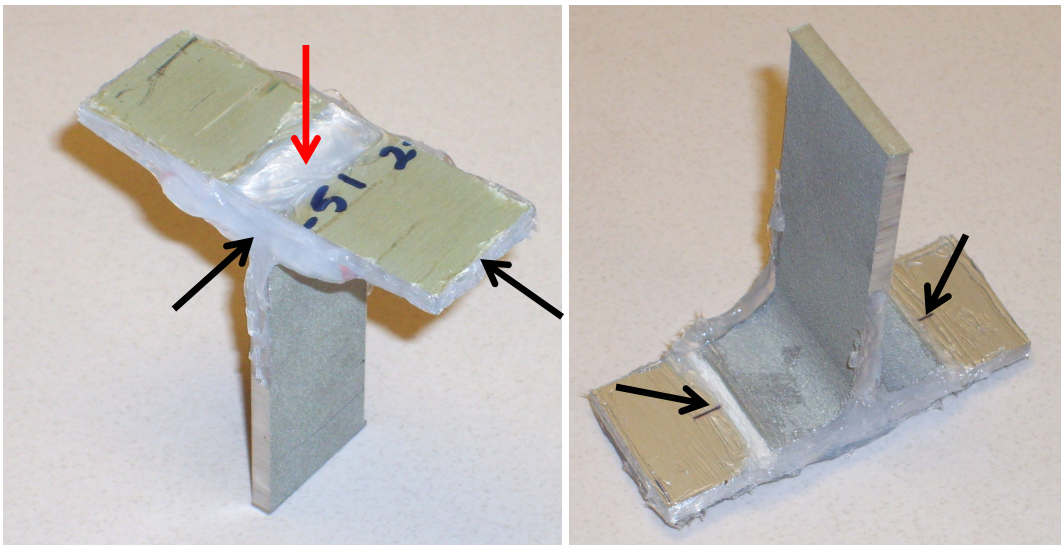

(a) **(b)**

Figure 2.5. (a) Fatigue test specimen in which exposed aluminum surfaces are masked. Exposed surfaces due to sectioning are denoted by black arrows and the weld scroll surface is denoted by the red arrow. (b) Additional masking of the sealant fillet was applied to two of the masked weld coupons with nylon sealant.

2.3. EVALUATION OF SEALANT PROPERTIES

2.3.1. Thermal Analysis. Pure nylon-11 and Corvel™ White materials were evaluated for glass transition temperature and melting temperature using differential scanning calorimetry per ASTM D 3418 – 08 [99]. Pure nylon-11 was supplied by Sigma-Aldrich® in the form of 3 mm diameter beads. Samples were cooled to 0 ºC prior to measurements and heated at 20 ºC/min to 210 ºC. Samples were restricted to sizes less than 10 mg in order to reduce lag effects due to low thermal conductivity.

2.3.2. Tensile Testing. Tensile testing of polymers was conducted to determine tensile properties of each sealant material for finite element analysis and for comparison. Five specimens of each material were made by casting the polymer in an aluminum mold 7.5 cm (3 in) diameter by 15 cm (6 in) long with a 2.5 cm (1 in) diameter hole in a

furnace at 220 ºC for 1-2 hours. After solidifying and cooling, polymer specimens were machined to round tensile bars of 6.4 mm (0.25 in) diameter gage section (see Figure 2.6). Tests were conducted per ASTM D 638 – 08 [100] at an elastic strain rate of 0.08 mm/mm/min to determine tensile properties of each material.

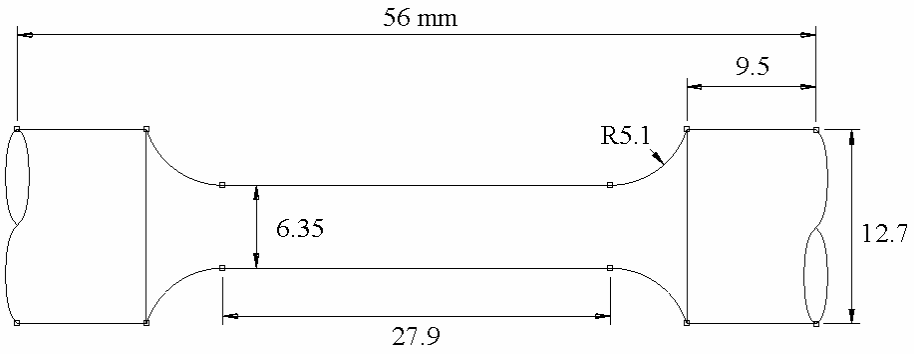

Figure 2.6. Dimensions in mm of round tensile bar for tensile testing of polymer sealant materials.

2.3.3. Stress Relaxation Testing. Compression testing of polymers was conducted to determine stress-relaxation rates of each sealant material per ASTM E 328 – 02 [101]. Two specimens of each material were cast in 2.5 cm (1 in) diameter by 2.5 – 5 cm (1-2 in) long cylinders and were ground flat to 2.5 cm (1 in) length. Specimens were compressed to –2.0 % strain at 1.4 MPa/s stress rate and held for 48 - 72 hours. The stress required to maintain compression was recorded periodically while the strain was held constant.

2.3.4. Adhesive Bond Strength Testing. Adhesive bond strength testing was performed to evaluate bond strength of each sealant with anodized aluminum in various conditions. Adhesive bonds were formed between round studs of 2.8 cm (1.1 in) diameter

(see Figure 2.7). Round studs were thin film sulfuric acid anodized prior to forming adhesive bonds. Adhesive bonds were formed in an assembly fixture. Round studs were inserted in the assembly fixture and heated to 255 ºC with a clamp heater (see Figure 2.8). The sealant material was then added and the studs were pressed together with 5 lbs of compressive force within 10-20 s of removal of the heater. The force was applied until the specimens were cooled. Sealant materials used include pure nylon-11 and Corvel^{TM} nylon-11. Data was collected only from specimens with final adhesive thickness ranging from 0.1 to 0.2 mm (0.004 to 0.008 in) after solidification and cooling to reduce thickness effects and cohesive failure in the polymers. Data from failures that were not predominantly adhesive in nature were discarded. Specimens were pulled in tension at 0.002 mm/s per ASTM D897 – 08 (see Figure 2.9) [102]. Testing was conducted at room temperature 24 ºC (for pure nylon-11 and Corvel^{TM} nylon-11), at reduced temperatures (-65 and -20 ºC, -85 and -4 ºF) and at elevated temperatures every 20 ºC (36 ºF) between

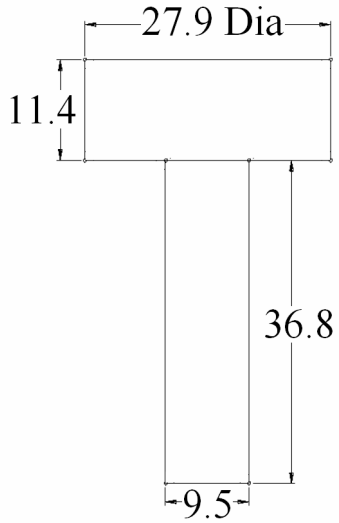

Figure 2.7. Dimensions in mm of round stud for adhesive bond testing.

(a) **(b)**

Figure 2.8. Fixture for the assembly of adhesive bonds. (a) Round studs were heated to 255 ºC in a clamp heater. (b) In 20 s after reaching the temperature, the polymer was added and the round studs were pressed together until cool.

60 and 200 ºC (140 and 212 ºF). Reduced and elevated temperature testing was conducted in an environmental chamber with Corvel^{TM} nylon-11 only. Extenders were used to grip specimens in the chamber (see Figure 2.9b).

2.3.5. Wettability Estimation. Contact angles of sessile deionized water drops on thin film sulfuric acid anodized aluminum, Corvel^{TM} nylon-11, and pure nylon-11 were measured per ASTM D 7334 – 08 [103]. Surfaces were cleaned with acetone, rinsed with deionized water, and dried prior to measurements. The contact angle θ_w is related to the surface tension of the solid γ_β, the surface tension of the liquid γ_α, and the

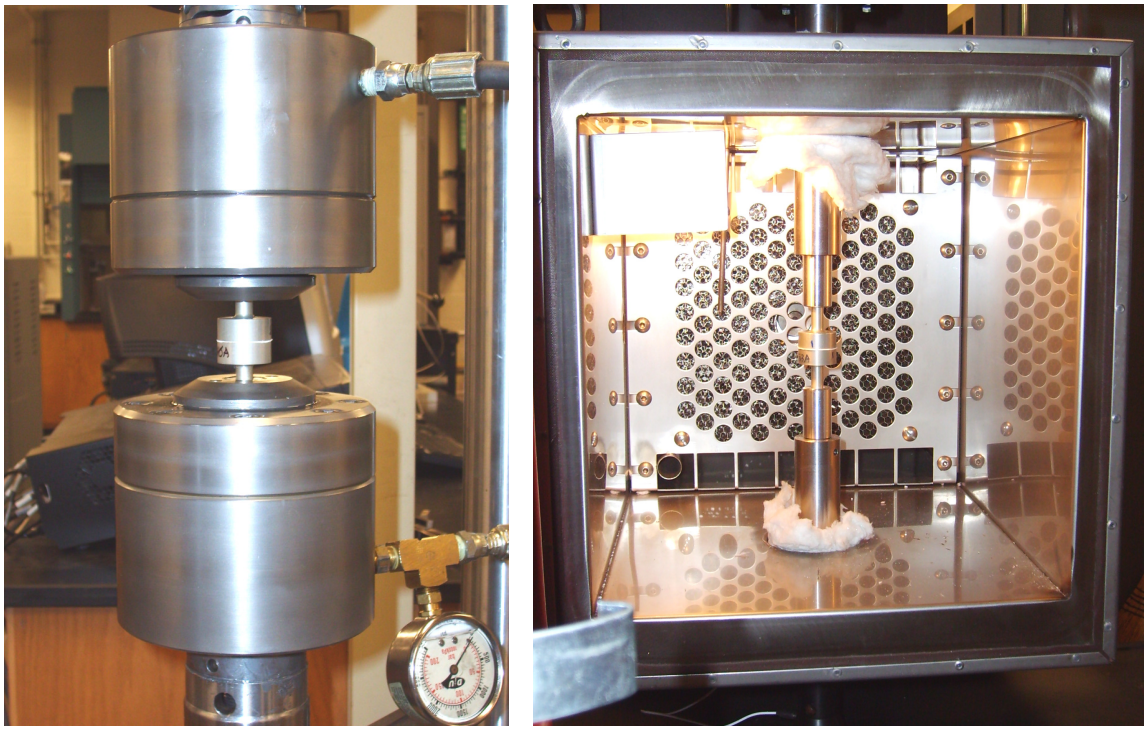

(a) **(b)**

Figure 2.9. Adhesive bond strength testing practice. Aligned hydraulic grips are used to secure round studs and are pulled at 0.002 mm/s. (a) Room temperature testing configuration and (b) reduced and elevated temperature test configuration using environmental chamber and grip extenders.

interfacial tension between the solid and liquid $\gamma_{\alpha\beta}$ by [104]

$$\cos\theta_w = \frac{\gamma_\beta - \gamma_{\alpha\beta}}{\gamma_\alpha} \tag{9}$$

The interfacial tension can be predicted from the surface tension of the liquid and solid by the geometric mean equation (valid between a low- and a high-energy material) [73]

$$\gamma_{\alpha\beta} = \gamma_\alpha + \gamma_\beta - 2\left(\sqrt{(1-x_\alpha)(1-x_\beta)\gamma_\alpha\gamma_\beta} + \sqrt{x_\alpha x_\beta \gamma_\alpha \gamma_\beta}\right) \tag{10}$$

where x_α and x_β are the polarities of the liquid and solid respectively.

The polarity and surface tension of water are 0.70 (unitless) and 72.8 mJ/m^2, respectively [73]. The polarity of the nylon-11 polymers is estimated at 0.344, which is

the measured polarity for nylon-6/6 [105]. Solving for eqs. 9 and 10 simultaneously for sessile water drop contact angle on each polymer estimates the room temperature surface tension of each polymer. The surface tension of each polymer in the melt (at 225 ºC) can be predicted by observing surface tension trends for nylon-6/6 (melting point ~180 ºC). The average change in surface tension of nylon-6/6 between 20 ºC and 300 ºC is -0.06 $mJ/m^2/ºC$ [105].

An estimate of the anodized layer polarity is required to calculate the surface tension of the thin film sulfuric acid anodized aluminum. Traini et al. report surface tension of anodized aluminum of 50.5 mJ/m^2 and polarity of 0.14 by water drop contact angle [106]. The surface tension of the thin film sulfuric acid anodized aluminum can be estimated using the sessile water drop contact angle measurement and the estimated polarity of anodized aluminum, 0.14, in addition to the known values for water. Assuming the surface tension of the anodized aluminum is approximately constant between 20 and 200 ºC, the interfacial tension between each polymer melt and anodized aluminum can be predicted using the geometric mean equation (eq. 10).

2.4. FINITE ELEMENT MODELING

2.4.1. Baseline Modeling Parameters. Finite element analysis was conducted using Abaqus® software by Dassault Systèmes. Static modeling was used to evaluate crack tip stress intensity factors as a function of geometry, material, and applied load of friction stir welded lap joint fatigue specimens. The baseline model geometry and meshing used is shown in Figure 2.10. The baseline model is two-dimensional, with symmetry about the central load-direction axis. Clamping distance is held constant at

18.4 mm (0.725 in) away from the weld center (consistent with ear clamping in tensile and fatigue testing as shown in Figures 2.3 and 2.4). The distance x between the faying surface notch and the symmetry line was initially set at 2.0 mm (based on typical weld dimensions). Quadratic, reduced integration, plane strain quadrilateral elements were used throughout the bulk of the model. Near the faying surface notch, the mesh converges to form wedge elements around the crack tip. Elastic material properties were based on 2024 aluminum at 20 ºC: elastic modulus E = 72.4 GPa (10.5 Msi); Poisson's ratio v = 0.33 [107].

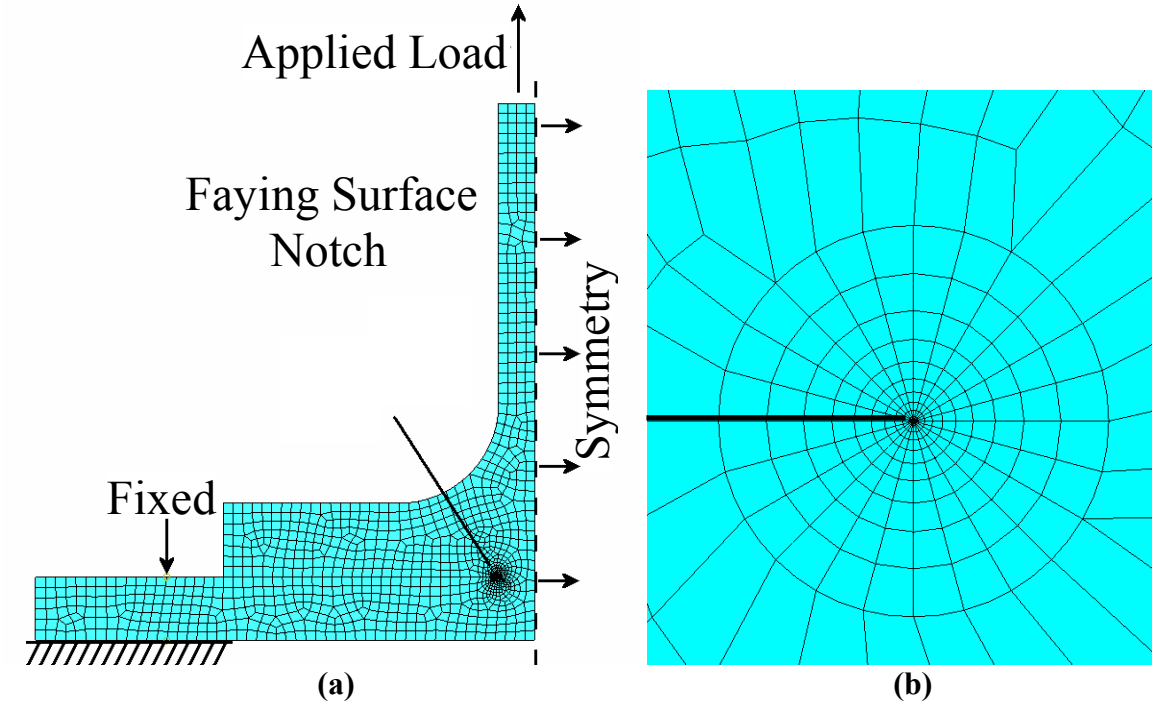

Figure 2.10. (a) Two-dimensional, finite element model mesh with symmetry. (b) Exploded view of crack tip mesh at faying surface notch.

2.4.2. Model Analysis Method. A static 78.8 N/mm (450 lbs/in) load is applied to the model. Baseline model stress distributions are shown in Figure 2.11. Crack tip analysis at the faying surface notch was used to quantify mode I, II, and III stress intensity factors K_I, K_{II}, and K_{III} and the energy release rate or *J*-integral. The *J*-integral is integrated along a contour Γ that surrounds the crack tip

$$J = \int_{\Gamma} (w dy - T_i \frac{\partial u_i}{\partial x} ds) \tag{11}$$

where w is strain energy density, ds is a length increment along the contour, T_i represents components of the traction vector, u_i represents components of the displacement vector, and x and y are Cartesian coordinates relative to the crack tip (see Figure 2.12a) [108]. The strain energy density is defined as

$$w = \int_0^{\varepsilon_{ij}} \sigma_{ij} d\varepsilon_{ij} \tag{12}$$

where σ_{ij} and ε_{ij} are the stress and strain tensors respectively. The traction vector T_i is defined as

$$T_i = \sigma_{ij} n_j \tag{13}$$

where n_j is the component of the unit vector normal to ds corresponding with the stress tensor component.

The *J*-integral is calculated in Abaqus® software using discrete steps along a contour of elemental nodes (see Figure 2.12b). The local crack Cartesian coordinates are specified in the model input. Five unique successive contours were used to verify convergence of *J*-integral. The *J*-integral is calculated in auxiliary components J_I, J_{II}, and J_{III} corresponding with pure mode I, II, and III related stresses. Stress intensity factors $\boldsymbol{K} = [K_I, K_{II}, K_{III}]$ can be determined from these components for a linear elastic material by

$$\mathbf{K} = \mathbf{B} \bullet \mathbf{J} = \mathbf{B} \bullet [\, J_I, J_{II}, J_{III}]^T \tag{14}$$

where ***B*** is defined for elastic, isotropic, homogeneous materials as

$$\mathbf{B} = \begin{bmatrix} \frac{1}{E} & 0 & 0 \\ 0 & \frac{1}{E} & 0 \\ 0 & 0 & \frac{1}{2G} \end{bmatrix} \tag{15}$$

for plane stress condition and

$$\mathbf{B} = \begin{bmatrix} \frac{1-\nu^2}{E} & 0 & 0 \\ 0 & \frac{1-\nu^2}{E} & 0 \\ 0 & 0 & \frac{1}{2G} \end{bmatrix} \tag{16}$$

for plane strain condition where G is the shear modulus. This is based on the established relationship between J and $\mathbf{K}$ [109-110]:

$$J = \frac{1}{8\pi} \mathbf{K}^{\mathrm{T}} \bullet \mathbf{B}^{-1} \bullet \mathbf{K} \tag{17}$$

For a two-dimensional model, K_{III} and J_{III} are zero.

Crack propagation direction θ_p is determined from stress intensity factors by

$$\cos\theta_p = \frac{3K_{II}^2 + \sqrt{K_I^4 + 8K_I^2 K_{II}^2}}{K_I^2 + 9K_{II}^2} \tag{18}$$

Several iterations of the model are performed adjusting the input crack propagation direction until it approximately matches the calculated θ_p from the model output. The converged model stress intensity factors are taken as the final values for the model.

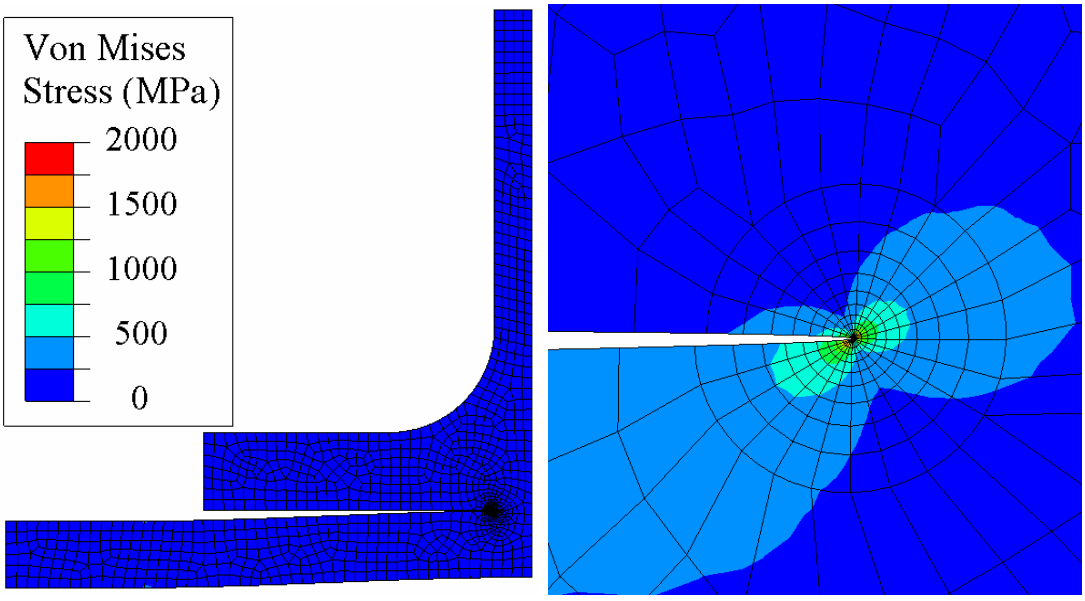

(a) **(b)**

Figure 2.11. (a) Stress distribution with 78.8 N/mm applied load (450 lbs/in) at 5x deformation magnification. (b) Highest stresses are located at the crack tip corresponding with fatigue crack initiation observations.

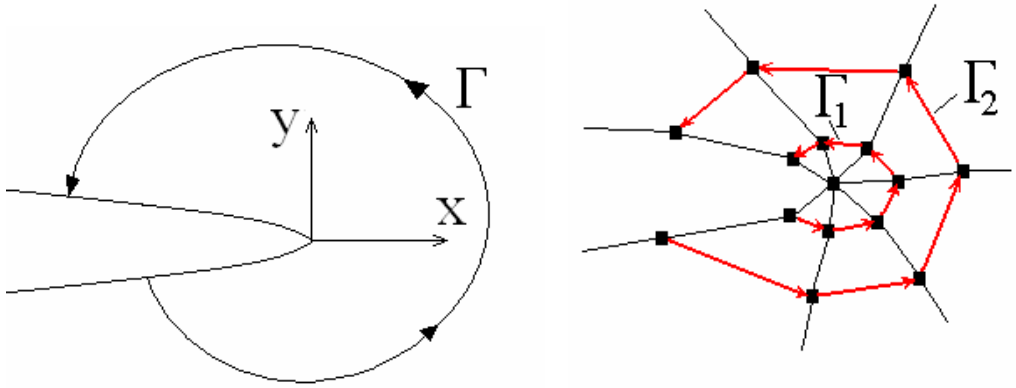

(a) **(b)**

Figure 2.12. (a) *J*-integral contour around crack tip is path independent [111]. (b) Multiple, unique contours are used in finite element crack tip analysis.

2.4.3. Modeling Parameter Study. Modeling parameters were investigated to evaluate the parametric dependency of the baseline model. The following parameters were varied independently and the resulting stress intensity factors were compared with those of the baseline model: three-dimensional vs. two-dimensional model; elastic material properties; elastic-plastic material vs. elastic material. Additionally, the effect of applied load was evaluated.

Three-dimensional models were 2.54 cm (1.0 in) and 3.81 cm (1.5 in) deep with symmetry at half-depth (see Figure 2.13). Stress intensity factors along the depth of the crack model were compared with two-dimensional stress intensity factors. Results of the baseline model (based on elastic properties of 2024) are compared with results of using elastic properties for 357: E = 71.7 GPa (10.4 Msi); ν = 0.33 [107]. Elastic-plastic material parameters used were based on properties for 2024-T6 at 24 ºC [107]: yield strength σ_y of 393 MPa (57 ksi); tensile strength σ_u of 476 MPa (69 ksi); elongation to fracture of 10 %. Material stress-strain relationship is shown in Figure 2.14. Only the J-integral can be calculated with elastic-plastic material. Therefore, the J-integrals at the crack tip were compared with the baseline elastic material model. The effect of applied load for the baseline elastic model and for the elastic-plastic model are evaluated at various applied loads between 0 and 78.8 N/mm (450 lbs/in).

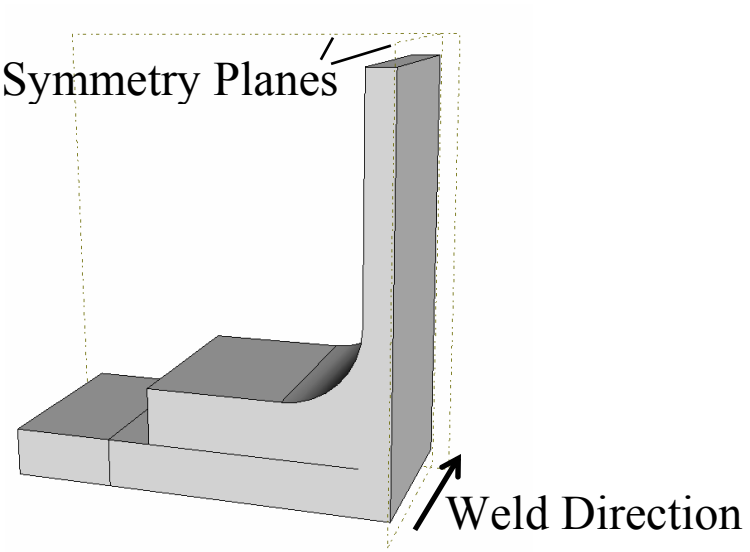

Figure 2.13. Three-dimensional model of 2.54 cm (1.0 in) depth. Symmetry planes are oriented vertically along weld direction and orthogonal to weld direction.

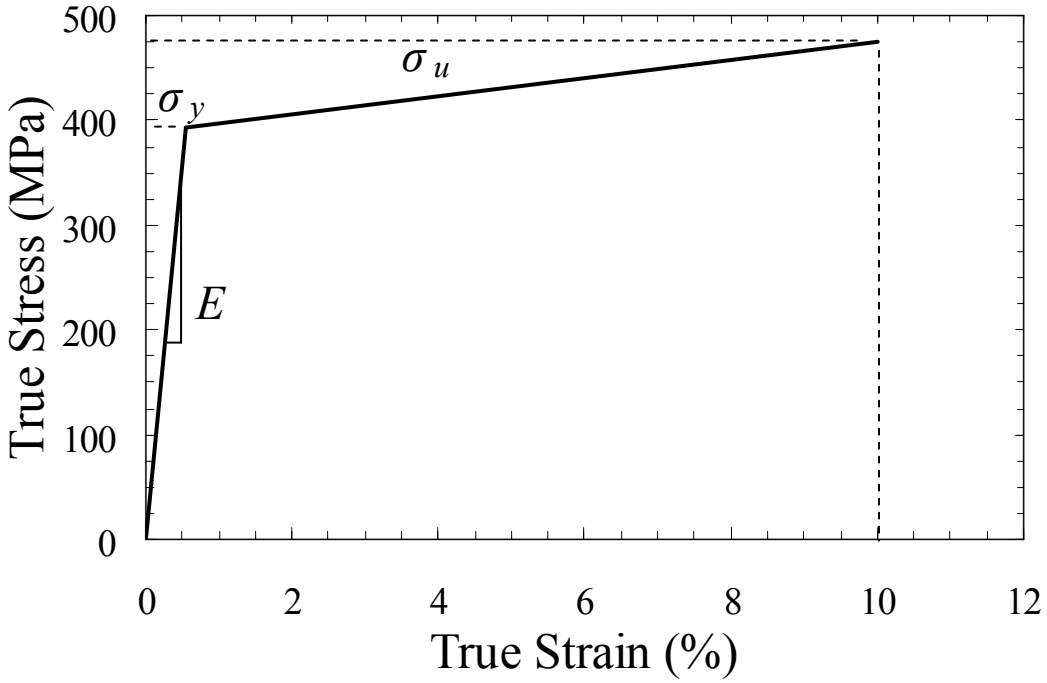

Figure 2.14. Stress-strain behavior of elastic-plastic material for comparison with elastic material model. Material properties are based on 2024-T6 [18].

2.4.4. Model Geometric Study. The effect of a hook defect on stress intensity factors was investigated. A partial hook and a full hook model were compared with the baseline model (see Figure 2.15). Geometric parameters for each model were varied independently to assess their influence on stress intensity factors. For each model the following parameters were varied when applicable: the half-weld width x (distance between faying surface notch and symmetry line); the hook intrusion angle θ_h; the vertical hook intrusion depth y; and the hook radius r.

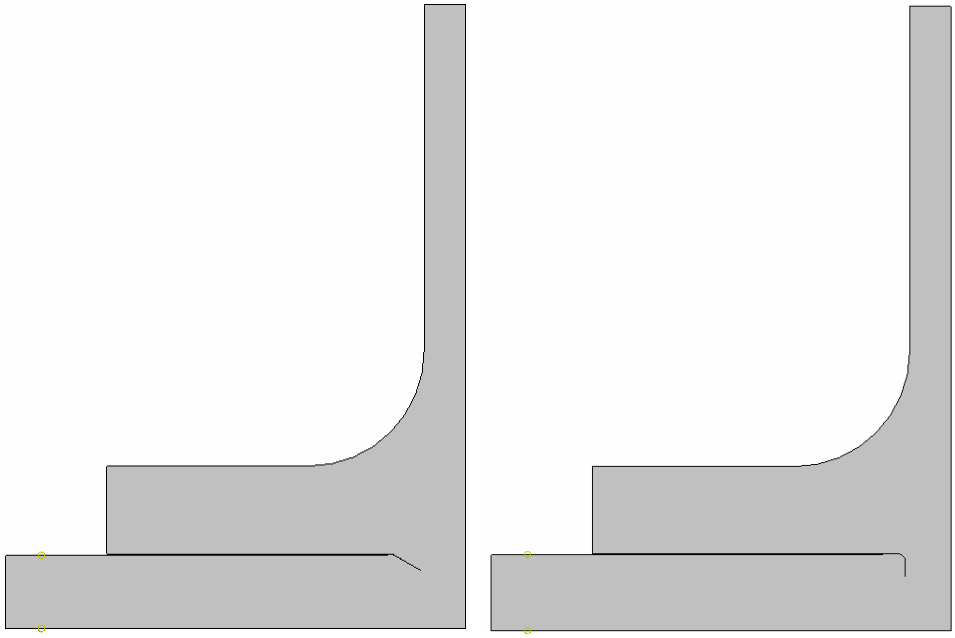

(a) **(b)**

Figure 2.15. Geometry for (a) partial and (b) full hook defect models for comparison with baseline model. Geometric parameters were varied for (c) baseline, (d) partial and (e) full hook models.

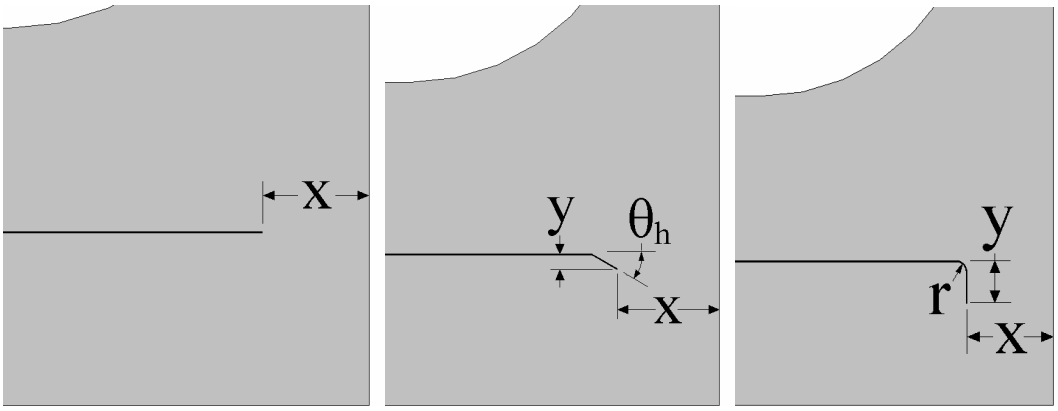

(c) **(d)** **(e)**

Figure 2.15. (cont.) Geometry for (a) partial and (b) full hook defect models for comparison with baseline model. Geometric parameters were varied for (c) baseline, (d) partial and (e) full hook models.

2.4.5. Sealant Analysis. The effect of bonded sealant was investigated. Sealant material elastic properties were estimated from tensile testing: E = 1.2 GPa (174 ksi); v = 0.3. Sealant layer thicknesses t of 0.1 mm (0.004 in) and 0.2 mm (0.008 in) were modeled based on weld observations. Sealant models include the baseline flat crack model and the full hook model with the sealant added (see Figure 2.16). Crack tip stress intensity factors were measured for baseline crack tip dimensions with g = 0.5 mm and x = 2.0 mm and for hook model dimensions with gap size g = 0.5 mm, x = 2.0 mm, r = 0.1 mm, and y = 0.5 mm. An additional model was used to analyze the effects of partial sealant filling. For this model, the sealant only filled the closest half of the faying surface gap to the weld, baseline crack tip dimension were used, and t = 0.1 mm.

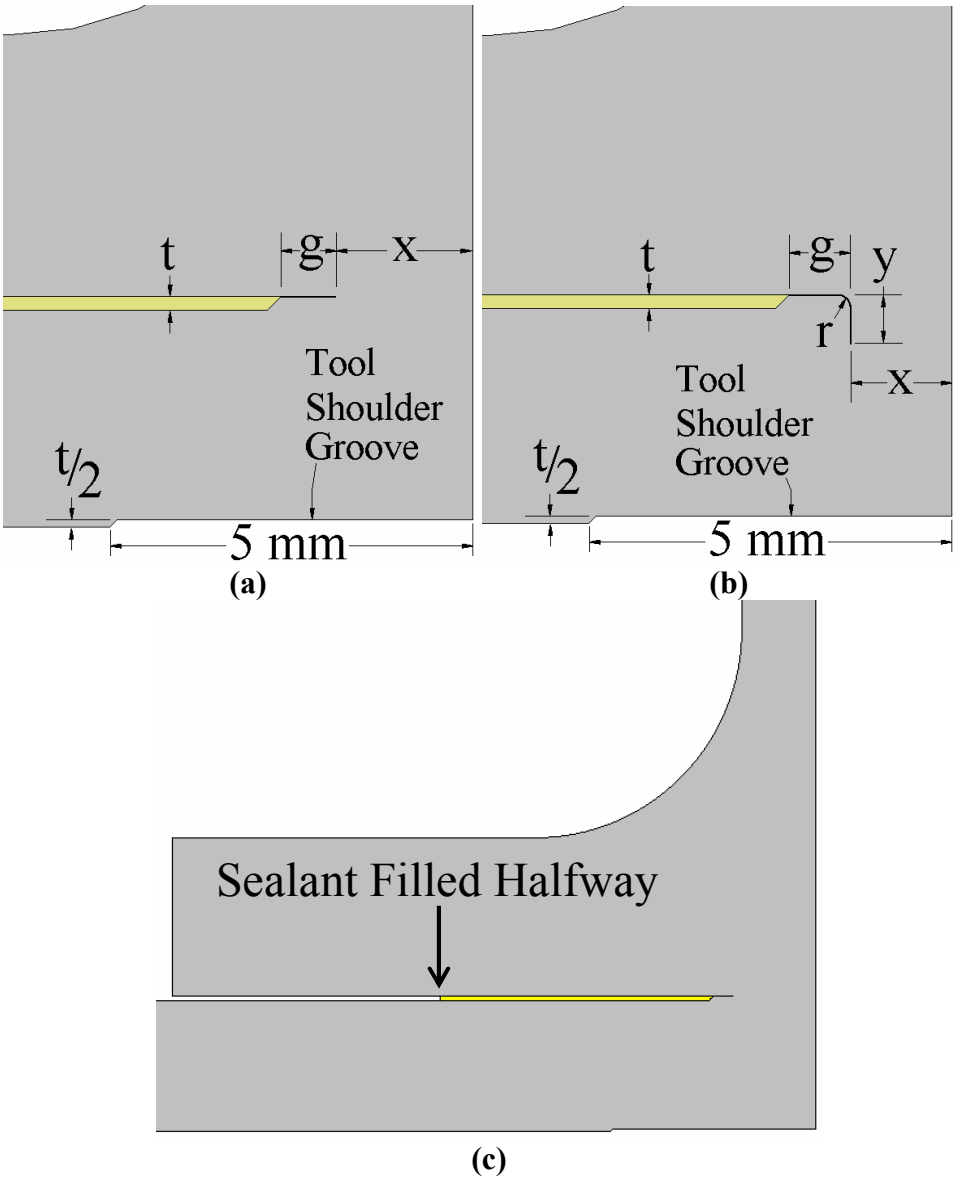

Figure 2.16. Geometry of crack tip for (a) flat and (b) hook models with complete fill sealant and (c) model for partial fill sealant.

2.4.6. Asymmetric Considerations. An asymmetric model was used to investigate the effect of crack propagation on crack tip stress intensity factors and the effect of grip restriction (see Figure 2.17). Due to asymmetry, the applied load has a tendency to bend the T-rail portion of the weld coupons. Two load constraints were modeled: with restricted horizontal displacement of the top of the T-rail; with free

horizontal displacement of the top of the T-rail. The two constraint models are intended to represent the rigid upper grip of the preliminary fatigue test arrangement and the universal joint upper grip of the subsequent fatigue test arrangement. For both cases, the applied load direction is maintained in the vertical axis (does not rotate with the T-rail).

The advancing side was modeled with a partial hook in which the distance between the crack tip and the centerline x_a = 2.0 mm, the hook intrusion angle θ_h = 30º, and the hook intrusion depth y = 0.35 mm. The retreating side was modeled with a flat interface with x_r = 2.0 mm. These dimensions are representative of observed welds. Crack tip stress intensity factors at the advancing and retreating side notches were determined and compared with stress intensity factors for the partial hook model and flat baseline model of similar crack tip geometries.

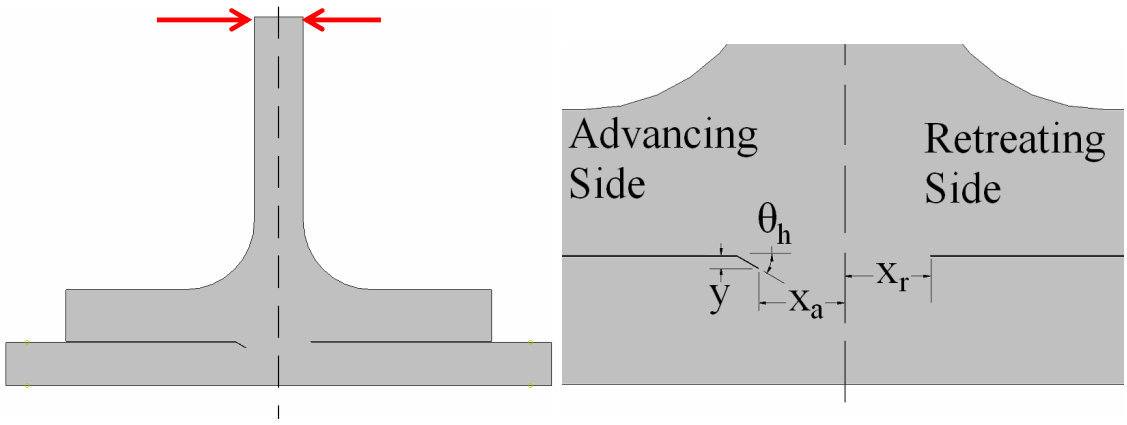

(a) **(b)**

Figure 2.17. (a) Asymmetric model with (b) exploded view of crack tips on retreating and advancing sides. Top of T-rail is denoted by arrows in (a) and is either restricted (rigid upper grip) or free (universal upper grip) in horizontal displacement.

The crack was advanced from the advancing side of the weld in the model. This corresponds with fatigue crack propagation observations. Crack growth at the advancing side was directed at 75º with the horizontal based on converged model results (eq. 18). The crack was advanced a total of 10 increments. The last increment of crack propagation represents complete cracking through the top-skin (total crack length = 2.90 mm). The stress intensity factors were calculated at the retreating side notch and advancing side crack tip for all crack growth increments for both the rigid upper grip and universal joint upper grip. The difference in predicted stress intensity factors with each grip arrangement is used to justify difference in observed fatigue propagation lives.

3. RESULTS

3.1. SEALANT MATERIAL PROPERTIES

3.1.1. Thermal Analysis. Differential scanning calorimetry results for pure nylon-11 and Corvel™ nylon-11 are shown in Figure 3.1. Heat flow or energy input per sample mass (W/g) is shown relative to heat flow at the melting peak. Results indicate the materials have similar melting temperatures of 190 ºC for Corvel™ nylon-11 and 193 ºC for pure nylon-11. Lower melting temperature suggests a reduced average molecular weight for Corvel™ nylon-11 compared with pure nylon-11. Due to the large crystallization hysteresis peaks immediately above the glass transition, glass transition temperature T_g could not be determined by inflection point methods. Instead, glass transition temperature was determined by evaluating the average of the temperature at first deviation from linearity after stabilization (T_d) and the temperature of the intersection (T_i) of the extrapolated linear region above the glass transition (see Figure 3.2). For both materials, the glass transition temperature calculated by this method is 43 ºC as compared to 46 ºC reported by the manufacturer (Sigma-Aldrich®) for pure nylon-11.

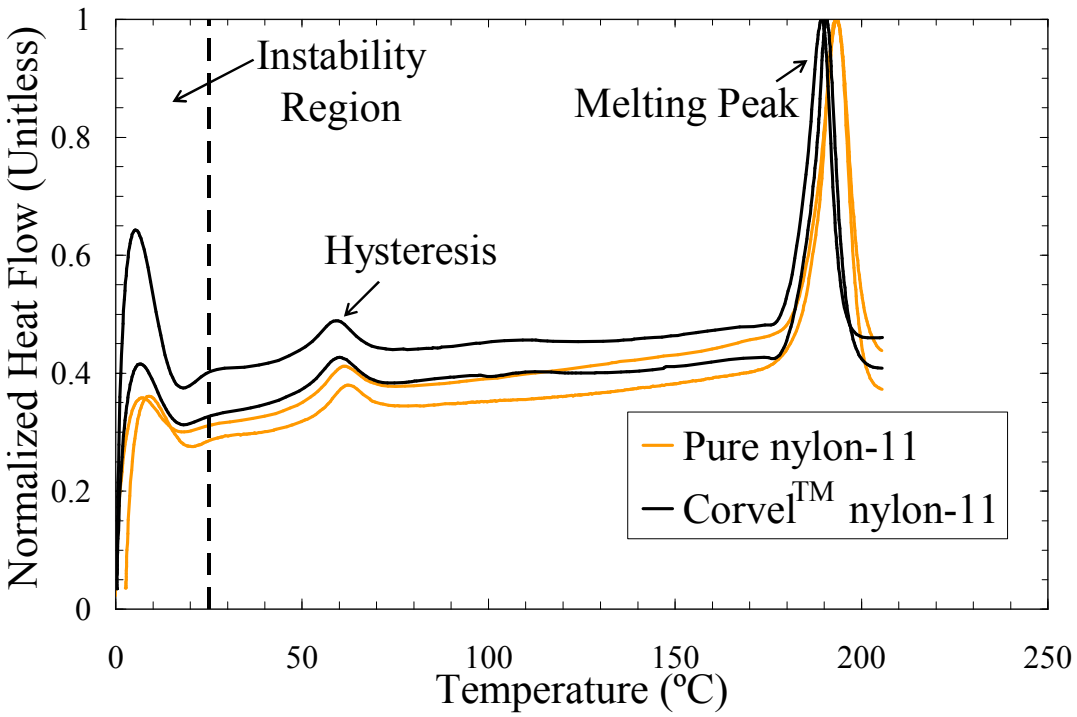

Figure 3.1. Differential scanning calorimetry results for pure nylon-11 and Corvel™ nylon-11.

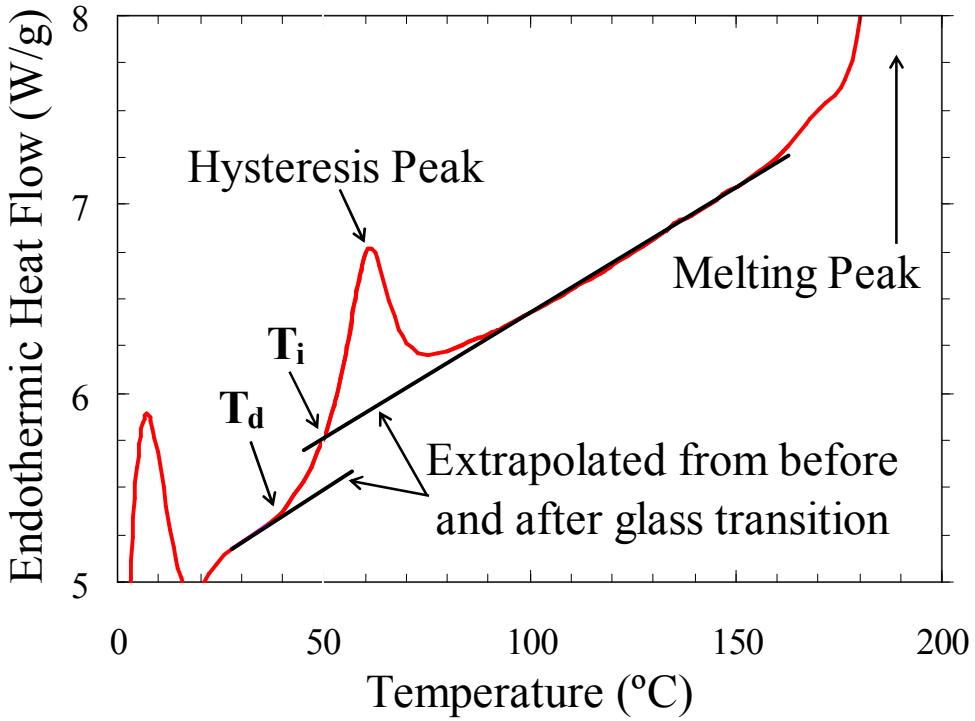

Figure 3.2. Method for calculating glass transition temperature. Example using pure nylon-11.

3.1.2. Adhesive Bond Strength Testing. The room temperature adhesive bond strengths of each sealant material, pure nylon-11 and Corvel™ nylon-11, on a thin film sulfuric acid anodized aluminum surface are listed in Table 3.1. Error is reported as ± one sample standard deviation.

Table 3.1. Room Temperature Adhesive Bond Strength Results

Sealant Material	Average Polymer Layer Thickness (μm)	Bond Strength (MPa)
Corvel™ nylon-11	130	18.7 ± 1.5
Pure nylon-11	140	17.9 ± 1.3

Failure mode for all room temperature bond strength test specimens was predominantly adhesive in nature, resulting in separation of the polymer from the anodization layer (see Figure 3.3). 0 – 20 % of the surface area of each failed bond appeared to fail cohesively. Adhesive bond strength of Corvel™ nylon-11 on thin film sulfuric acid anodized aluminum at various temperatures is shown in Figure 3.4. No significant delamination of the anodized layer was observed.

Adhesive bond strength results from testing in an environmental chamber appear to predict higher bond strength at room temperature than was observed from testing with hydraulic test fixture at room temperature. This may be due to the difference in fixture alignment compliance, and the difference in effective strain rate in displacement rate controlled testing. The environmental chamber testing was performed with more compliant grips and grip extenders. While both testing practices used 0.002 mm/s

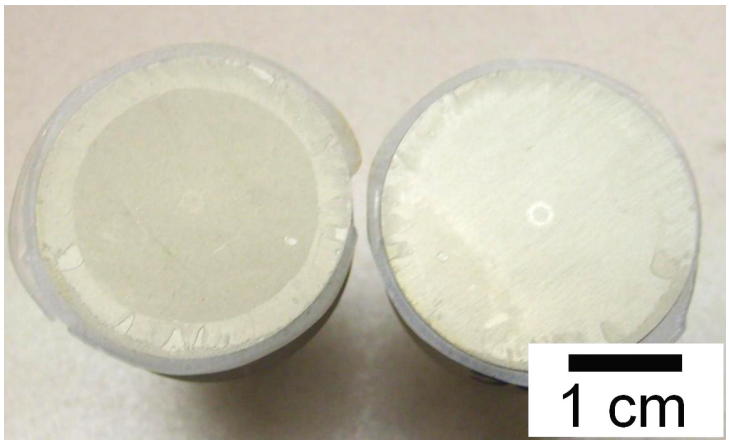

(a)

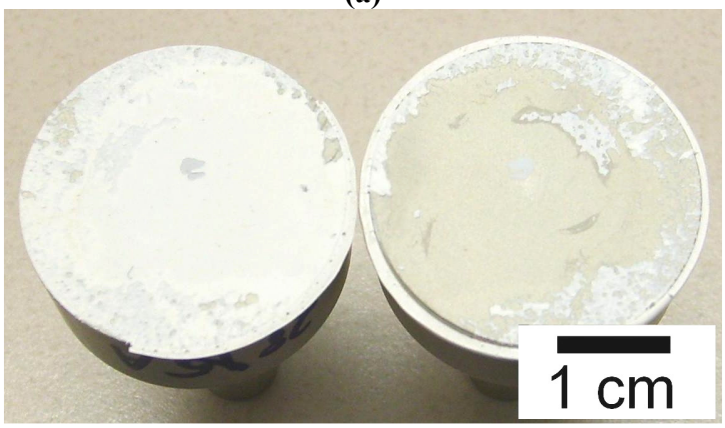

(b)

Figure 3.3. Sample failed adhesive bond specimens with (a) pure nylon-11 and (b) Corvel^{TM} nylon-11 on thin film sulfuric acid anodized aluminum tested at room temperature.

actuator displacement rate, the effective strain rate on the adhesive bond is likely lower for the environmental chamber testing than for the ambient testing.

There are two distinct transitions in bond strength related to the glass transition and melting of the polymer. With each transition is a distinct change in the failure mode of the adhesive bond. Failures in the middle 'rubbery' region, at temperatures between 100 and 190 ºC, are more adhesive in nature than at colder temperatures in the 'glassy' region. Failures above the melting temperature are mostly cohesive in nature, indicating

the polymer was liquid. The melt transition occurs near the melting point (190 ºC) while the glass transition occurs at about 100 ºC, significantly higher than the glass transition temperature (42 ºC). This may indicate that the glass transition is more sensitive to strain rate; the glass transition of bond strength is expected to approach the true glass transition temperature as strain rate decreases.

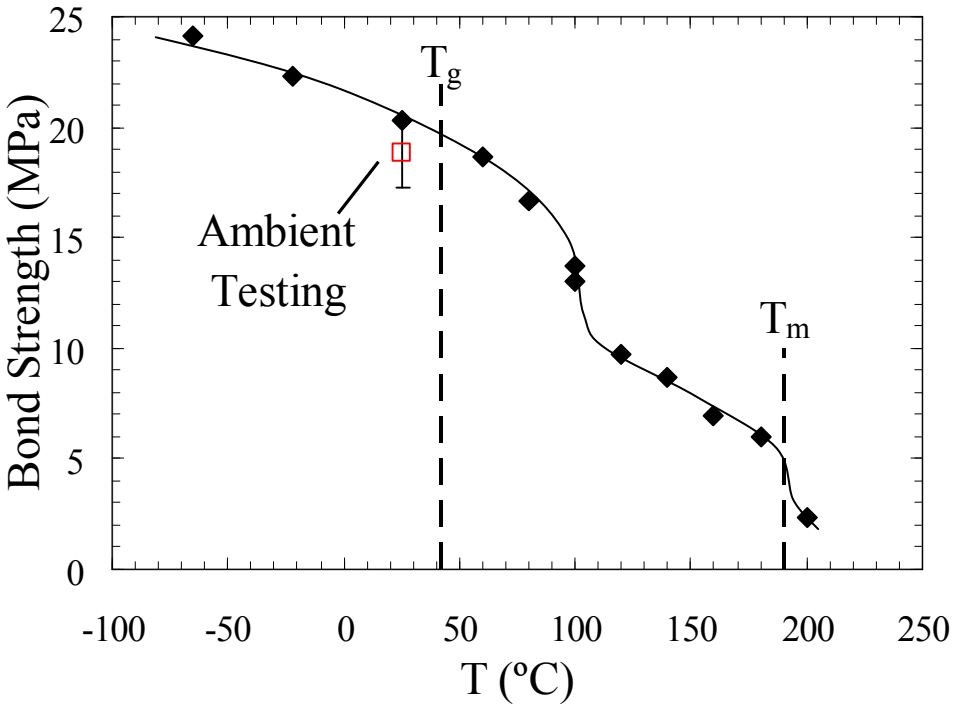

Figure 3.4. Adhesive bond strength of Corvel™ nylon-11 on thin film sulfuric acid anodized aluminum at various temperatures. Results are compared with that from ambient adhesive bond strength testing reported in Table 3.1. Dashed lines indicate the glass transition and melting temperatures of the polymer.

3.1.3. Tensile Testing. Tensile test curves from testing of pure nylon-11 and Corvel™ nylon-11 are shown in Figure 3.5. Elastic properties of both materials are equivalent: elastic modulus E = 1.2 GPa; Poisson's ratio ν = 0.3; elastic limit S_{el} = 25

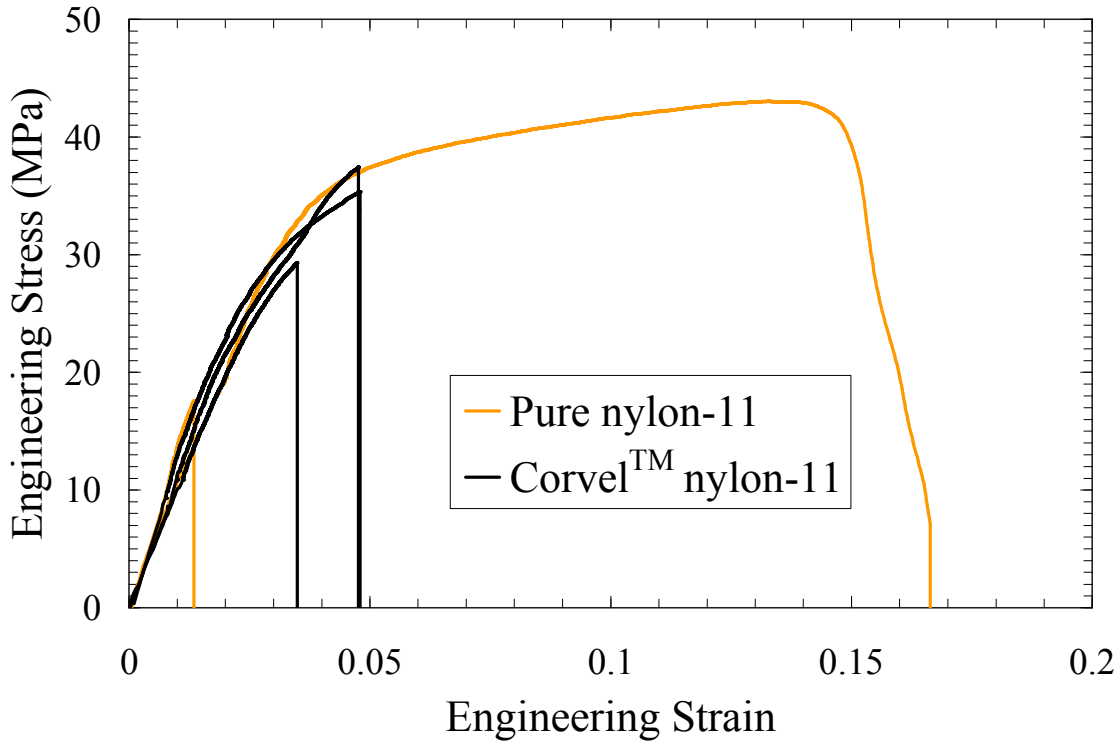

Figure 3.5. Tensile curves of sealant materials. Premature failure occurred as the result of severe porosity in the tensile bars.

MPa. The flexural modulus reported for nylon-11 in dry air and at 50 % relative humidity are 1.17 and 1.03 GPa respectively [79]. Failed specimens revealed severe porosity in the tensile bars due to polymer decomposition during the casting of the tensile bars. The elongation to fracture was varied significantly for both materials and sensitive to the size of the largest void, in some cases more than half the size of the cross-section of the tensile bar. Therefore, no conclusions regarding elongation to fracture or ultimate stress can be made.

3.1.4. Stress Relaxation Testing. Stress relaxation curves for pure nylon-11 and Corvel™ nylon-11 are shown in Figure 3.6. The natural logarithm of the ratio of

instantaneous modulus $E(t)$ with initial modulus E_o is plotted against the natural logarithm of time at full, constant strain e,

$$E(t) = \frac{\sigma(t)}{e} \tag{19}$$

where $\sigma(t)$ is the applied stress at time t. Both materials exhibit similar viscoelastic stress relaxation behavior typical of crystalline polymers. The slope of log [$E(t)/Eo$] vs. t begins to change at a load time of about 1 s and stabilizes at load times of ~300 s for the Corvel™ nylon-11 and ~2000 s for the pure nylon-11. The accelerated relaxation of the Corvel™ nylon-11 may be related to a reduced average chain length consistent with differential scanning calorimetry results indicating lower melting point.

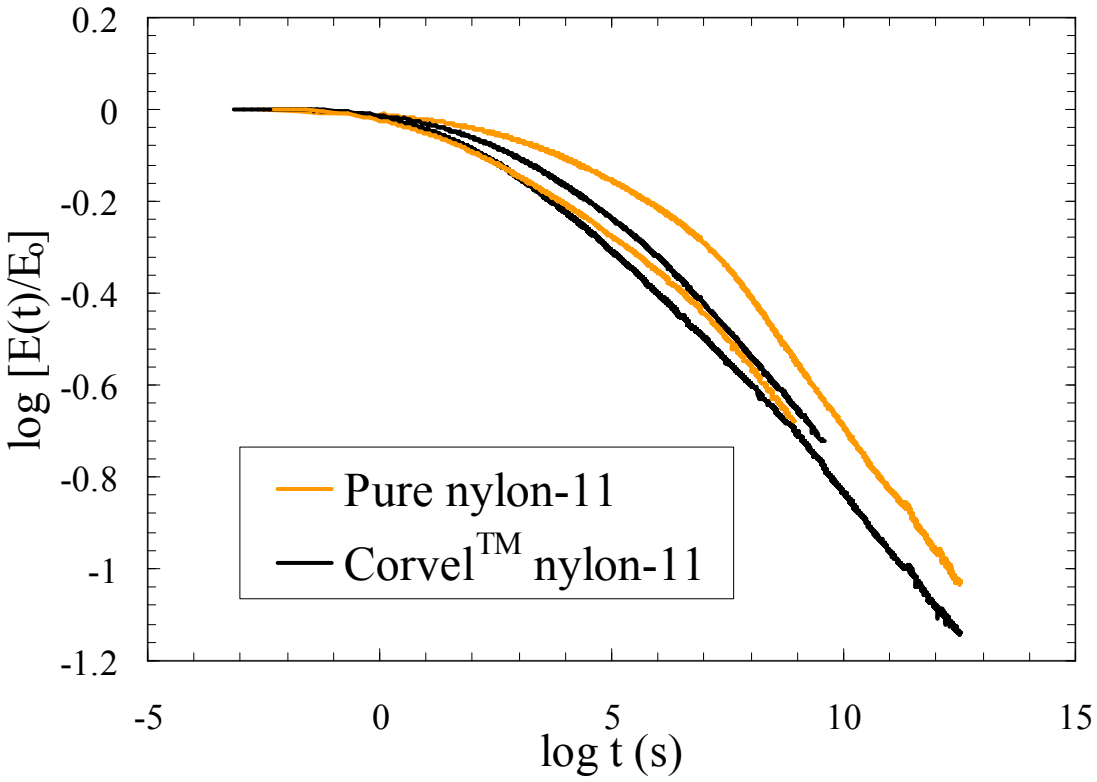

Figure 3.6. Stress relaxation curves of sealant materials.

3.1.5. Surface Energy Estimation and Wettability Prediction. Average sessile water drop contact angle θ_w measurements (± one standard deviation) on pure nylon-11, Corvel™ nylon-11, and thin film sulfuric acid anodized aluminum and calculated surface tensions γ_α of each material at 25 and 225 ºC are listed in Table 3.2. Surface tension obtained for pure nylon-11 is similar to that reported by Hybart and White using a maximum bubble pressure method at 225 ºC: 22.6 mJ/m^2 [112]. The predicted interfacial surface tension $\gamma_{\alpha\beta}$ of pure nylon-11 and Corvel™ nylon-11 on thin film sulfuric acid anodized aluminum at 25 and 225 ºC are listed in Table 3.3. Also listed is the predicted cos θ_w at 225 ºC from eq. 9 in section 2.3.5. The effect of raising the surface tension by adding high energy ceramic particles to a low energy polymer (as in Corvel™ nylon-11) is predictable and is reflected in the calculated surface tensions.

Table 3.2. Measured Water Contact Angle and Calculated Surface Energies

Material	θ_w (º)	$\gamma_{\alpha\beta}$ (mJ/m^2) with water at 25 ºC	γ_α (mJ/m^2)	
			25 ºC	225 ºC
Anodized Aluminum	53.3 ± 2.1	25.4	69.0	69.0
Pure nylon-11	72.0 ± 1.3	13.2	35.7	22.7
Corvel™ nylon-11	59.9 ± 1.8	10.5	47.0	34.0

Table 3.3. Predicted Interfacial Surface Energy and Wettability on Anodized Aluminum

Material	$\gamma_{\alpha\beta}$ (mJ/m^2) with anodized aluminum		cos θ_w (225 ºC)
	25 ºC	225 ºC	
Pure nylon-11	8.4	14.9	2.38
Corvel™ nylon-11	5.5	9.0	1.77

Calculations predict perfect wetting for both polymer samples on the anodized aluminum. However, better wetting (higher cos θ_w) is predicted for pure nylon-11 than for Corvel^{TM} nylon-11. Perfect wetting is not observed in practice, probably because of the limitations of achieving equilibrium conditions in short times with a highly viscous liquid and the difficulty of a viscous liquid in wetting a rough surface. Long time frame experiments above the melting temperature would result in significant polymer decomposition. Dynamic wetting considerations need to account for liquid viscosity (see eq. 6 in section 1.5). The ceramic particles added in Corvel^{TM} nylon-11 probably increase the viscosity per eq. 8 in section 1.5, thus further reducing the dynamic wetting on an anodized surface. However, the effect of reduced dynamic wetting is likely negligible because the adhesive bond strength of pure nylon-11 and Corvel^{TM} nylon-11 on anodized aluminum are equivalent.

3.2. MICROSTRUCTURES AND PROPERTIES OF LAP JOINTS

3.2.1. Microstructures of Lap Joints. Microstructures of the welds with prior thin film sulfuric acid anodization are shown in Figures 3.7 (without sealant), 3.8 (with DAPCO^{TM} rubber sealant) and 3.9 (with Corvel^{TM} nylon-11 sealant). Images are oriented such that the top-skin is above the T-rail. The faying surfaces are in contact adjacent to the weld. In sealed welds, the sealant was displaced away from the weld nugget during welding. No evidence of sealant incorporation into the weld was observed for any of the sealed welds. Sample microstructures of baseline welds to which preliminary fatigue testing results are compared are shown in Figure 1.9. Dimensions of weld features are listed in Table 3.4. Included are the anodized layer thickness, size of the faying surface

gap, weld width (distance between faying surface notches), and advancing side hook defect intrusion depth and angle. Grain diameter in the weld nugget for welds with nylon sealant ranged from 4 - 12 μm; that of all other welds ranged from 2 – 5 μm in diameter.

Table 3.4. Dimensions of Weld Cross-Sections

Prior Anodization	Sealant	Anodized Layer Thickness (μm)	Faying Surface Gap Size (μm)	Weld width (mm)	Hook Defect Size	
					Intrusion Depth (μm)	Intrusion Angle (º)
Bare	None	< 2*	-	-	-	-
Bare	Nylon	< 2*	-	-	-	-
Standard	None	14 ± 2	120 ± 20	3.6	100	30
Standard	Nylon	14 ± 5	140 ± 20	-	-	-
Thin Film	None	12 ± 4	90 ± 30	3.6	100	30
Thin Film	Nylon	8 ± 2	190 ± 40	4.2	200	45
Thin Film	Rubber	10 ± 4	220 ± 20	3.6	50	20

**thickness of oxide layer*

Welds with standard sulfuric acid anodization bear about 50 – 100 % thicker anodized layers than those with thin film sulfuric acid anodization. Even welds without sealant exhibited a faying surface gap that is probably the result of residual stress since parts were clamped during welding. The weld width is dependent on the welding parameters only. Welding was performed at 900 rpm and 4.2 mm/s (10 in/min) for welds without sealant or with rubber sealant and resulted in 3.6 mm (0.14 in) weld width. Welding at 1100 rpm and 3.6 mm/s (8.5 in/min) for nylon sealed welds resulted in 4.2 mm (0.17 in) weld width. The severity of the hook defect is also dependent on the welding parameters. The advancing side hook defect is deeper and intrudes at a steeper

angle for nylon sealed welds than other welds. Nylon sealed welds also have an upward hook defect at the retreating side notch (see Figure 3.9c) as opposed to the slight downward hook defect in welds without sealant (see Figure 3.7c). The rubber sealant appears to influence the hook defect as well. The rubber sealant reduces the severity of both the upward hook defect at the advancing side notch and the downward hook defect at the retreating side notch compared with welds without sealant (see Figures 3.7 - 3.8).

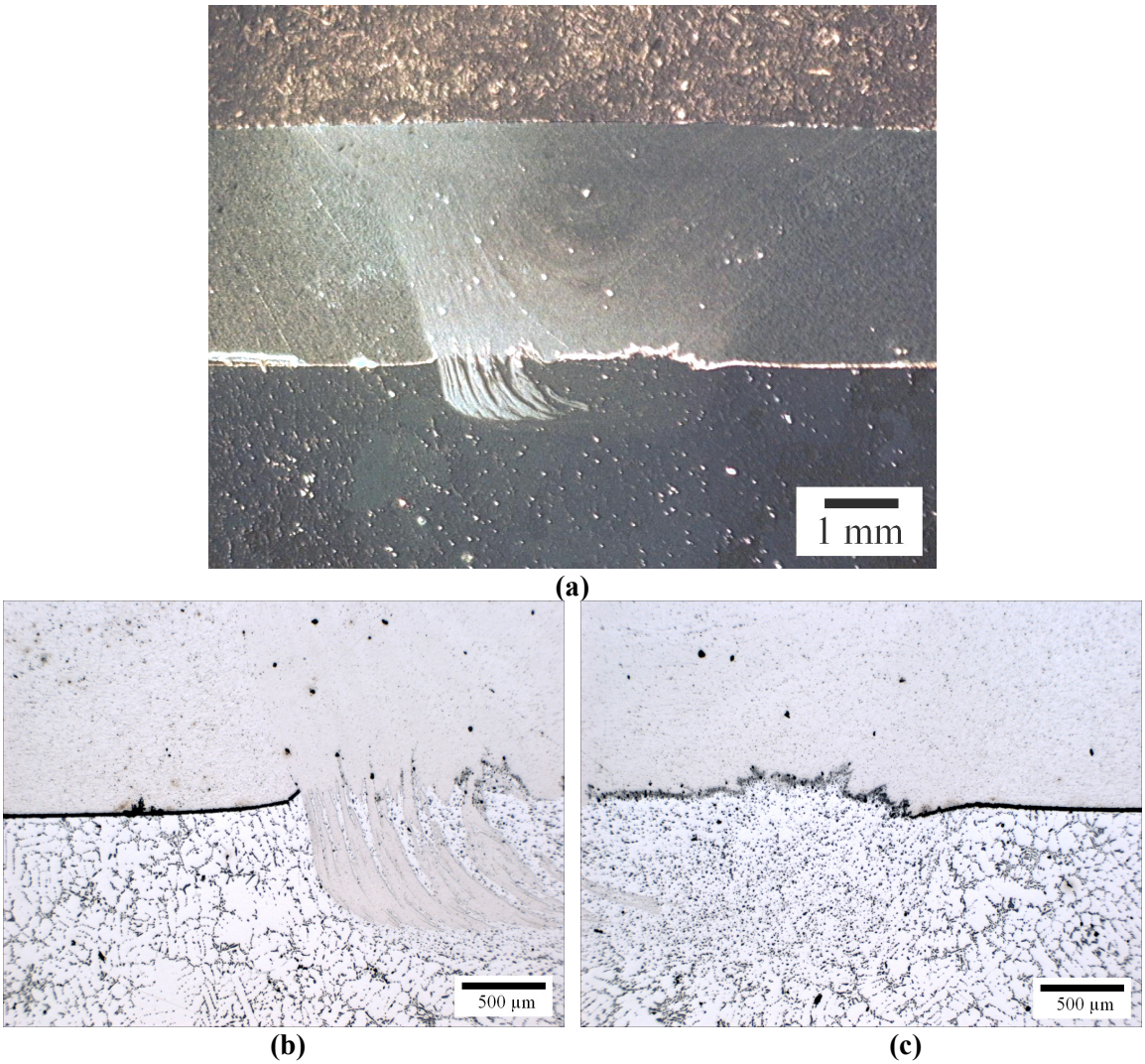

Figure 3.7. (a) Weld without sealant with prior thin film sulfuric acid anodization. (b) shows the advancing side notch and (c) shows the retreating side notch.

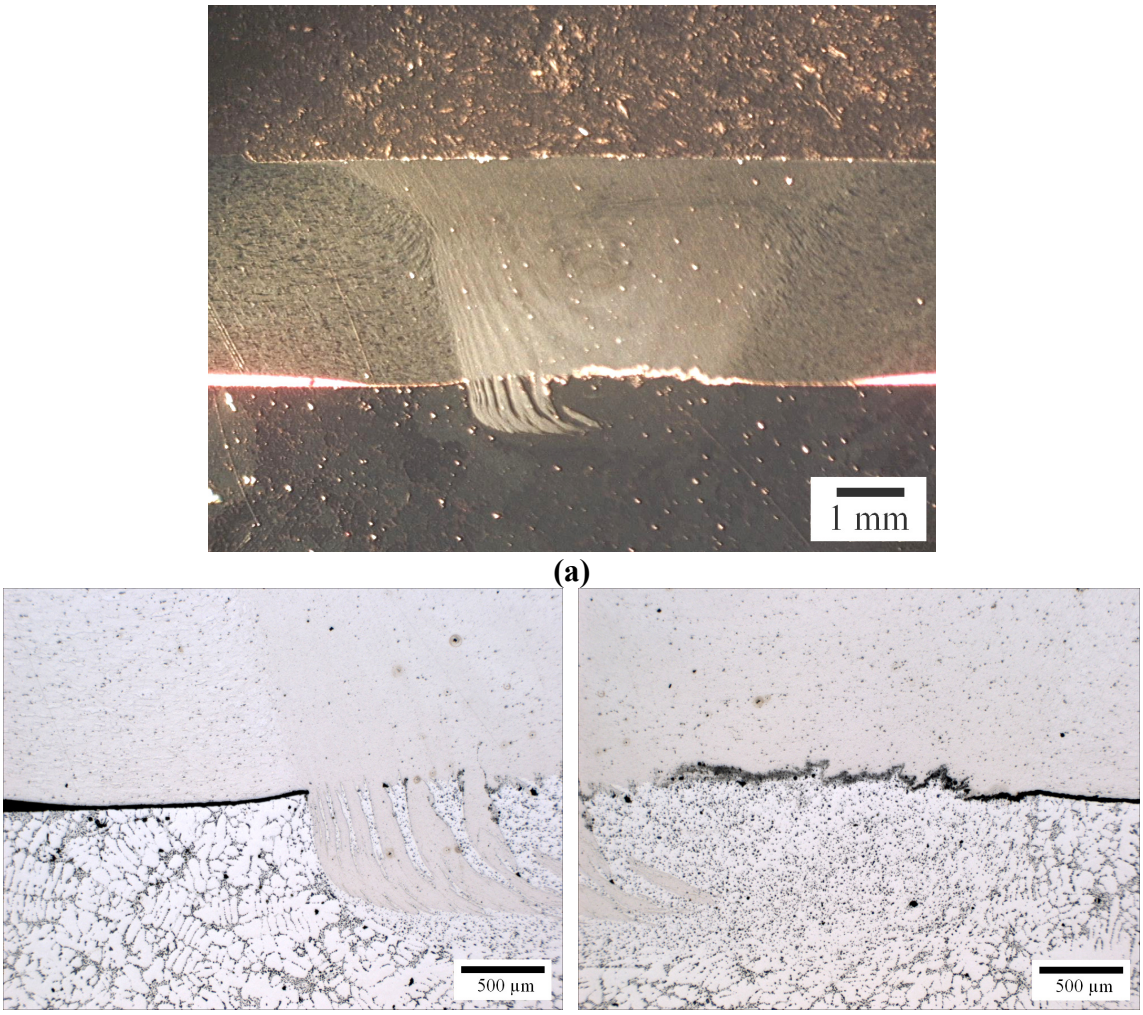

Figure 3.8. (a) Weld with DAPCO™ rubber sealant with prior thin film sulfuric acid anodization. (b) shows the advancing side notch and (c) shows the retreating side notch.

3.2.2. Tensile Testing of Lap Joints. Average maximum tensile loads measured during tensile testing are listed in Table 3.5. Error is reported as ± one sample standard deviation. Welds without sealant, welds with DAPCO™ rubber sealant, and Corvel™ nylon-11 sealed welds with no prior anodization were welded at 900 rpm and 4.2 mm/s

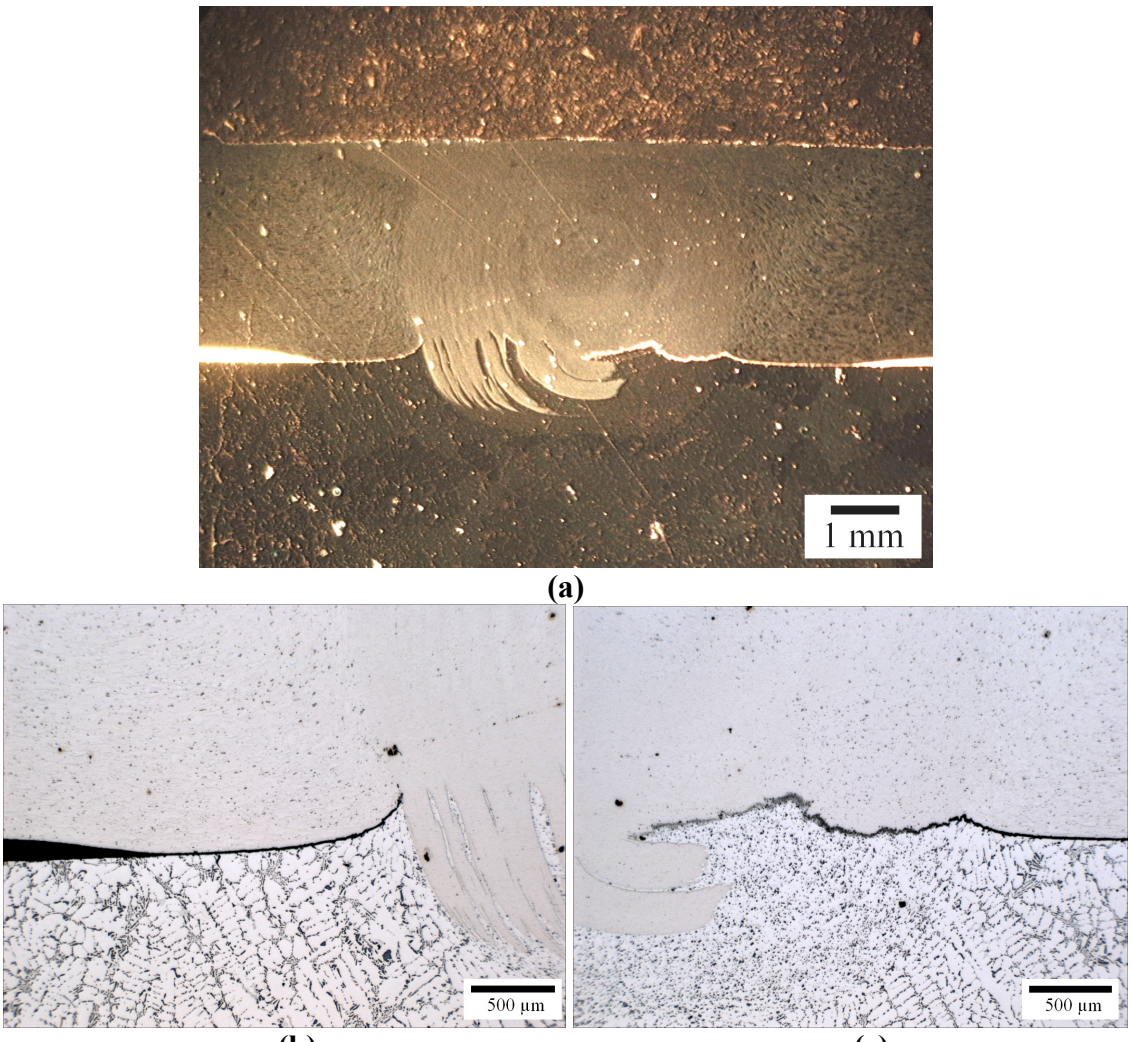

Figure 3.9. (a) Weld with Corvel™ nylon-11 sealant with prior thin film sulfuric acid anodization. (b) shows the advancing side notch and (c) shows the retreating side notch.

(10 in/min). Nylon sealed welds with prior anodization were welded at 1100 rpm and 3.6 mm/s (8.5 in/min). Sample tensile curves are shown in Figure 3.10 for welds with thin film sulfuric acid anodization.

Table 3.5. Tensile Weld Strength (N/mm of weld)

Prior Anodization	No Sealant	Corvel™ nylon-11	DAPCO™ rubber
Bare	*294 ± 5**	294 ± 14	-
Standard	*252 ± 7**	228 ± 14	266 ± 4
Thin Film	292 ± 7	273 ± 19	291 ± 19

**Reported by Van Aken et al.* [3]

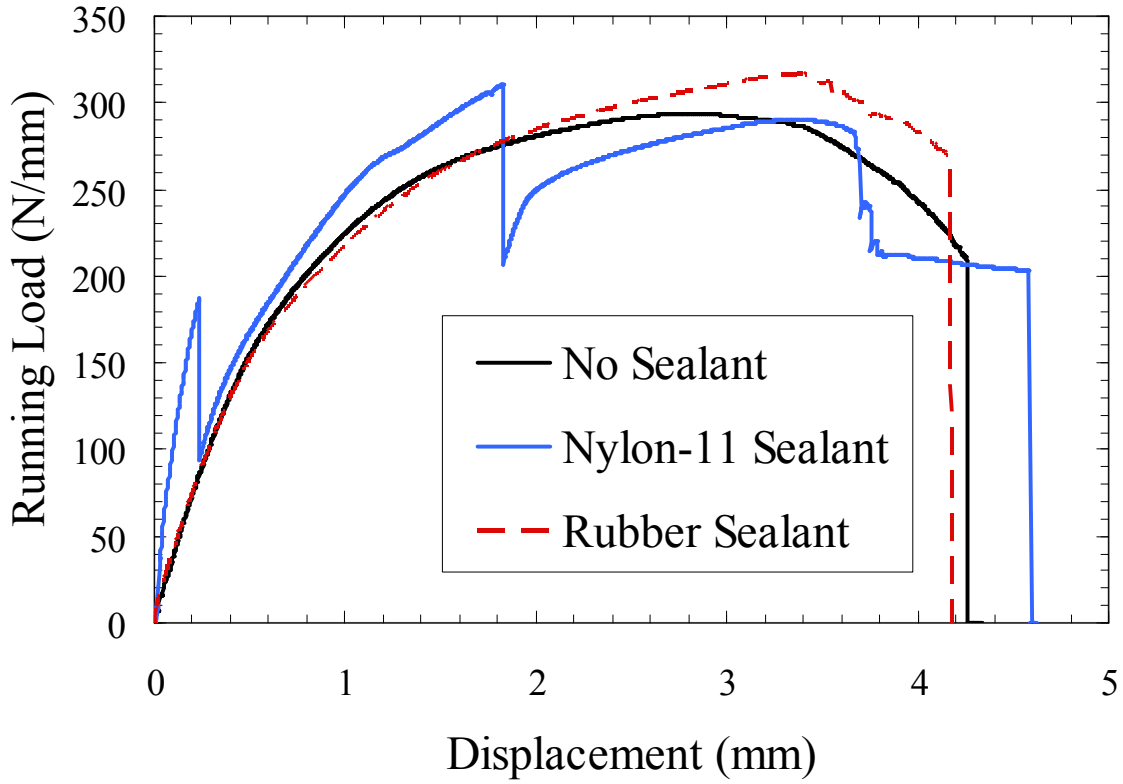

Figure 3.10. Representative sample tensile curves of welds with prior thin film sulfuric acid anodization. Nylon sealed welds were repaired.

The first two sudden load drops of the nylon sealed welds are associated with sealant bond failures on each side of the weld. Nylon sealed welds (thin film sulfuric acid anodized) were repaired by heat treating for 10 min at 200 ºC. The two specimens

tested without the repair did not exhibit good sealant bonding and the sealant failure occurred entirely at the interface between the sealant and the top-skin. These welds exhibited stiffness commensurate with welds where no sealant was applied. The sealant bonds were weaker and probably failed during specimen preparation. It was noted that the sealant could be manually peeled off the surface of the T-rail of the tested specimens.

For welds with nylon sealant repaired, the running loads at the failure of the first nylon sealant bond for each welding condition are listed in Table 3.6. The first nylon sealant bond to fail occurred at the sealed faying surface gap on the retreating side of the weld in 88 % of the specimens tested. The specimens were oriented such that half of the specimens were tested with the advancing side under one ear clamp and half were tested with the advancing side under the other ear clamp to examine effects of fixture misalignment. 58 % of the specimens failed with the advancing side under one ear clamp and 42 % failed with the advancing side under the other ear clamp. Thus, no correlation was observed with respect to the clamping fixture.

Sealant failure was mostly adhesive in nature (see Figure 3.11). In the welds with prior anodization, some delamination of the anodized layer was also observed. The extent of the delamination was more severe with standard sulfuric acid anodization than with thin film sulfuric acid anodization. This is likely attributed to the thicker anodization layer with standard anodization (see Table 3.4).

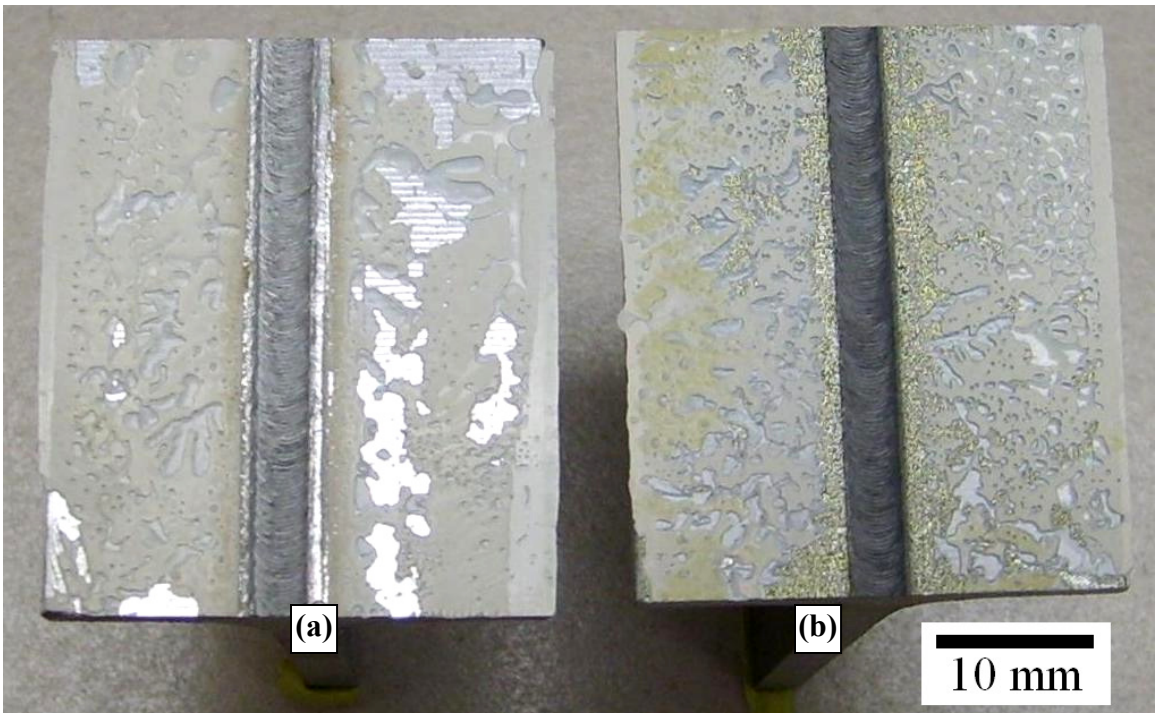

Figure 3.11. T-rail of failed sealed welds with (a) no prior anodization and with (b) prior standard sulfuric acid anodization. (b) shows evidence of anodized layer delamination from the top-skin.

Table 3.6. Load at First Nylon Sealant Failure

Prior Anodization	Bare	Standard	Thin Film (repaired)
Failure Load (N/mm of weld)	249 ± 33	97 ± 41	134 ± 63

3.2.3. Preliminary Fatigue Testing. Results of preliminary fatigue testing (78 N/mm of weld; steel fixture) with nylon sealed welds with standard sulfuric acid anodization are compared with results reported by Van Aken et al. in Figure 3.12 [3]. A two-parameter Weibull statistical analysis was used and is described as follows. Specimens were arranged in ascending order of number of cycles to failure N_i and

assigned a median rank i ranging from 1 – N where N is the sample size. Probability density P_f was determined for each specimen by

$$P_f(N_i) = \frac{i - 0.3}{N + 0.4} \tag{20}$$

P_f is related to N_i by the Weibull modulus m and scale parameter θ

$$P_f(N_i) = 1 - \exp\left(-\frac{N_i}{\theta}\right)^m \tag{21}$$

m and θ were obtained by linear regression analysis to fit the data to

$$\ln\ln\left(\frac{1}{1 - P_f(N_i)}\right) = m\ln(N_i) - m\ln\theta \tag{22}$$

The Weibull parameters were then used to calculate predicted fatigue life for 1, 10, 50, and 90 % sample population failure as listed in Table 3.7.

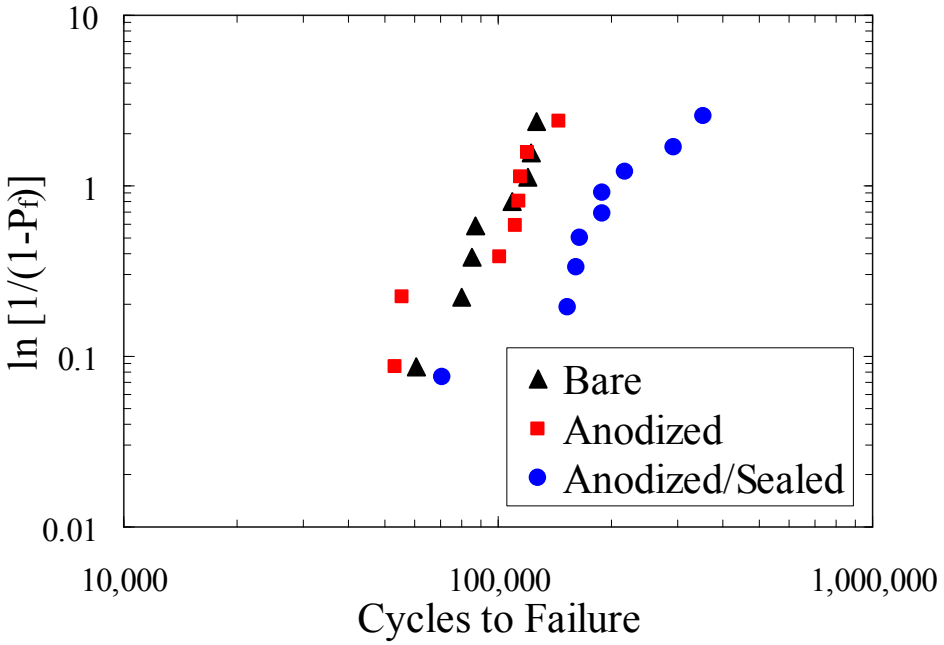

Figure 3.12. Weibull graph showing results of preliminary fatigue testing for welds with nylon sealant and prior standard anodization. Results are compared with welds without sealant reported by Van Aken et al. [3].

Table 3.7. Number of Cycles for % of Sample to Fail

% Failed	Bare	Anodized	Anodized with Nylon Sealant
1 %	36,400	22,100	32,100
10 %	64,100	52,000	88,400
50 %	101,000	103,000	199,000
90 %	134,000	160,000	334,000
	Weibull Parameters		
m	4.16	2.75	2.32
θ	110,000	118,000	233,000

Visual observation of fatigue crack propagation revealed that the fatigue cracking began at the hook defect on the advancing side of the weld for all specimens without sealant (see Figure 3.13). The cracks would then propagate into the top-skin through the weld. At about 80 % of the way through the top-skin, the cracks would slow down and eventually crack initiation at the retreating side notch would begin. This is verified by the rapid increase and subsequent leveling of the loop displacement data before increasing again (see Figure 3.14). For welds with prior anodization, the crack emanating from the retreating side always propagated horizontally through the weld along the oxide seam defect. For welds in the bare aluminum condition, the crack would either propagate through the top-skin, across the weld, or two cracks fronts would propagate, one along each path.

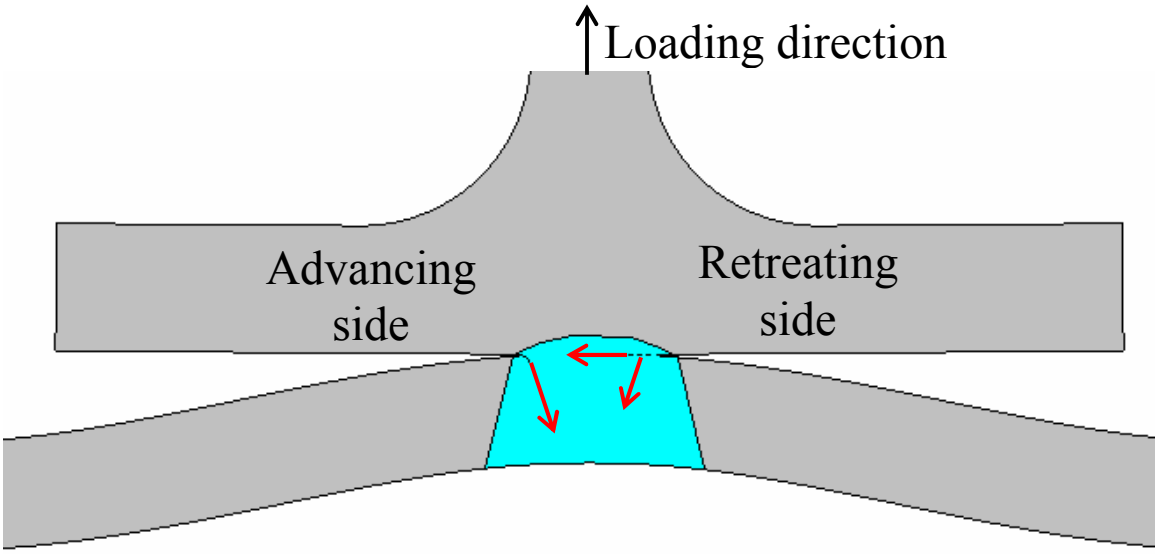

Figure 3.13. Schematic representing typical crack propagation. Cracking occurs at the advancing side notch first. In welds with prior anodization, cracks emanating from the retreating side usually follow the horizontal path.

It was noted that more than 50 % of the nylon sealed weld coupons tested had a failure of the sealant bond on either the retreating or advancing side within 1,000 fatigue cycles. The loop displacement prior to sealant failure is significantly less than in welds without sealant and loop displacement remains constant until the sudden failure of the sealant (see Figure 3.14). Therefore, the sealant bond seems to stiffen the lap joints and prevent fatigue cracking until the bond fails. No fatigue cracking prior to sealant bond failure was observed either visually or by observation of the loop displacement data. Sealant failure in ambient (lab air) fatigue tests is similar in appearance to that in tensile loading. Failure is characterized as predominantly adhesive between the anodized aluminum and nylon. The majority of adhesive failure occurred at the top-skin interface, as with tensile loading, and some anodized layer delamination was commonly observed.

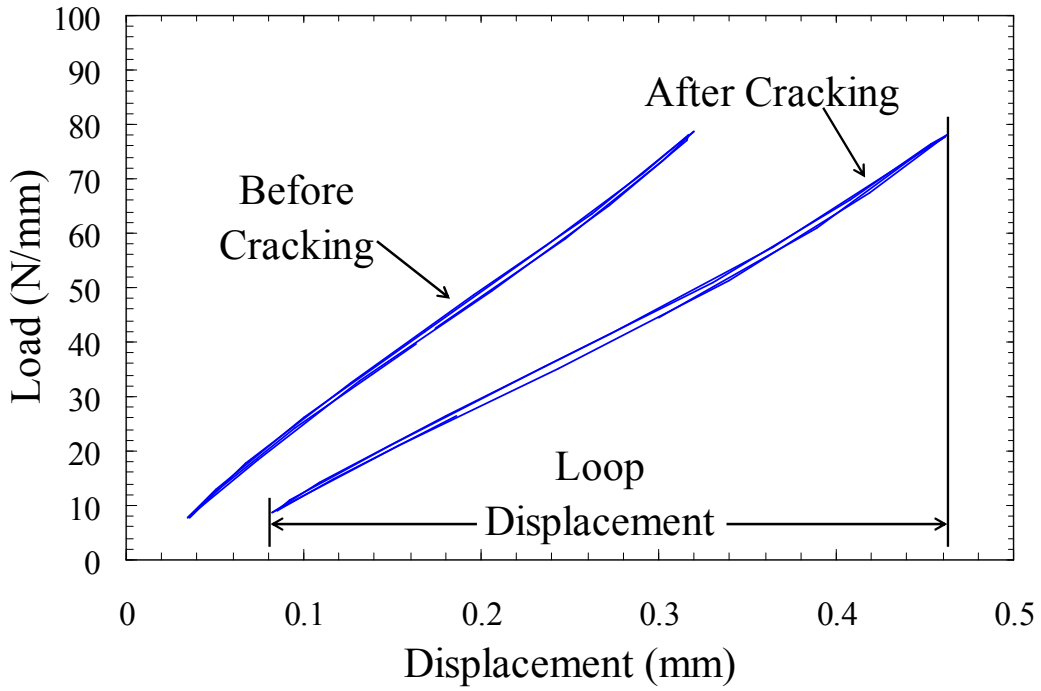

(a)

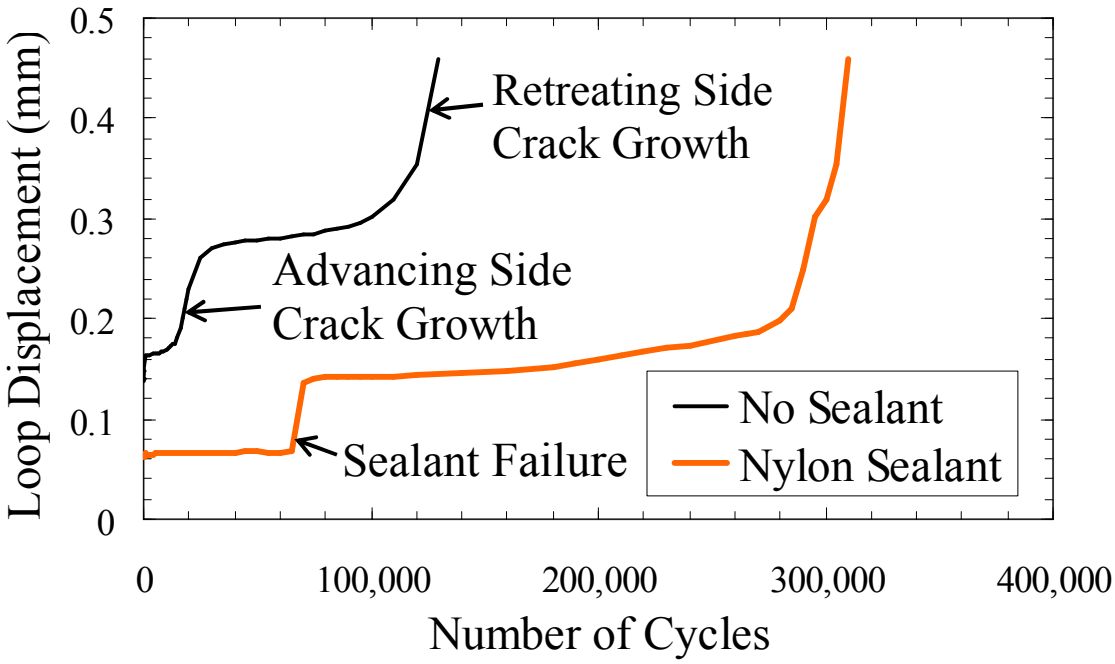

(b)

Figure 3.14. (a) Cyclic loop before and after fatigue cracking from which loop displacement is obtained. (b) Representative example loop displacement data for welds with prior standard sulfuric acid anodization with and without nylon sealant.

3.2.4. Fixture Comparison Study. Average fatigue lives for DAPCO™ rubber sealed weld specimens tested using either the steel or aluminum fixture, with either the rigid upper grip or the universal upper grip are listed in Table 3.8. Included are the average initiation life and propagation life determined by analyzing the loop displacement data (see Figure 3.15). Error is reported as ± one sample standard deviation. Preliminary testing was conducted with the steel fixture and rigid upper grip. Subsequent fatigue testing was conducted with the aluminum fixture and universal upper grip. Representative loop displacement curves for each fixture and grip condition are shown in Figure 3.16. All weld specimens initiated fatigue at the advancing side notch first and fatigue cracking progressed to about 80 % through the top-skin whereupon fatigue cracking at the retreating side notch advanced horizontally through the weld and failed the specimen. This was observed visually during testing and is consistent with observations in preliminary testing. Complete cracking through the top-skin from the advancing side notch was not observed in any of the specimens tested. Retreating side fatigue cracking occurred more simultaneously with advancing side fatigue cracking in welds tested with the rigid grip, regardless of the fixture. This implies more accelerated fatigue cracking and higher stresses at the retreating side notch with the rigid grip than with the universal grip. Independent of fatigue fixture, testing with the rigid grip exhibits a slight reduction in total fatigue life. Independent of upper grip, testing with the aluminum fixture exhibits a significantly reduced fatigue life and increased loop displacement.

Table 3.8. Fatigue Life Data for Various Fixture Conditions

Fixture	Upper Grip	Initiation Life	Propagation Life	Total Fatigue Life
Steel	**Rigid**	**26,300 ± 1,700**	**4,300 ± 2,000**	**30,500 ± 800**
Steel	Universal	30,800 ± 400	18,900 ± 4,700	49,600 ± 6,900
Aluminum	Rigid	14,100 ± 200	1,300 ± 100	15,400 ± 300
Aluminum	**Universal**	**15,100 ± 1,500**	**2,300 ± 700**	**17,400 ± 2,100**

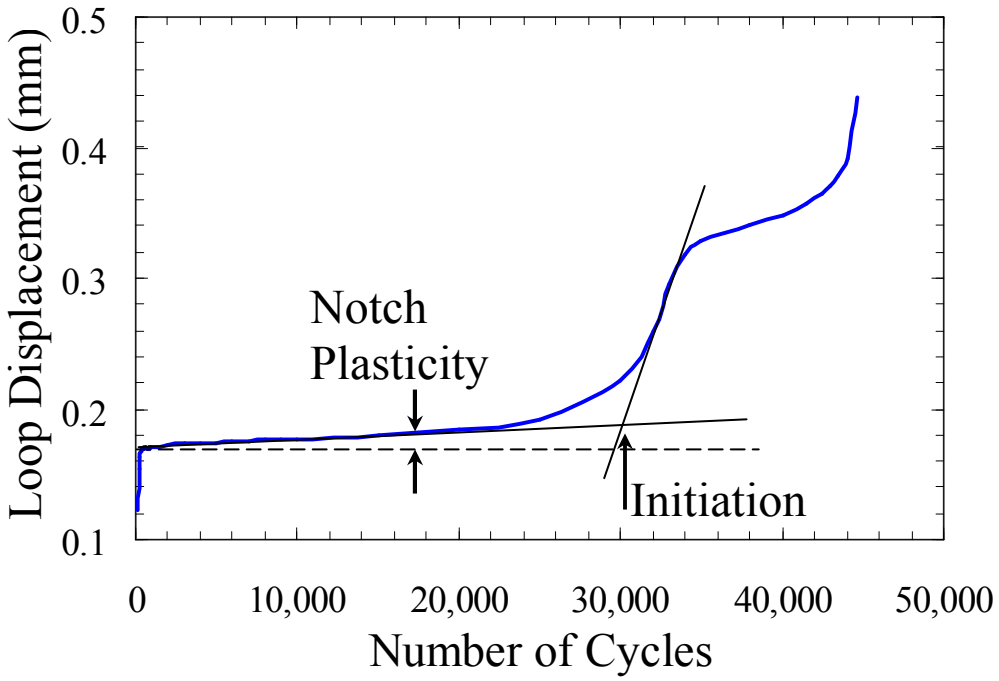

Figure 3.15. Example showing method for determining fatigue initiation life by using the tangent line at the inflection point of the first crack growth region.

3.2.5. Thin Film Sulfuric Acid Anodized Fatigue Testing. Figure 3.17 shows the ambient fatigue life analyzed using Weibull statistics of welds with Corvel™ nylon-11 sealant, DAPCO™ rubber sealant and without sealant using thin film sulfuric acid anodization of the aluminum pieces. The cyclic life for 1, 10, 50 and 90 % of the sample population to fail are listed in Table 3.9.

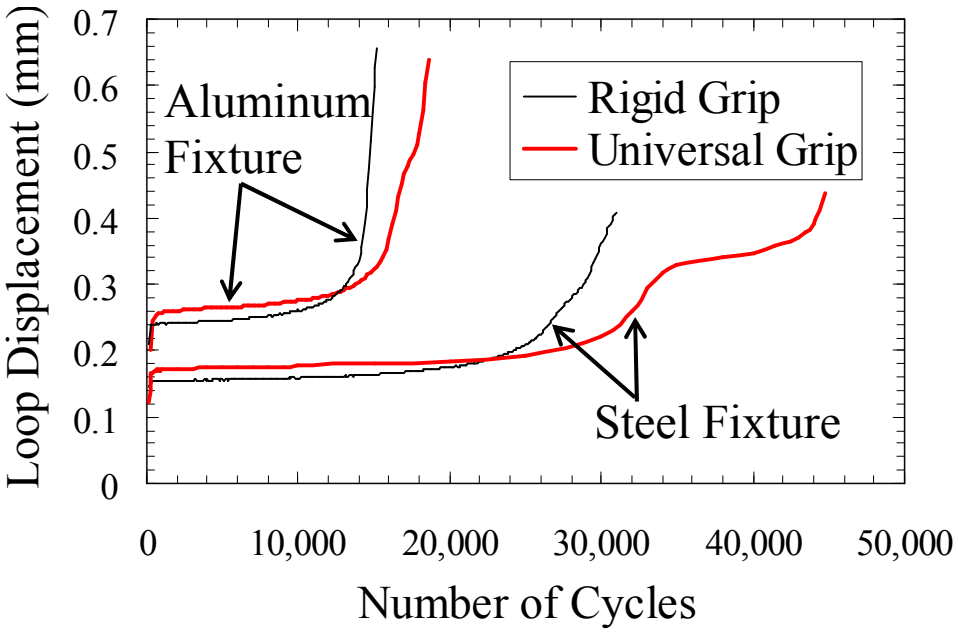

Figure 3.16. Representative loop displacement curves for rigid and universal grips with aluminum and steel fixtures at 78.8 N/mm maximum fatigue load.

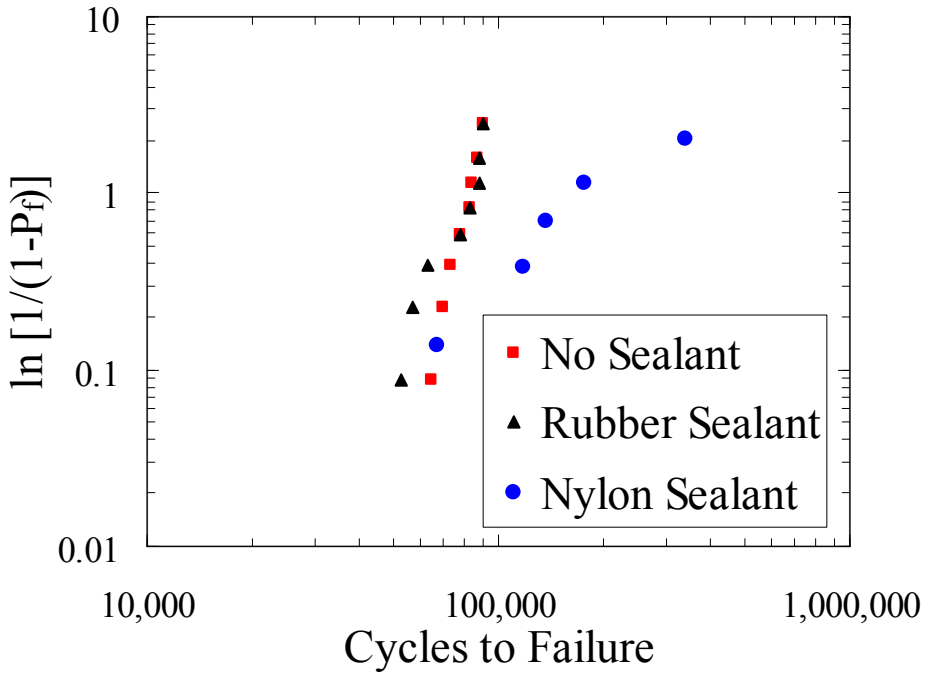

Figure 3.17. Weibull graph showing results of fatigue testing for welds with prior thin film sulfuric acid anodization without sealant and sealed with DAPCO^{TM} rubber or Corvel^{TM} nylon-11.

Fatigue crack initiation and propagation in thin film anodized welds without sealant or with rubber sealant were similar to those of welds with standard sulfuric acid anodization. However, for welds without sealant, the advancing side crack always fractured entirely through the top-skin prior to failure across the weld by the retreating side crack front. This was observed visually during the tests and resulted in a large sudden jump in the loop displacement and subsequent rapid crack growth at the retreating side crack front as shown in Figure 3.18. Cohesive failure of the rubber sealant was visually observed at the onset of fatigue loading. Representative loop displacement curves for weld coupons with each type of sealant are shown in Figure 3.19. Total fatigue life was comparable between welds without sealant and welds with rubber sealant. The initiation life was higher for welds with rubber sealant, occupying 73 - 88 % of the total fatigue life (41,400 – 79,300 cycles) while that for welds without sealant was only 36 - 46 % of the total fatigue life (29,900 – 41,000 cycles).

Table 3.9. Number of Cycles for % of Sample to Fail

% Failed	No Sealant	DAPCO™ Rubber Sealant	Corvel™ Nylon Sealant
1 %	50,500	31,500	13,000
10 %	65,000	51,300	51,700
50 %	79,500	75,900	156,500
90 %	90,500	97,400	317,100
		Weibull Parameters	
m	9.32	4.82	1.70
θ	82,700	81,900	194,200

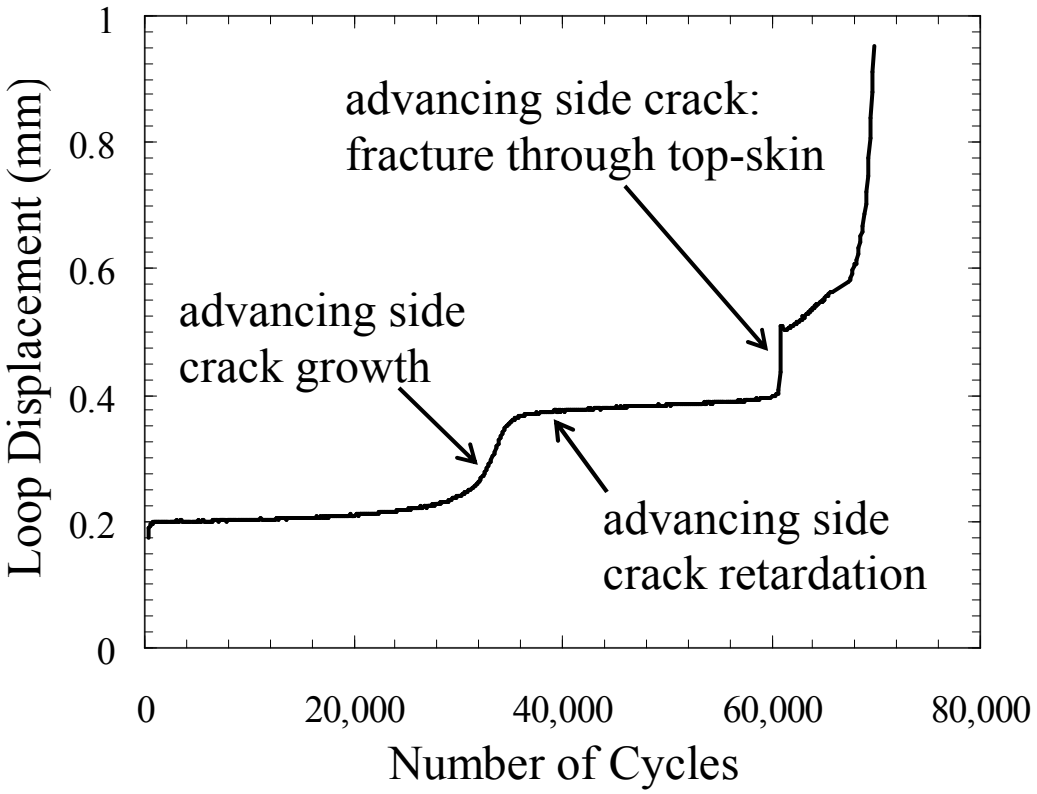

Figure 3.18. Loop displacement data of thin sulfuric acid anodized weld coupon without sealant showing advancing side crack growth, retardation, and final fracture through the top-skin.

Nylon sealed welds exhibited a significantly higher fatigue life than welds with rubber sealant or without sealant, similar to preliminary test results reported in section 3.2.3. Three of the eight specimens tested with nylon sealant did not fail within 1,000,000 cycles, the tests were terminated, and the specimens were not included in Weibull analysis. In nylon sealed weld coupons, no crack growth was observed until one of the sealant bonds failed. Failure of one of the sealant bonds occurred within 2,000 cycles for 37.5 % (three) of the weld coupons tested (see Table 3.10). These weld coupons occupied Weibull ranks i = 1, 2, and 3 and had statistically lower fatigue life than specimens with delayed sealant bond failure. Of these three weld coupons, the only

one in which the first sealant failure occurred on the advancing side occupied rank $i = 1$ and was the only weld coupon with fatigue life comparable to welds with other sealants.

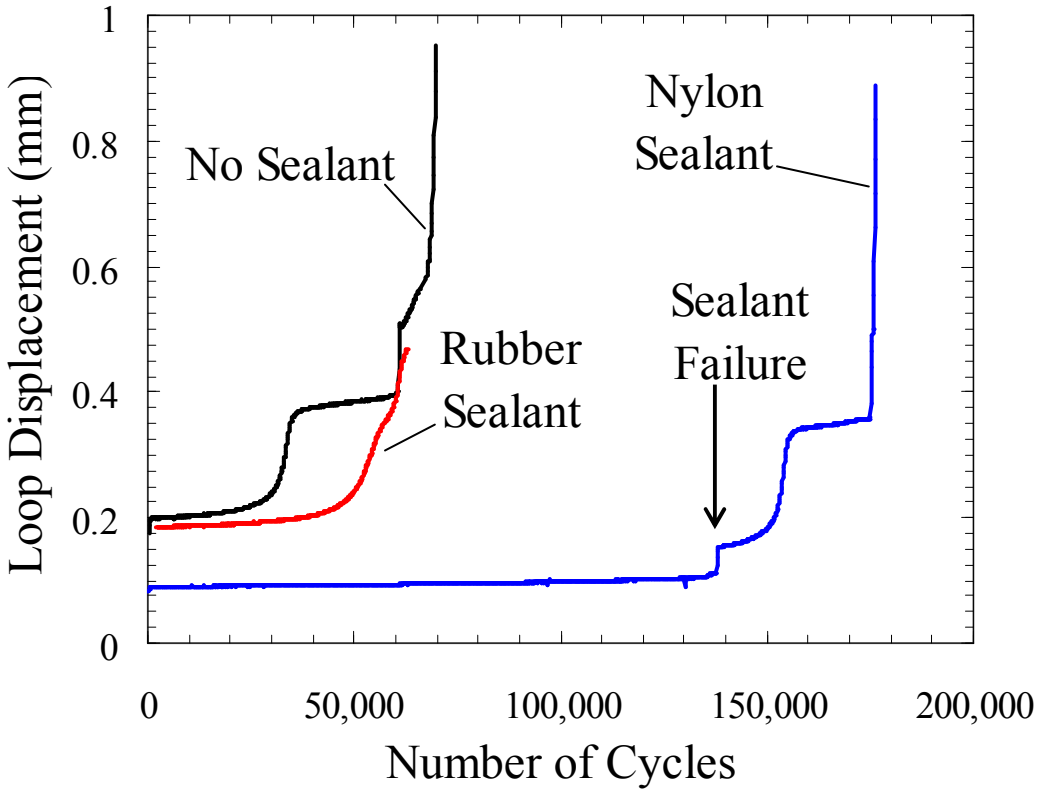

Figure 3.19. Loop displacement data of thin sulfuric acid anodized weld coupons without sealant, with rubber sealant, and with nylon sealant. In the nylon sealed weld coupon, first sealant bond failure occurred at 140,000 cycles.

The number of fatigue cycles to initiate fatigue after sealant bond failure is dependent on the location of the initial sealant bond failure (see Table 3.7). For welds with sealant failure occurring on the advancing side first, fatigue initiation occurred in about 15,000 additional cycles compared with 67,000 – 92,000 cycles for welds with

sealant failure occurring on the retreating side first. This is consistent with the tendency for fatigue cracking to initiate at the advancing side notch before the retreating side notch and suggests a greater susceptibility to fatigue cracking at the advancing side notch.

The fatigue fracture of the crack emanating from the advancing side notch of a specimen without sealant is shown in Figure 3.20. Two locations are shown corresponding with a crack length of 0.9 mm and 2.2 mm, 30 and 70 % of total crack length, respectively. Fatigue striations are observed at 2.2 mm crack length. Striation separation distance (*da/dN*) is about 200 nm. For 2024 at $R = 0.1$ in ambient conditions, *da/dN* = 200 nm/cycle occurs at K_{max} = 10.2 MPa√m (see Figure 1.7) [30]. At 0.9 mm, striations are too small to resolve with the scanning electron microscope and parameters used. Striations smaller than the microscope resolution (~20 nm) would occur at K_{max} < 7.2 MPa√m.

Table 3.10. Nylon Sealed Welds - Fatigue Initiation

Weibull Rank	First Sealant Bond Failure		Fatigue Initiation		
	Weld Side	No. of fatigue cycles	Weld Side	No. of total fatigue cycles	No. of cycles after sealant failure
1	Advancing	1,200	Advancing	17,000	15,800
2	Retreating	1,600	Retreating	68,500	66,900
3	Retreating	200	Retreating	84,000	83,800
4	Advancing	137,700	Advancing	152,000	14,300
5	Retreating	89,000	Retreating	181,000	92,000

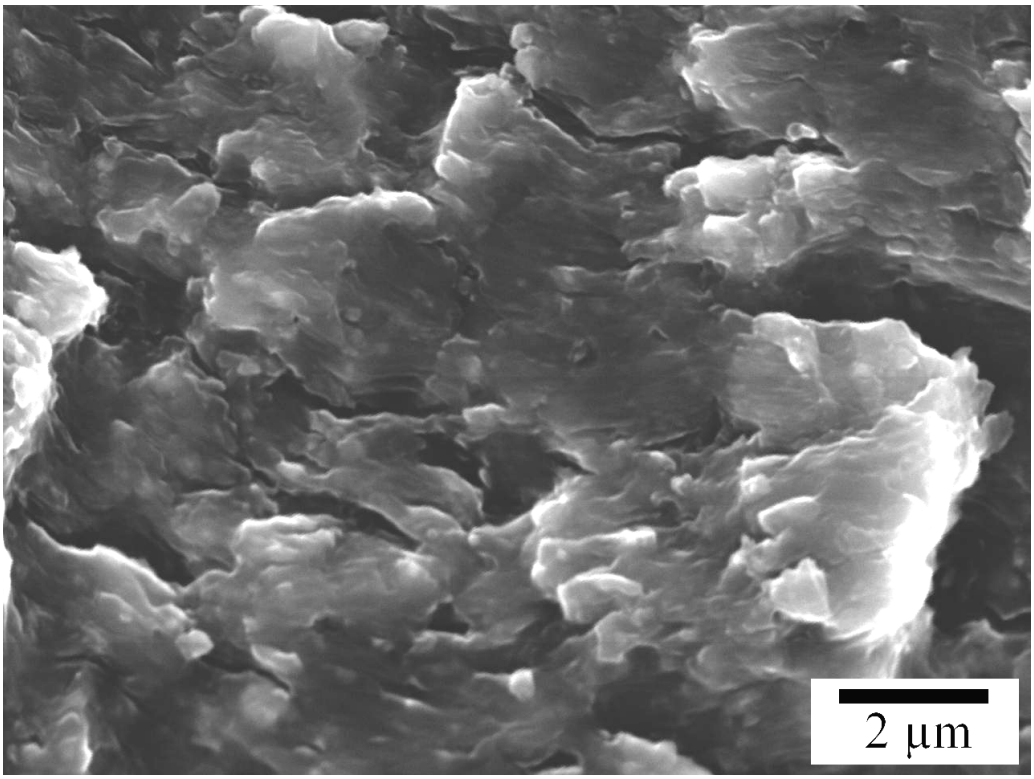

(a)

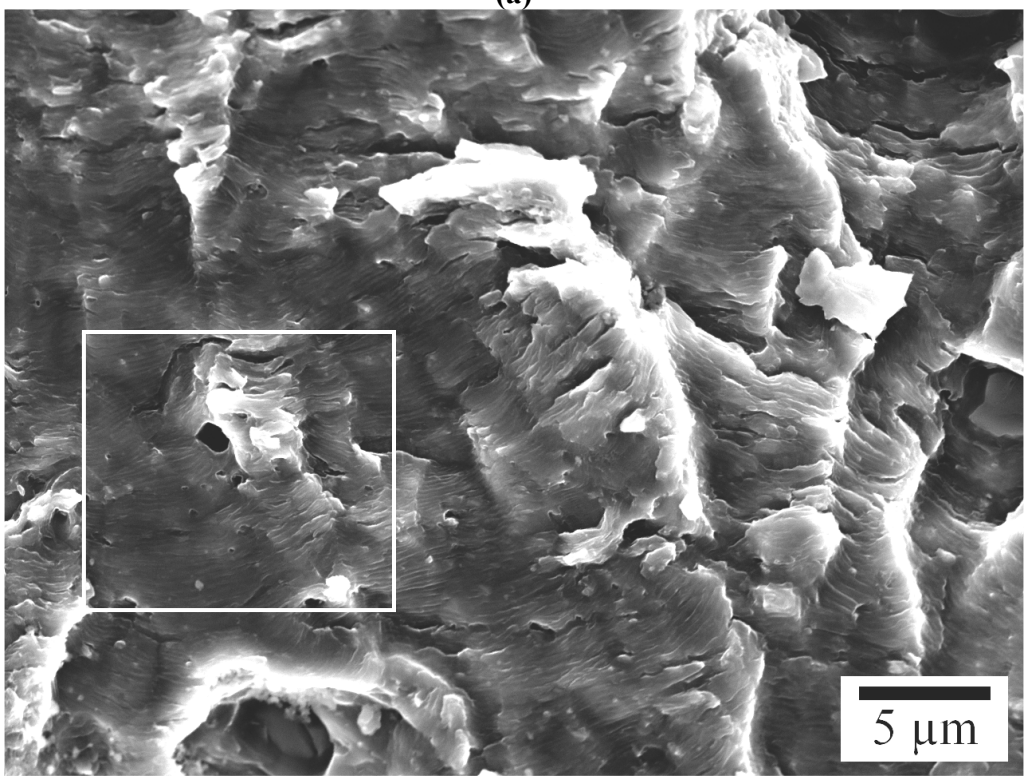

(b)

Figure 3.20. Ambient fatigue fracture surface of advancing side crack at (a) 0.9 mm and (b) 2.2 mm crack lengths. (c) boxed region in (b) at higher magnification showing fatigue striation separation of 200 nm.

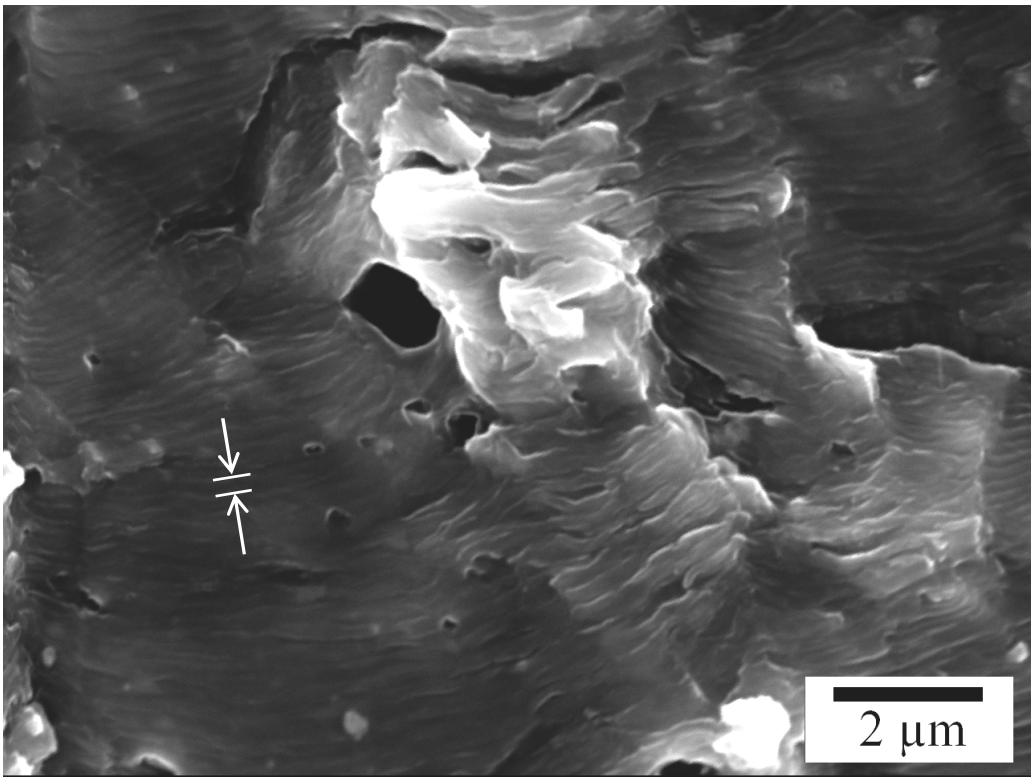

(c)

Figure 3.20. (cont.) Ambient fatigue fracture surface of advancing side crack at (a) 0.9 mm and (b) 2.2 mm crack lengths. (c) boxed region in (b) at higher magnification showing fatigue striation separation of 200 nm.

3.2.6. Corrosion Fatigue Testing. Testing results from fatigue loading in a neutral 3.5 % NaCl solution are shown in Figure 3.21. Unmasked specimens are indicated by arrows and no consistent effect due to masking is observed. The cyclic life for 1, 10, 50, and 90 % sample population failures predicted by Weibull statistics for each sealant condition are listed in Table 3.11.

DAPCO^{TM} rubber sealed welds exhibited a significant loss in fatigue life due to immersion in 3.5 % NaCl solution. However, corrosion fatigue life for rubber sealed welds is higher than for those without sealant. Nylon sealed welds exhibited the shortest corrosion fatigue life.

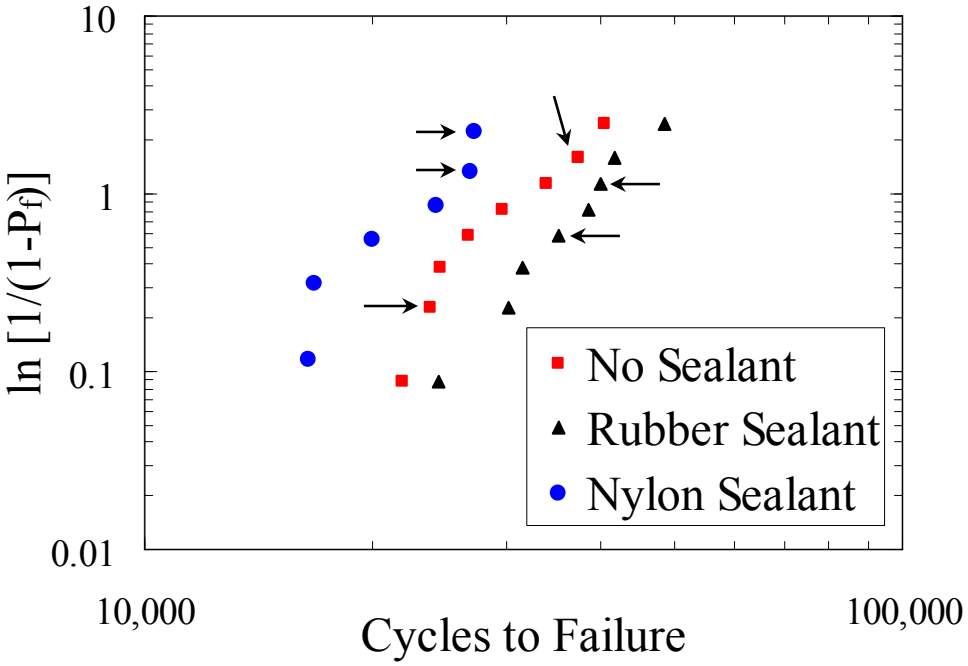

(a)

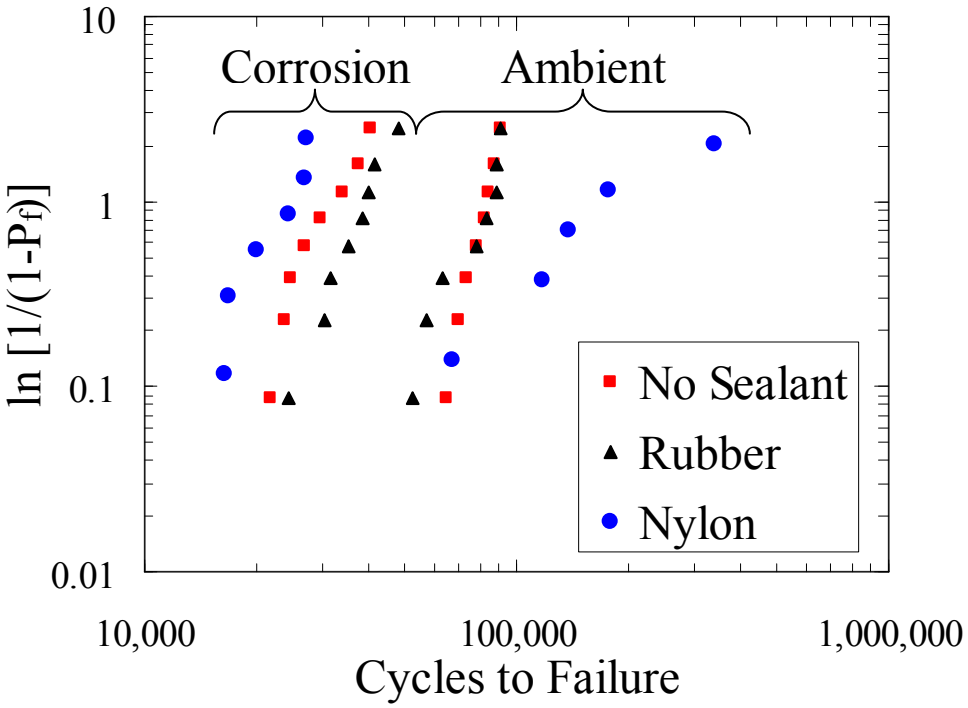

(b)

Figure 3.21. Weibull graphs showing (a) results of corrosion fatigue testing for welds with prior thin film sulfuric acid anodization without sealant and sealed with DAPCO^{TM} rubber or Corvel^{TM} nylon-11 (b) compared with results of ambient fatigue testing. Unmasked specimens are indicated by arrows in (a).

Table 3.11. Number of Cycles for % of Sample to Fail

% Failed	No Sealant	DAPCO™ Rubber Sealant	Corvel™ Nylon Sealant
1 %	12,100	15,800	8,500
10 %	20,100	25,200	14,400
50 %	30,100	36,600	22,200
90 %	39,000	46,400	29,200
		Weibull Parameters	
m	4.65	5.05	4.39
θ	32,600	39,400	24,100

For specimens with nylon sealant and with standard masking (see Figure 2.5a) or no masking, the first sealant failure occurred within 10 cycles of specimen immersion. The second sealant failure followed within 500 cycles. Total fatigue life for nylon sealed welds is significantly less than those without sealant or with rubber sealant. This may be related to the more severe hook defect of welds with nylon sealant (see Table 3.4).

Two specimens with nylon sealant were given additional masking to protect the sealant (see Figure 2.5b). The first sealant failure occurred at 1,200 cycles for one specimen and 15,900 cycles for the other. For the first specimen, water penetration through the mask was observed after the first sealant failure and total fatigue life was 34,800 cycles (comparable to nylon sealed welds with standard masking or no masking in corrosion fatigue). The solution may have penetrated the mask prior to sealant failure. For the specimen with delayed sealant failure, fatigue failure occurred at 133,700 cycles (comparable to nylon sealed welds in ambient air fatigue). Therefore, if the faying

surface notches are sealed and masked such that only anodized surfaces are exposed, corrosion fatigue is mitigated.

The corrosion fatigue fracture surface of a weld coupon without sealant is shown in Figure 3.22 at 0.9 mm and 2.2 mm crack lengths, similar to locations of ambient fatigue fracture surface images shown in Figure 3.20. At 2.2 mm, fatigue striations are separated by about 330 nm (compared with 200 nm for ambient fatigue striations at the same crack length, see section 3.2.5). Fatigue transitions across grains are more angular and abrupt than those in ambient fatigue.

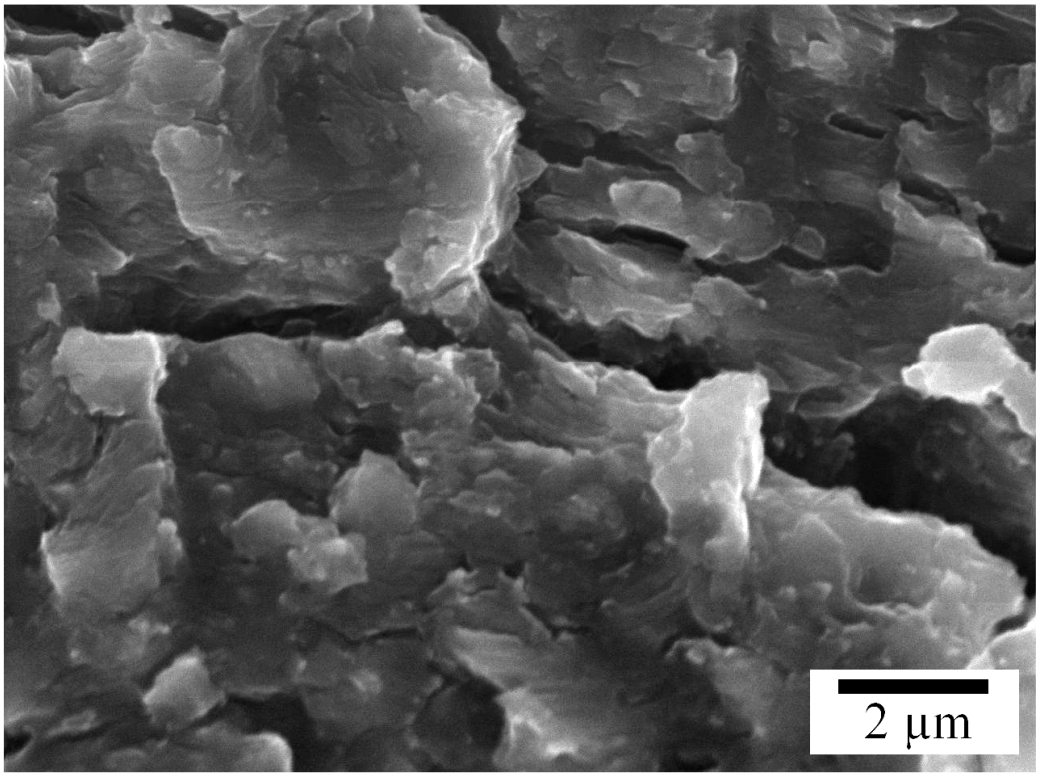

(a)

Figure 3.22. Corrosion fatigue fracture surface of advancing side crack at (a) 0.9 mm and (b) 2.2 mm crack lengths. Fatigue striation separation of 330 nm is shown in (b).

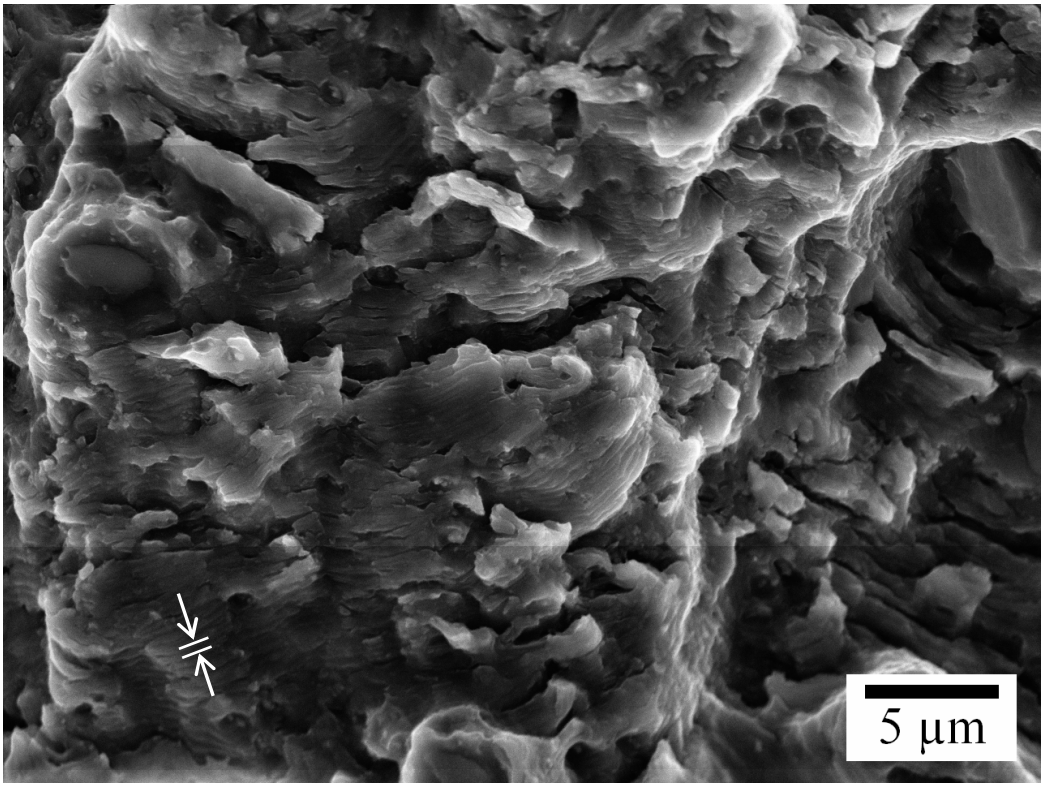

(b)

Figure 3.22. (cont.) Corrosion fatigue fracture surface of advancing side crack at (a) 0.9 mm and (b) 2.2 mm crack lengths. Fatigue striation separation of 330 nm is shown in (b).

3.3. FINITE ELEMENT MODELING RESULTS

3.3.1. Baseline Model. Finite element modeling crack tip results for the baseline, elastic, two-dimensional model are listed in Table 3.12. The baseline model is described in section 2.4.1 (see Figure 2.10). K_{II} is small and K_I is maximized because of the orientation of the axes with respect to the crack propagation direction θ_p. The faying surface gap opening at the furthest distance from the weld is 94 μm.

Table 3.12. Baseline Crack Tip Analysis Results

K_I (MPa*m^{½})	K_{II} (MPa*m^{½})	J (J/m^2)	θ_p (º)
4.330	**0.016**	**259.2**	**40**

The results of varying material parameters are listed in Table 3.13. The effect of varying elastic properties is negligible. Therefore, so long as the weld retains elastic properties similar to those of the materials being joined, the use of 2024 elastic properties will yield an accurate representation of the lap joint. There is no effect of introducing plasticity to the material on the square root of the predicted *J*-integral until a load of 30 N/mm (170 lbs/in) is reached (see Figure 3.23). Above 30 N/mm (J = 36 J/m^2), the plastic model predicts $\sqrt{J}$ between 4 and 7 % higher than that predicted by the elastic model. Because the $\sqrt{J}$ is directly related to K_I (see eq. 17 in section 2.4.2), models using only elastic properties can be expected to underestimate predicted K_I values by about 7 %.

Table 3.13. Material Parameter Effects on Crack Tip Analysis

Material	Material Type	K_I (MPa$\sqrt{}$m)	J (J/m^2)
2024	**Elastic**	**4.330**	**259.2**
2024-T6	Elastic - Plastic	-	298.1
357	Elastic	4.322	260.5

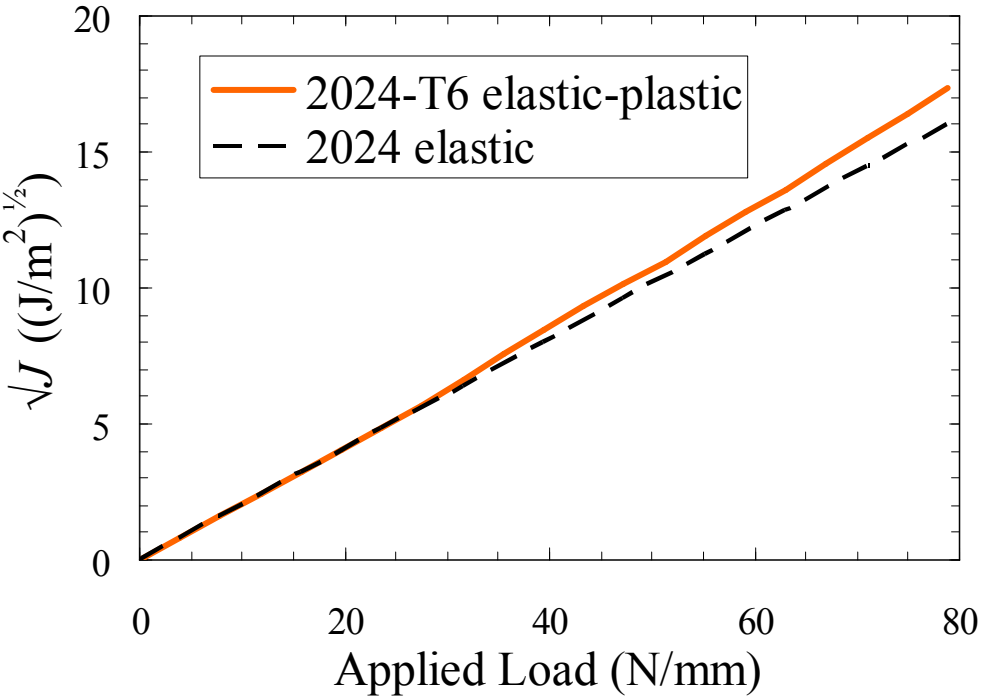

Figure 3.23. Square root of J at the crack tip versus applied load per length of weld comparing an elastic-plastic model and an elastic model.

3.3.2. Three Dimensional Model. Crack tip analysis results of three dimensional models of 25.4 mm and 38.1 mm weld coupons are shown in Figure 3.24. K_I levels off to about 4.8 MPa√m and K_{III} tapers to zero for both sizes of weld coupon at the center of the coupon. This suggests a plane strain condition at the center of the weld coupon. Maximum K_I is predicted at 2.5 mm from the center of the 25.4 mm weld coupon and 5.0 mm from the center of the 38.1 mm weld coupon. The maximum K_I for the 25.4 mm and 38.1 mm weld coupons are equivalent at 4.96 and 4.93 MPa√m, respectively. However, these values are significantly larger than K_I = 4.33 MPa√m predicted by the baseline two-dimensional model.

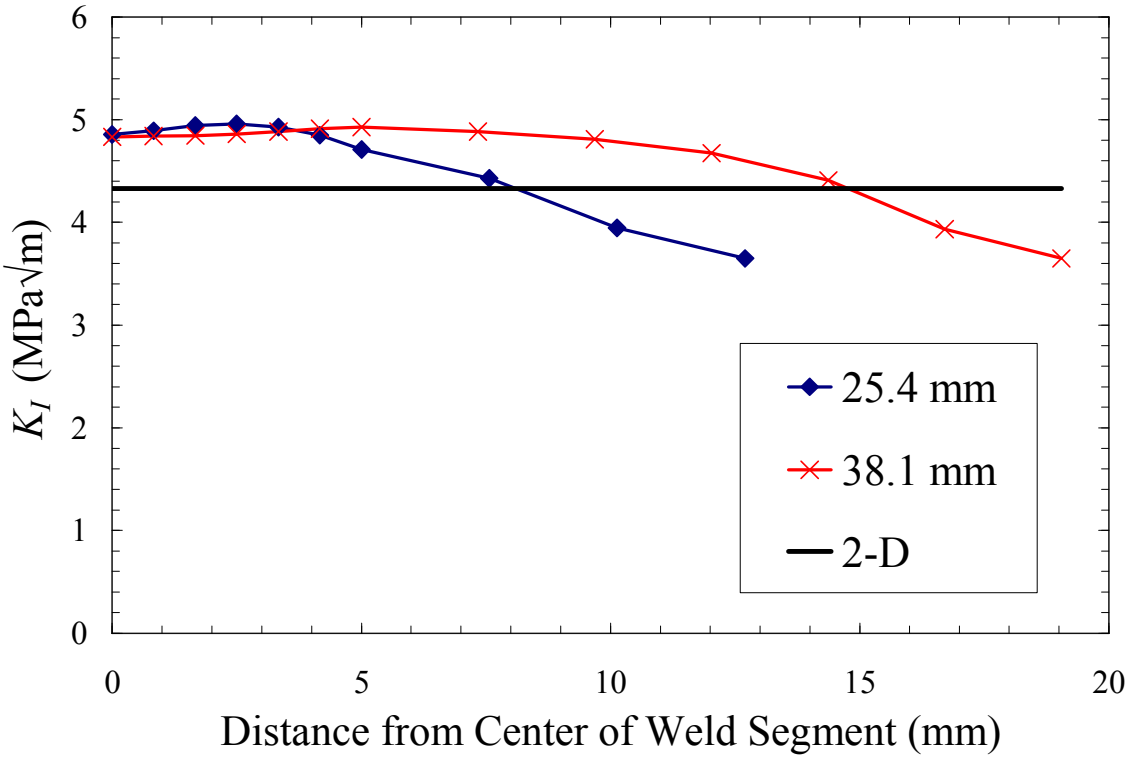

(a)

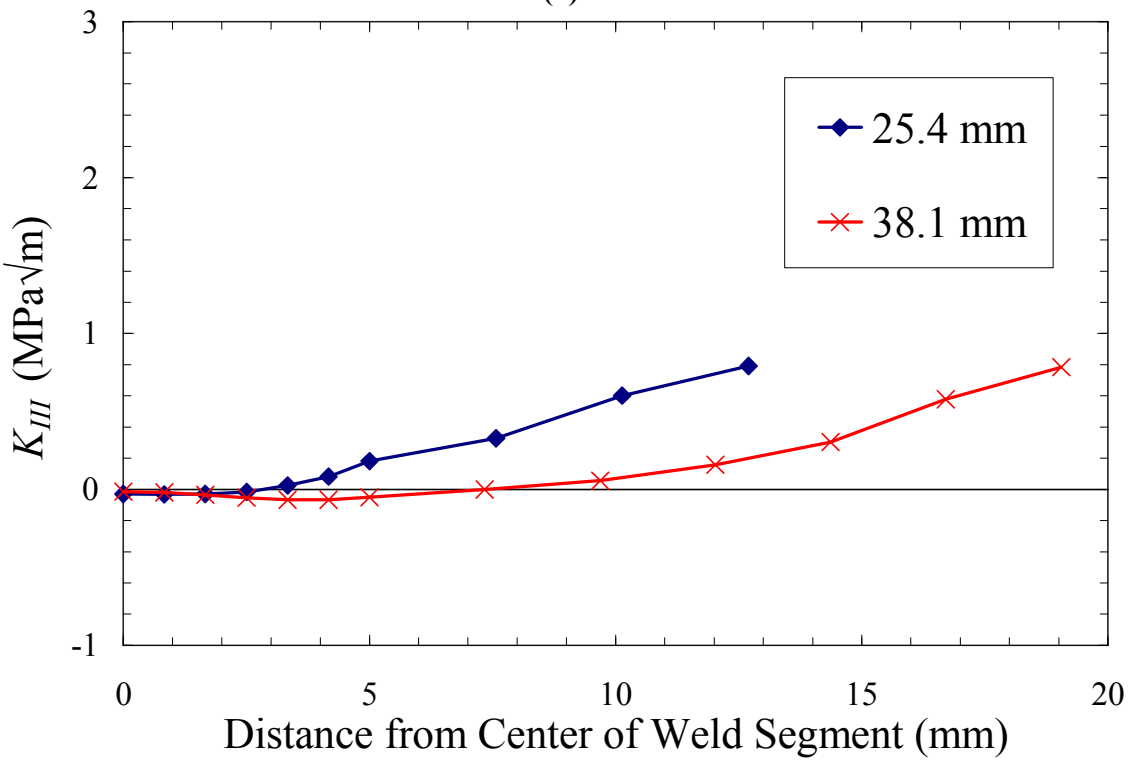

(b)

Figure 3.24. (a) mode I and (b) mode III stress intensity factors versus location along weld coupon.

3.3.3. Model Geometry Effects. Effects of varying the width of weld joint (measured as 2*x*) on the flat notch model (baseline) are shown in Figure 3.25. Maximum K_I occurs at a weld width of 6 mm, but the actual weld width typically observed is between 3.6 and 4.2 mm (see Table 3.4).

The effect of the hook angle (θ_h) in the partial hook notch model at constant hook intrusion depth y = 0.5 mm is shown in Figure 3.26a. K_I increases with θ_h below 75º. The crack propagation direction (θ_p) results are listed in Table 3.14 and show a trend of crack rotation towards 75º. The effect of varying hook intrusion depth for a partial hook model with θ_h = 30º and for a full hook model (θ_h = 90º) is shown in Figure 3.26b. Increasing hook intrusion depth also increases K_I and seems to continue to increase beyond an intrusion depth of 1.0 mm (roughly halfway through the top-skin). Hook radius (*r*) has no effect on crack tip stress intensity factors.

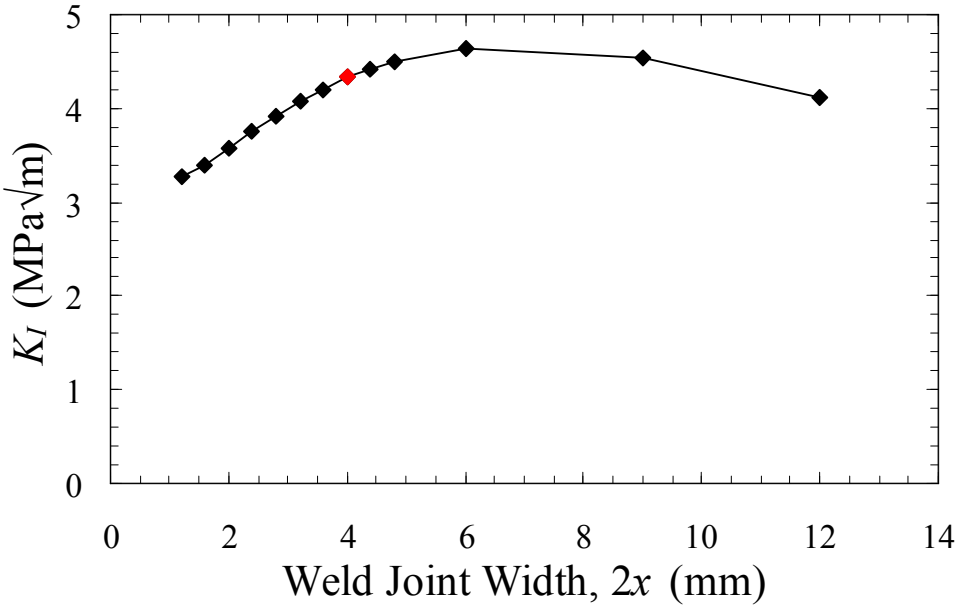

Figure 3.25. K_I at various weld joint sizes for flat faying surface model. Typical weld joint sizes of actual welds are 3.6 – 4.2 mm. Red point indicates result of baseline model.

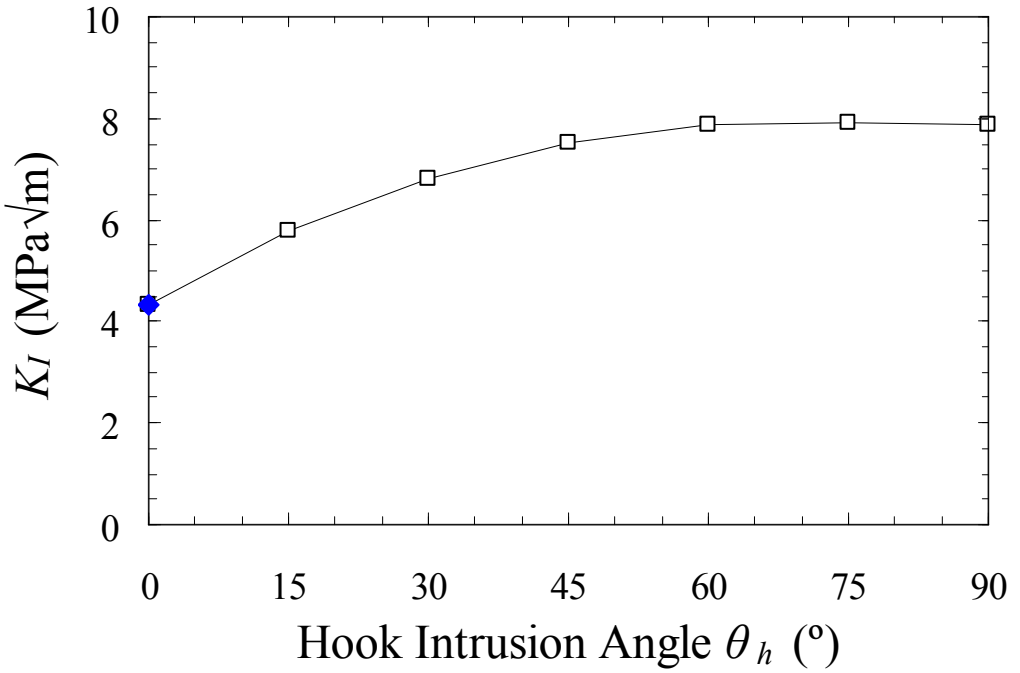

(a)

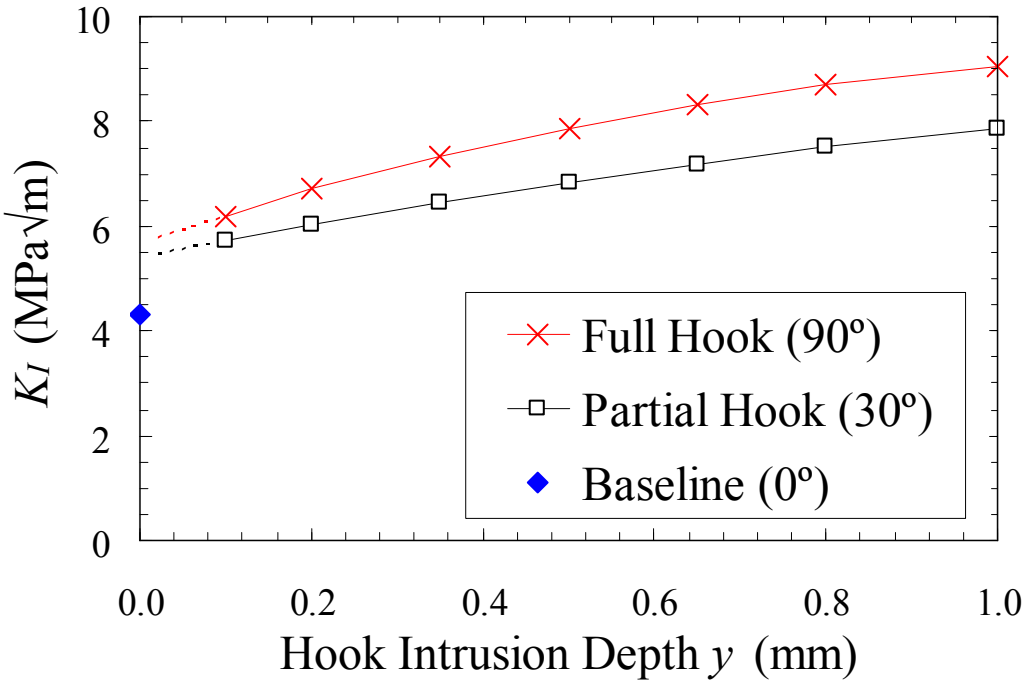

(b)

Figure 3.26. K_I for partial hook model at (a) various θ_h and constant y = 0.5 mm and (b) various y with constant θ_h = 30° (partial hook) and 90° (full hook). Baseline results are included for comparison.

Table 3.14. Partial Hook Model Results at Various Hook Angles

Hook Intrusion Angle, θ_h (º)	K_I (MPa√m)	Crack Propagation Direction, θ_p (º)
0	**4.330**	**40**
15	5.779	35
30	6.830	48
45	7.537	62
60	7.867	72
75	7.910	75
90	7.869	76

3.3.4. Sealant Effects. The effect of a sealant in the faying surface gaps was evaluated based on nylon-11 elastic properties obtained from tensile testing (section 3.1.3). Results were obtained with sealant layer thickness (t) varied between 0.1 and 0.2 mm, reflecting observations of actual lap joints. These results are compared with results from full hook models (θ_h = 90º) of y = 0.5 mm with and without sealant in Table 3.15. Also shown is the effect of a partially filled sealant gap with t = 0.1 mm and no hook defect. Regardless of sealant thickness and fill, K_I at the faying surface notch is reduced by about > 90 %.

The stress distribution at the location of maximum stress in the sealant for the completely filled sealant model is shown in Figure 3.27. For t = 0.1 and 0.2 mm, σ_{max} = 28.5 and 26.0 MPa, respectively. It should be noted that the majority of the sealant in the model is below S_{el} (25 MPa) determined from tensile testing (section 3.1.3). Therefore, an elastic model for the sealant is valid.

The stress distribution in the sealant for the partially filled sealant model is shown in Figure 3.28. The maximum stress in the sealant is 74.1 MPa and the stress throughout the bulk of the sealant is 20 – 50 MPa. Therefore, if the sealant only partially fills the faying surface gap, the sealant bond may fail at lower applied loads during testing of the welded lap joint.

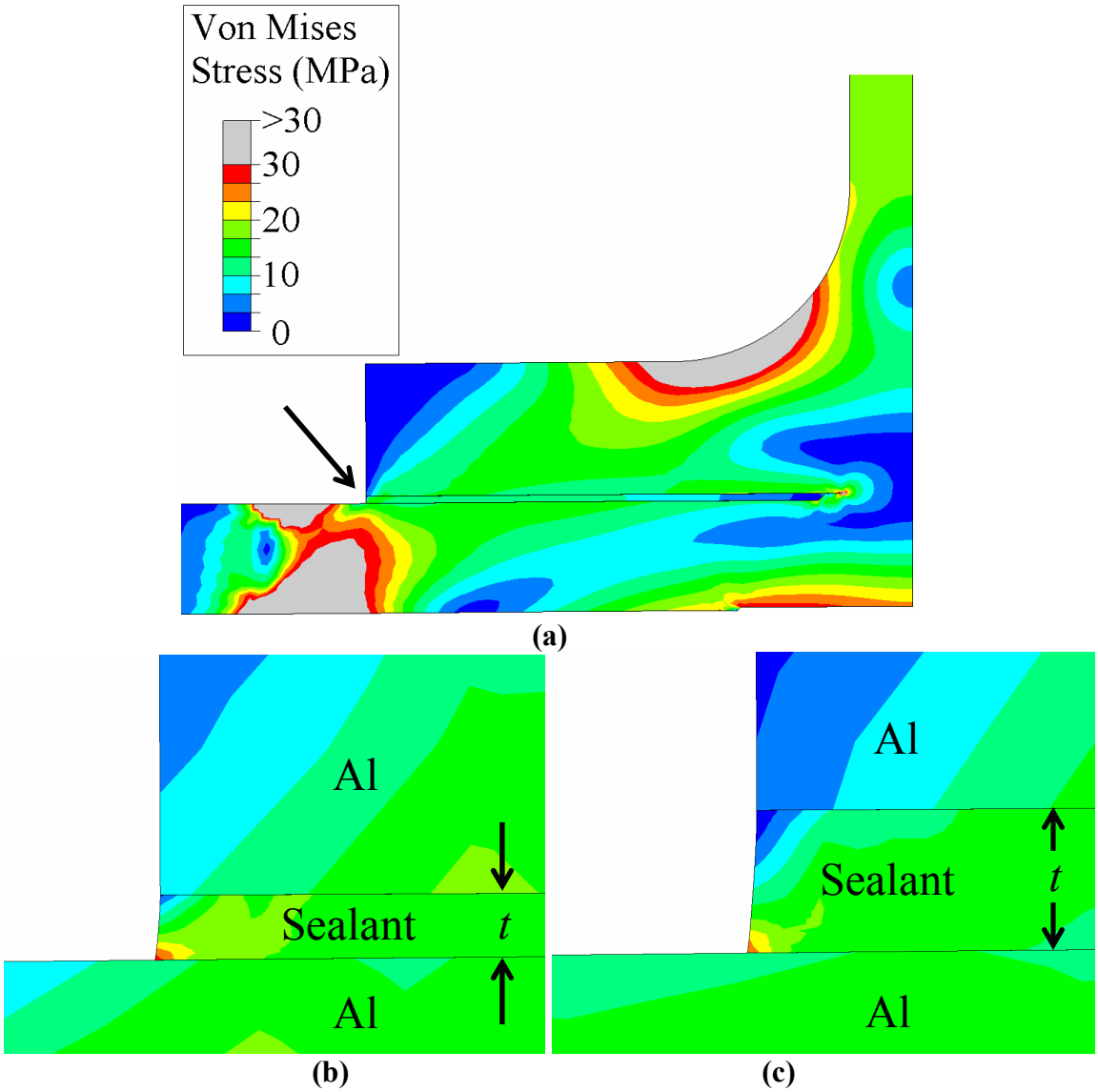

Figure 3.27. Von Mises stress distribution in (a) completely filled sealant model at the location of maximum stress in the sealant (indicated by arrow) for t = (b) 0.1 and (c) 0.2 mm.

Table 3.15. Crack Tip Analysis Results for Models with Sealant

Sealant Fill	y^* (mm)	t^* (mm)	K_I (MPa$\sqrt{m}$)	J (J/m^2)	θ_p (º)
None	**0**	**0**	**4.330**	**259.2**	**40**
Full	0	0.1	0.220	0.596	48
Full	0	0.2	0.343	1.440	48
Partial	0	0.1	0.171	0.359	60
None	0.5	0	7.869	855.2	76
Full	0.5	0.1	0.185	0.423	57
Full	0.5	0.2	0.388	1.856	63

*y *and* t *defined in Figures 2.15 and 2.16, respectively*

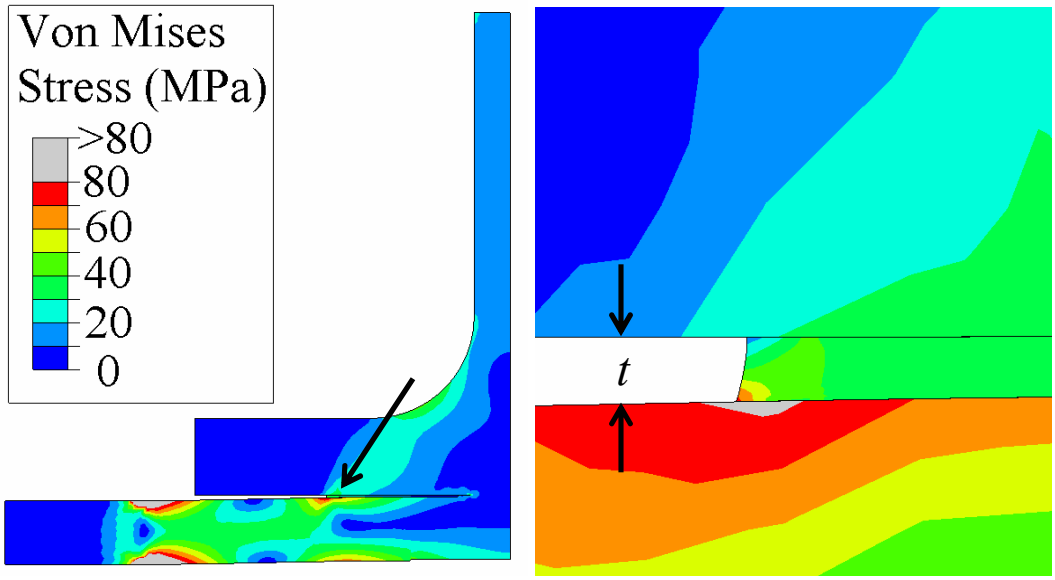

Figure 3.28. Von Mises stress distribution in (a) partially filled sealant model (b) at the location of maximum stress in the sealant (indicated by arrow in (a)) for $t = 0.1$ mm.

3.3.5. Effects of Asymmetry and Grip Conditions. The asymmetric model is composed of a partial hook defect on one notch representing the advancing side of the weld and a flat interface notch representing the retreating side of the weld. Crack

propagation was modeled from the advancing side notch at 75º based on crack rotation tendencies determined in section 3.3.3 (see Table 3.14). K_I as a function of crack length for both advancing side and retreating side notches with boundary conditions representing rigid and universal upper grips are shown in Figure 3.29.

The difference in K_I for each grip condition at zero crack length is negligible. Thus, crack initiation life is not expected to be affected by grip condition. K_I increases more rapidly with crack length at the advancing side crack tip for the universal grip condition than the rigid grip condition and remains higher throughout crack propagation. At the retreating side notch, K_I only increases with crack length for the rigid grip condition until the advancing side crack has propagated nearly entirely through the top-skin. K_I at the retreating side notch increases dramatically after complete cracking through the top-skin for both grip conditions.

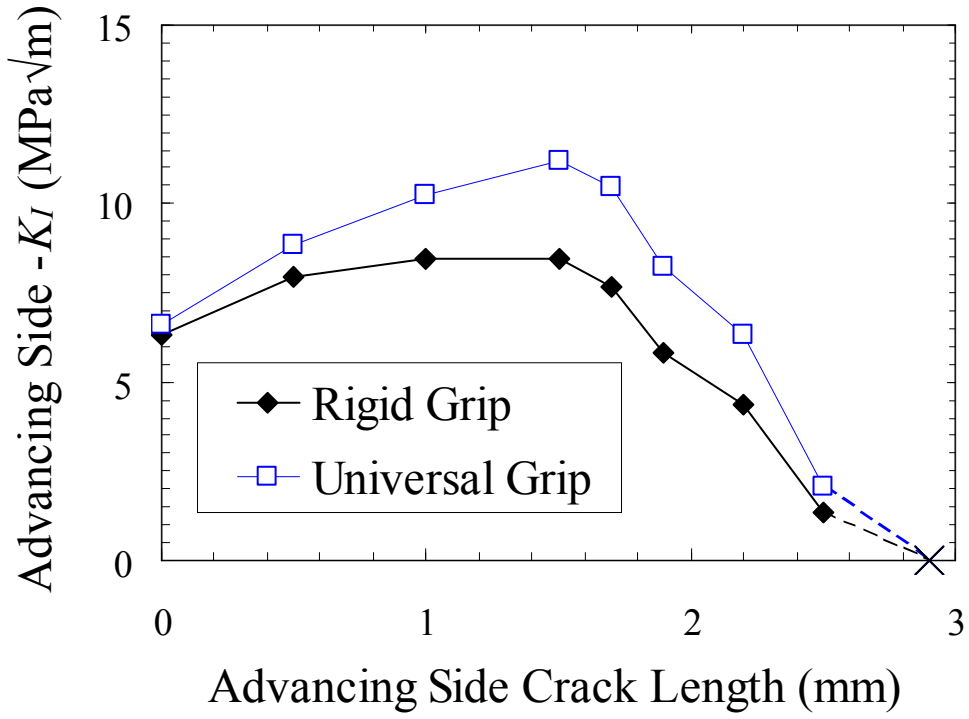

(a)

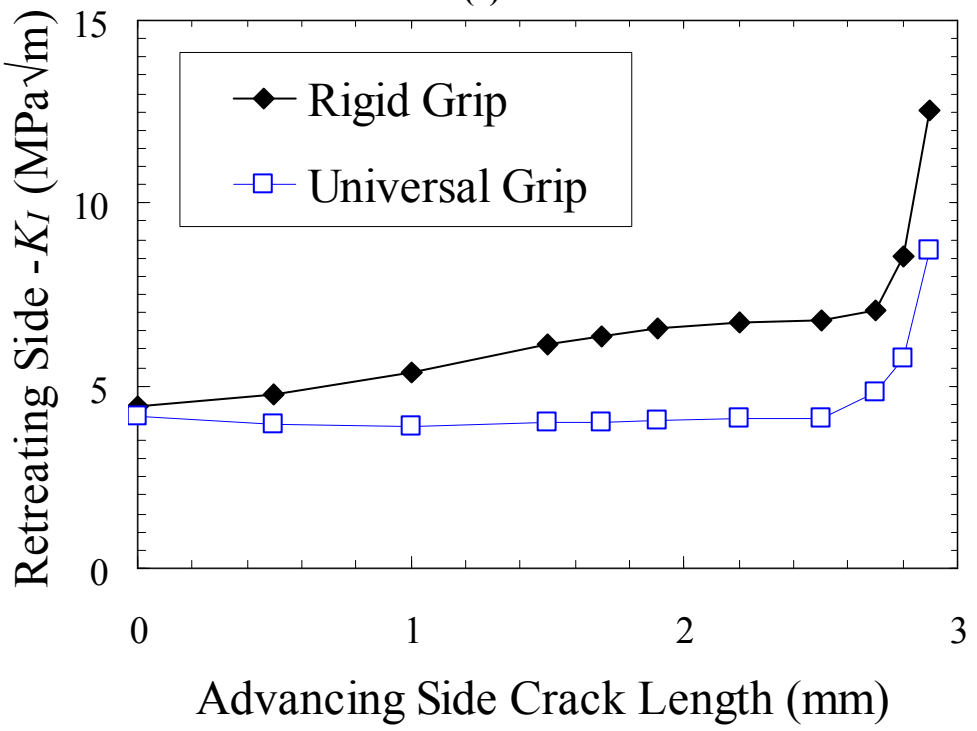

(b)

Figure 3.29. K_I at (a) advancing side and (b) retreating side notches for rigid and universal grip conditions as a function of advancing side crack length. Complete cracking through the top-skin occurs at crack length of 2.9 mm.

4. DISCUSSION

4.1. TENSILE WELD STRENGTH

The weld strength shows a strong dependence on type of prior anodization (see Table 3.5). Weld strength and weld dimensions are comparable for bare welds and welds with prior thin film sulfuric acid anodization without sealant or with DAPCO^{TM} rubber sealant. Welds with prior standard sulfuric acid anodization possessed a thicker anodization layer (see Table 3.4). It is thought that the excess oxide debris field in the welds with standard sulfuric acid anodization may have reduced the weld nugget strength.

Welds with Corvel^{TM} nylon sealant and prior anodization exhibited reduced strength compared with welds with other sealants (see Table 3.5). Nylon sealed welds with prior anodization were welded at 1100 rpm and 3.6 mm/s (8.5 in/min) whereas all other welds and nylon sealed welds without prior anodization were welded at 900 rpm and 4.2 mm/s (10 in/min). Per eq. 1, the higher rotation speed and slower traverse rate should increase the heat input and produce a hotter weld. This may have resulted in a higher extent of overaging in the heat affected zones and a reduction in total weld strength. Additionally, the more extensive hook defect (hook intrusion depth y = 0.2 vs. 0.05 mm; hook intrusion angle θ_h = 45 vs. 30º) and wider weld width ($2x$ = 4.2 vs. 3.6 mm) of nylon sealed welds with the higher heat input may have contributed to stable crack propagation at lower applied loads. Finite element modeling results predict an increase in stress intensity factor with increasing $2x$ (Figure 3.25), increasing θ_h (Figure 3.26a), and increasing y (Figure 3.26b) in the ranges observed in these welds.

4.2. LAP JOINT SEALANT STRENGTH

Welds sealed with DAPCO^{TM} rubber exhibited cohesive sealant failure at the onset of fatigue loading. No strength or stiffness contribution was observed during tensile testing of welds with rubber sealant. The rubber sealant is expected to possess a low elastic modulus consistent with elastomers. Therefore, the strain in the sealant is expected to be predictable by the opening of the faying surface gap in weld coupons without sealants. Finite element modeling of a weld without sealant predicts the widest gap opening of 94 μm under an applied load of 78.8 N/mm. The unloaded gap size in rubber sealed welds is 220 ± 20 μm. Therefore, a displacement of 94 μm would yield 39 – 47 % strain in the sealant. An elastomer sealant likely requires greater than 50 % elongation to failure to ensure that it does not fail cohesively upon fatigue loading.

The relatively stiff nylon-11 sealant contributes substantially to the weld stiffness (see Figure 3.10). The strength of the nylon sealant bond is dependent on the prior material surface treatment. The bond strength is reduced on an anodized surface compared with bare aluminum. This may be the result of a combination of reduced dynamic wetting due to the porous nature of an anodized surface and premature bond failure by delamination of the anodized layer as shown in Figure 3.11. Delamination of the anodized layer always occurred on the wrought top-skin probably because the machined surface of the cast T-rail was rougher and therefore likely provided better mechanical adhesion.

The nylon sealed welds with bare aluminum and with prior standard sulfuric acid anodization (compared with those studied by Van Aken et al. [3]) were welded with thinner prior sealant thickness (100-130 μm) than nylon sealed welds with thin film

sulfuric acid anodization (150-200 μm). It is thought that the thicker sealant required more heat to melt and press out of the faying surface gap. Therefore, the melted sealant in the welds with thin film sulfuric acid anodization probably did not reach as high a temperature and did not wet the anodized surfaces as well resulting in reduced bond strength. During water-cooled sectioning, handling, and fixturing of specimens, the weak bonds probably failed and no bond strength was detected during tensile loading. After a 10 min heat treatment at 200 ºC, the bonds were repaired and exhibited comparable strength to other nylon sealed welds (see Table 3.6). This step may not be necessary if the sealant thickness is maintained between 100 and 150 μm with proper control of welding parameters. Thicknesses below 100 μm may not adequately fill the faying surface gap since welds without sealant exhibited gaps between 60 and 140 μm wide. Finite element modeling predicts significantly higher stresses in the sealant for partially filled faying surface gaps (see Figure 3.28) so bond strength may also suffer if the faying surface gap is incompletely filled.

Successful nylon sealant bonding with bare aluminum was achieved at reduced welding heat index at 900 rpm and 4.2 mm/s (10 in/min) traverse rate. Standard anodized welds did not exhibit successful as-welded bonding until parameters were adjusted to 1100 rpm and 3.6 mm/s (8.5 in/min). This may reflect a higher heat input required for the nylon to wet and adhere the porous anodized surface as opposed to the bare aluminum surface. Wetting a rough surface requires additional time and pressure, especially with a viscous fluid (see section 1.5).

4.3. FATIGUE RESULTS WITHOUT SEALANTS

Ambient fatigue results comparing welds with bare aluminum and prior standard anodization reveal a slightly reduced fatigue life at 1 % sample population failure for prior anodized welds (see Table 3.7). This is consistent with the reduced strength of the anodized welds and likely results in accelerated crack propagation across the weld nugget through the oxide debris field adjacent to the retreating side faying surface notch (see Figures 1.9c, 3.7c). However, at greater than 10 % sample population failure, ambient fatigue life is comparable between bare and anodized welds. The tendency for the fatigue cracks to propagate through the top-skin is corroborated by the crack propagation direction ranging between 35º and 76º predicted by finite element modeling for models representative of flat and hook faying surface notches (see Table 3.14). In the standard and thin film anodized welds, the oxide debris field adjacent to the retreating side notch provided an easy crack path. Finite element modeling also justifies the tendency for fatigue initiation to occur at the advancing side notch before the retreating side notch. Higher K_I is anticipated with increasing hook intrusion depth and angle (see Figure 3.26). Therefore, the hook defect at the advancing side notch (see Figures 1.9, 3.7) is expected to contribute to significantly higher notch stresses and accelerated fatigue cracking.

Fatigue striations in the fatigue fracture in ambient testing indicate a ductile, transgranular fatigue path (see Figure 3.20), typical of fatigue of aluminum in ambient air at moderate to high *da/dN* (see section 1.4.1) [58]. Striations are also observed in corrosion fatigue (see Figure 3.22), although the striations are significantly larger consistent with faster fatigue propagation rates and shorter fatigue life. Corrosion fatigue transitions across grains are more angular and abrupt than those in ambient fatigue. This

may indicate a more brittle transgranular cracking mode as observed in fatigue of 7017 in 3.5 % NaCl at ΔK between 10 and 18 MPa$\sqrt{m}$ at f = 4 Hz [8]. The similarity between fatigue fractures in ambient air and in 3.5 % NaCl may be related to the presence of water vapor in ambient air. Water vapor in ambient air increases crack propagation rates and influences crack morphology presumably due to hydrogen embrittlement, although to a smaller extent than water in aqueous chloride solutions (see section 1.4.1) [57 – 58, 61] .

4.4. COMPARISON BETWEEN FATIGUE TEST FIXTURES

DAPCO^{TM} rubber sealed weld specimens tested in the aluminum fixture exhibited a higher cyclic loop displacement (see Figure 3.16) and significantly reduced fatigue life than those tested in the steel fixture (see Table 3.8) regardless of the upper grip condition. The increased cyclic loop displacement implies greater crack opening and therefore higher stress intensity factors at the crack tips. This is likely a combination of lower stiffness of the aluminum grips and wider effective clamping distance due to wear of aluminum clamping teeth. Testing at fifty percent reduced maximum applied load (78.8 to 52.5 N/mm) with the aluminum fixture yielded similar fatigue life data to tests with the steel fixture at 78.8 N/mm.

Independent of the top-skin clamping fixture used, testing with the rigid grip yielded reduced fatigue life compared with testing with the universal grip. Prior to fatigue initiation, stress intensity factors for each condition at each side notch are similar according to finite element modeling results (see Figure 3.29). Therefore, reduced fatigue initiation life of the rigid grip condition may be related to slight fixture misalignment. The misalignment was likely parallel to the direction of the weld since

specimens were tested in both orientations relative to the weld (i.e. with advancing side on the left and on the right) and no trend was observed regarding specimen orientation and fatigue life.

During fatigue propagation, stress intensity factors are influenced by the grip condition according to finite element modeling (see Figure 3.29). After the advancing side fatigue crack propagates about halfway through the top-skin, the stress intensity factor at the retreating side notch is increased from 4.4 to 6.4 MPa√m for the rigid grip condition but remains unchanged for the universal grip condition. Therefore, fatigue at the retreating side notch is expected to initiate sooner and fail the weld specimen sooner with the rigid grip than with the universal grip. This was observed experimentally with both the steel fixture and the aluminum fixture.

For all rubber sealed weld specimens tested, the advancing side crack did not propagate entirely through the top-skin. Since the universal joint increases the stress intensity factors at the propagating advancing side crack tip, the use of the universal joint may reduce the total fatigue life if it causes complete fracture through the top-skin whereupon the stress intensity factor at the retreating side notch jumps to 8.7 MPa√m with the universal grip (see Figure 3.29). Fatigue testing of weld specimens without sealant using the rigid grip (section 3.2.3) did not fail through the top-skin whereas those tested with the universal grip did fail through the top-skin (section 3.2.5). Assuming the different applied loads and grip fixtures only had symmetrical effects on the notch stresses, the universal grip probably contributed to a reduction in fatigue life of unsealed welds compared with that of testing with the rigid grip. The upper grip condition was not isolated in any experiment with unsealed welds so this is not verified experimentally.

4.5. SEALANTS IN AMBIENT FATIGUE

The cyclic lives for 1 % sample population failure for welds with Corvel™ nylon-11 sealant were comparable to welds without sealant as determined by preliminary testing with prior standard anodization (see Table 3.7) and testing with thin film sulfuric acid anodization (see Table 3.9). At larger % sample population failures, the nylon sealant exhibits a dramatic improvement in fatigue life. The improvement is thought to rely on the mechanical contribution of the sealant. While the sealant bond remains in tact, the maximum K_I at the notches is maintained below 0.4 MPa√m for final sealant layer thickness (t) of 100–200 μm as predicted by finite element modeling, regardless of the extent of the hook defect (see Table 3.15). The dependence of K_I on t is irrelevant since for both cases it is well below 2.7 MPa√m, the threshold K_{max} for 2024 at $R = 0.1$ [33].

Once the sealant bond has failed on one side of the weld, K_I increases above the threshold value and fatigue can ensue in a similar fashion as with welds without sealant, particularly if the advancing side sealant bond fails first. If the retreating side fails first, fatigue initiation is delayed as shown in Table 3.10. This is probably because the hook defect is more severe at the advancing side notch than the retreating side notch (see Figure 3.9) and thus K_I is expected to be higher at the advancing side notch. The large variance in fatigue life for the nylon sealed welds as evidenced by the lower Weibull modulus can be attributed to the large variance in fatigue life of the sealant bond. Fatigue of the sealant bond is controlled by the size of the largest interfacial void or void in the bulk of the sealant. The voids in the bulk of the sealant are typically about 2 mm in size (see Figure 3.11). These voids may be indicative of incomplete sealant fill of the faying surface gaps. In unsealed welds, the faying surface gaps are opened 60 – 140 μm due to

residual stresses. However, the finger clamp pressure over the faying surface gaps during the weld was sustained a sufficient length of time after welding to ensure polymer solidification. The gaps were not allowed to open up from residual stresses while the polymer remained melted expect in the case of repaired welds in which the polymer was remelted. However, the voids were observed in welds with and without repair. Therefore, it seems more likely that the voids are the result of polymer decomposition at the high welding temperatures, similar to the voids obtained during tensile bar preparation (see section 3.1.3).

Welds with DAPCO^{TM} rubber sealant are comparable in fatigue life with those without sealant for the prior thin film sulfuric acid anodization condition (see Table 3.9). This is consistent with the observation from tensile testing that the rubber sealant provides negligible mechanical contribution to the lap joint. The fatigue initiation life is higher for welds with rubber sealant than for those without sealant. In general, the advancing side crack did not propagate through the top-skin because of the reduced size of the hook defect at the advancing side notch for welds with rubber sealant and the corresponding delayed fatigue crack initiation (see Table 3.4). However, the propagation life of the rubber sealed welds was shorter than that of the welds without sealant. The retreating side notch on the welds without sealant was slightly hooked towards the cast T-rail (see Figure 3.7c) which may have reduced the stress intensity factor at this notch and delayed fatigue initiation. Therefore, compared with unsealed welds, rubber sealed welds have delayed fatigue cracking at the advancing side notch and accelerated fatigue cracking at the retreating side notch because of the size and orientation of the notches. These effects seem to have cancelled each other in order to yield similar total fatigue life

results between unsealed and rubber sealed welds. Adding a highly viscous liquid, such as the uncured rubber sealant, between the parts to be welded changes the notch sizes and orientations and influences fatigue cracking in the lap joint.

4.6. SEALANTS IN CORROSION FATIGUE

Fatigue life with and without sealants in corrosion fatigue conditions are comparable (see Table 3.11). Ideally, an effective sealant will have comparable fatigue life in ambient and corrosion fatigue conditions. Neither sealant candidate is ideally effective as an immersion sealant by this criterion.

The DAPCO^{TM} rubber sealant failed cohesively at low loads as in ambient fatigue, opening the faying surface gaps, and allowing fluid access to the faying surface notches. However, the rubber sealed weld coupons exhibited improved fatigue life over the welds without sealant. The presence of the rubber may have reduced or delayed fluid access to the faying surface notches. This may have been accomplished by the sealant closing the gap during fatigue unloading or by only partial failure of the sealant in which passages are created allowing restricted fluid flow to the notches.

The lack of the effectiveness of the Corvel^{TM} nylon-11 sealant is attributed to the loss of adhesive bond strength between the nylon and the anodized aluminum in water. This is supported by the observed change from a combination of adhesive and cohesive sealant failure to entirely adhesive failure, a lack of anodized layer delamination, and the consistency of failure of the sealant bond early in the fatigue loading in corrosion fatigue conditions. The sudden nature of the loss of bond strength with the immersion in water suggests a reversible effect due to the reduction of chemical bonding between the

adhesive (nylon) and adherend (aluminum) rather than a degradation process. The effect on ideal bond strength is best estimated by calculating the work of adhesion (W_a) in air and in water (see eq. 5). For W_a in air, γ_α and γ_β are the surface tensions of each component (Corvel^{TM} nylon-11 and anodized aluminum) in air. These values are calculated and presented in Table 3.2. For W_a in water, γ_α and γ_β are the interfacial tensions of each component with water (presented in Table 3.2). For both conditions, $\gamma_{\alpha\beta}$ is the interfacial tension between the components (presented in Table 3.3). The calculated W_a for each condition is shown in Table 4.1.

Table 4.1. Ideal Nylon-Aluminum Bond Energy

Environment	W_a (mJ/m^2)
Air	110.5
Water	30.4

There is a significant loss in ideal bond strength between the nylon and aluminum with the penetration of water. Rapid penetration of the interface can occur especially with a porous anodized layer. There may be an additional loss in bond strength related to ionic effects. Comyn proposed the reduction in adhesive bond strength between ionic materials is related to the reduction of ionic attractive force [113]. The ionic attractive force is inversely proportional to the relative permittivity k of the medium. In dry conditions, this may be an average of the adhesive and adherend. For most polymers and for aluminum oxide, $k < 10$; for water, $k \approx 80$. If water molecules penetrate the interface, the relative permittivity between bonded ionic groups of the adhesive and adherend

increases and therefore the ionic attractive force decreases. These losses in adhesive bond strength are dependent on the presence of water and should be recoverable by drying.

Masking of the nylon sealant was successful in one weld coupon in that fatigue life in corrosion fatigue conditions was comparable to that in ambient fatigue conditions. Therefore, the use of an additional sealant to mask the faying surface gap sealant may be viable. However, this further complicates the assembly, would require an additional fabrication step, and would require a masking sealant with adequate long-term corrosion protection. If the masking sealant is penetrated in one location, fluid could access the entirety of the weld on one side, and immediately break the sealant bond. A simpler alternative would be to use a polymer with stronger bond strength in water. This may be a challenge since polymers designed for adhesion, such as acrylics and epoxies, exhibit reduced bond strength with metals in water [114 - 117].

4.7. COMPARISON BETWEEN CORVEL™ AND PURE NYLON-11

Properties influencing the adhesive bond strength of pure nylon-11 and Corvel™ nylon-11 on anodized aluminum include tensile properties and dynamic wettability. The tensile properties of each sealant material are equivalent at least below the elastic limit (section 3.1.3). Dynamic wetting may be different between each material. However, the adhesive bond strengths of Corvel™ nylon-11 and pure nylon-11 on a thin film sulfuric acid anodized aluminum surface are statistically equivalent (see Table 3.1). Two possible explanations exist for this equivalency. (1) The reduced equilibrium wetting predicted for Corvel™ nylon-11 in section 3.1.5 is negligible with regards to dynamic wetting on a

rough surface. (2) The increase in viscosity predicted by the incorporation of fillers per eq. 8 in Corvel™ nylon-11 is exceeded by the reduced viscosity due to a reduced molecular weight as determined by thermal analysis (section 3.1.1). The dynamic wetting of a rough surface is sensitive to the viscosity per eqs. 6 and 7 such that if Corvel™ nylon-11 is less viscous than pure nylon-11, they may exhibit similar dynamic wetting even though pure nylon-11 has better predicted equilibrium wetting.

5. CONCLUSIONS

Polymer sealants have been successfully incorporated into the friction stir welding process with minor effects on the tensile strength of lap joints. Rubber sealant applied in the uncured form has negligible effects on the weld tensile strength and fatigue strength and can be welded with the same parameters as welds without sealant. However, the rubber sealant used fails cohesively at low applied loads and therefore only exhibits minor improvement over welds without sealant in corrosion fatigue. The effectiveness of the elastomer sealant is limited by its cohesive mechanical properties, specifically the elongation to failure. Improvements in the corrosion fatigue resistance of elastomer sealed welds may be achieved by using a material with > 50 % elongation that is still resistant to the high temperatures of friction stir welding.

The most notable effects in welds with nylon-11 sealant are those related to the higher heat input required to melt a thermoplastic sealant. More severe hook defects and a wider weld joint width correspond with higher stress intensity factors at the faying surface notches of nylon sealed welds and thus reduce weld strength if the sealant fails. In fatigue loading at small loads, this is eclipsed by the reduction of notch stresses due to the load-bearing capacity of the nylon sealant. Fatigue life of the nylon sealed welds in ambient conditions is comparable to or higher than that of welds with rubber sealant or no sealant depending on the fatigue life of the nylon bond. The fatigue properties are limited by the adhesive bond strength of the nylon sealant and aluminum interface. Immersed in an aqueous solution, the bond strength of the nylon sealant is theoretically reduced by 70 % and fails, which immediately exposes the faying surface notches and

negates any beneficial effect of the sealant as exhibited in ambient fatigue testing. Additional masking of the sealant can restore the ambient fatigue life in corrosion fatigue conditions, but adds additional risk factors associated with requiring an uncompromised and corrosion resistant mask. Also, the masking sealant would require high temperature resistance (~200 ºC) especially if one aims to take advantage of the reparability of the nylon sealant.

It is now known that a curable polymer can be used as a sealant so long as its decomposition at high temperatures for short times is minimal. Regarding hard polymer sealants with adhesive limitations, epoxies and other adhesive type curable polymers may be required to achieve sufficient bond strength in aqueous environments with minimal risk factors. Rubber sealants with cohesive limitations need to possess significant elongation (> 50 %) to maintain cohesion in fatigue loading.

APPENDIX

SEALANT SHEET FABRICATION

Sealant sheets were fabricated by a process similar to tape casting. A 19.1 mm (0.75 in) thick aluminum plate was evenly heated and maintained at a surface temperature of 200 – 250 ºC (392 – 482 ºF) via a series of hot plates (see Figure A1). The sealant material (in the form of powder or pellets) was placed over one end of the plate on a 1.6 mm (0.06 in) thick aluminum sheet. Once melted, the material was spread across the aluminum sheet with a scraper with adjustable height, similar to a doctor blade in tape casting (see Figure A2). The aluminum sheet and polymer spread were removed from the plate and rapidly air-cooled below the polymer melting point, 190 ºC (375 ºF). While still hot, the sealant sheet was gently peeled from the aluminum sheet with a razor blade. Wetting the interface with a small amount of water aided the separation. Resulting sheets were consistent in thickness to ± 25 μm (0.001 in) and were trimmed to fit the T-rail faying surface.

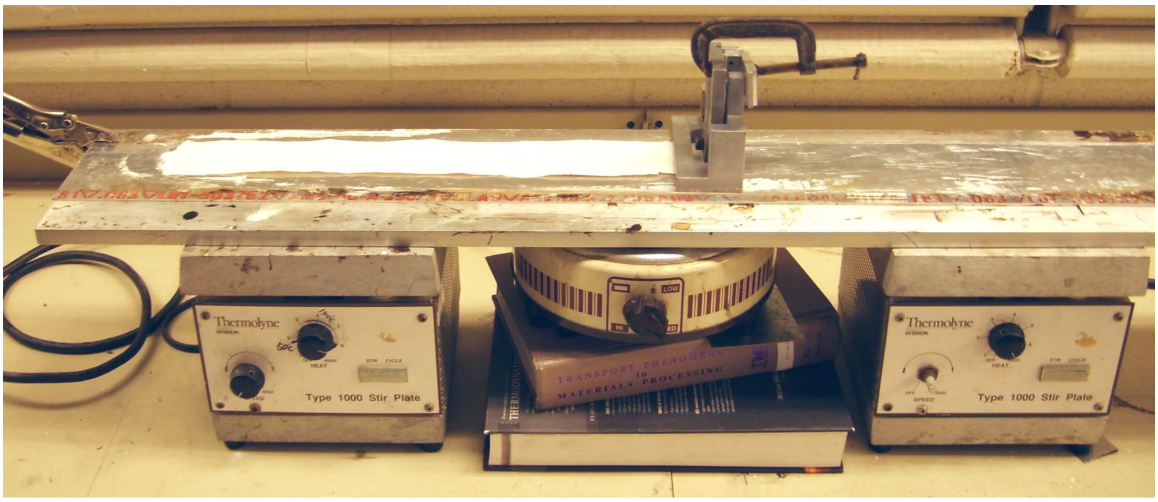

Figure A1. Sealant sheet fabrication process. Thin aluminum sheet is placed on thick aluminum plate across several hot plates. The temperature of the thick aluminum plate is consistent throughout and is maintained throughout successive sheet fabrication.

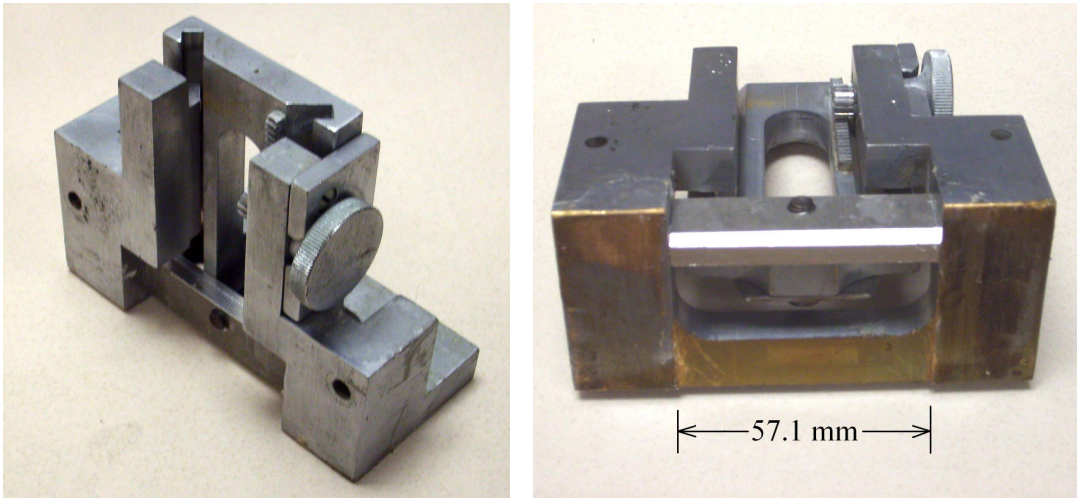

(a) **(b)**

Figure A2. (a) Top view and (b) bottom view of scraper used for spreading of sealant material into consistent thickness sheet. The height is adjustable and was secured in place during use. Resulting sheets were 57.1 mm (2.25 in) wide corresponding with width of the gate.

REFERENCES

[1] P. S. Pao, E. Lee, C. R. Feng, H. N. Jones, D. W. Moon, "Corrosion Fatigue in FSW Welded Al 2519," in *Friction Stir Welding and Processing II*, The Minerals, Metals & Materials Society, Warrendale, PA (2003), pp. 113-22.

[2] P. S. Pao, S. J. Gill, C. R. Feng, K. K. Sankaran, "Corrosion-Fatigue Crack Growth in Friction Stir Welded Al 7050," *Scripta Materiala* **45** (2001), pp. 605-12.

[3] D. C. Van Aken, R. J. Lederich, D. L. Ballard, "Corrosion-Fatigue Studies of Friction Stir Welded Lap Joints," in *Fatigue* 2006: 9th International Fatigue Congress, Atlanta, GA, paper FT 118.

[4] R. P. Gangloff, "Environment Sensitive Fatigue Crack Tip Processes and Propagation in Aerospace Aluminum Alloys," *Fatigue* **5**, A. F. Bloom (ed.), (2002), pp. 3401-34.

[5] R. S. Piascik, S. A. Willard, "The Growth of Small Corrosion Fatigue Cracks in 2024," *Fatigue & Fracture of Engineering Materials & Structures* **17**(11) (1994), pp. 1247-59.

[6] Z. M. Gasem, R. P. Gangloff, "Effect of Temper on Environmental Fatigue Crack Propagation in 7000-series Aluminum Alloys," in *Materials Science Forum* **331-7**, Trans Tech Publications Ltd., Switzerland (2000), pp. 1479-88.

[7] Z. Gasem, R. P. Gangloff, "Rate-Limiting Processes in Environmental Fatigue Crack Propagation in 7000-series Aluminum Alloys," in *Chemistry and Electrochemistry of Corrosion and Stress Corrosion Cracking: A Symposium Honoring the Contributions of R. W. Staehle*, Minerals, Metals & Materials Society, Warrendale, PA, (2001), pp. 501-21.

[8] N. J. H. Holroyd, D. Hardie, "Factors controlling crack velocity in 7000 series aluminum alloys during fatigue in an aggressive environment," *Corrosion Science* **23**(6) (1983), pp. 527-46.

[9] R.S. Piascik, R.P. Gangloff, "Environmental fatigue of an Al-Li-Cu alloy: Part I. Intrinsic crack propagation kinetics in hydrogenous environments," *Metallurgical and Materials Transactions A: Physical Metallurgy and Materials Science* **22A**(10) (1991), pp. 2415-28.

[10] *Welding, Brazing, and Soldering,* vol. 6 of *Metals Handbook,* 10th ed., American Society of Metals, Cleveland, OH (1990).

[11] W.I. Pumphrey and J.V. Lyons, "Cracking during the Casting and Welding of the More Common Binary Aluminum Alloys," *Journal of the Institute of Metals,* **74** (1948), pp. 439-55.

[12] J.K. Dawson, "Weld Crack Sensitivity of Aluminum Alloys," *Metal Progress,* **76**(1) (1959), p. 116.

[13] C.L. Cross, "Weldability of Aluminum-Lithium Alloys: An Investigation of Hot Tearing Mechanisms," Ph.D. thesis, Colorado School of Mines, Golden, CO (1986), p. 144.

[14] A. P. Reynolds, W. D. Lockwood, T. U. Seidel, "Process-Property Correlation in Friction Stir Welds," in *Materials Science Forum* **331-7**,Trans Tech Publications Ltd., Switzerland (2000), pp. 1719-24.

[15] M. B. Prime, T. Gnaeupel-Herold, J. A. Baumann, R. J. Lederich, D. M. Bowden, R. J. Sebring, "Residual Stress Measurements in a Thick, Dissimilar Aluminum Alloy Friction Stir Weld," *Acta Materialia* **54**(15) (2006), pp. 4013-21.

[16] K. V. Jata, J. J. Sankaran, J. J. Ruschau, "Friction-Stir Welding Effects on Microstructure and Fatigue of Aluminum Alloy 7050-T7451," *Metallurgical Transactions A: Physical Metallurgy and Materials Science* **31A**(9) (2000), pp. 2181-92.

[17] V. Dixit, R. S. Mishra, R. J. Lederich, "Effect of Initial Temper on Mechanical Properties of Friction Stir Welded Al-2024 Alloy," *Science and Technology of Welding and Joining* **12**(4) (2007), pp. 334-40.

[18] W. B. Lee, Y. M. Yeon, S. B. Jung, "The Mechanical Properties Related to the Dominant Microstructure in the Weld Zone of Dissimilar Formed Al Alloy Joints by Friction Stir Welding," *Journal of Materials Science* **38**(20) (2003), pp. 4183-91.

[19] M. Dunlavy, K. V. Jata, "High-Cycle Corrosion Fatigue of Friction Stir Welded 7050-T7451," in *Friction Stir Welding and Processing II*, The Minerals, Metals & Materials Society, Warrendale, PA (2003), pp. 91-6.

[20] W. J. Arbegast, "Modeling Friction Stir Joining as a Metal Working Process," in *Hot Deformation of Aluminum Alloys III*, The Minerals, Metals & Materials Society, San Diego, CA (2003).

[21] W. F. Hosford, *Mechanical Behavior of Materials*, Cambridge University Press, New York, NY (2005), p. 197.

[22] R. Galatolo, A. Lanciotti, "Fatigue Crack Propagation in Residual Stress Fields of Welded Plates," *International Journal of Fatigue*, **19**(1) (1997), pp. 43-9.

[23] L. E. Murr, Y. Li, E. A. Trillo, R. D. Flores, J. C. McClure, "Microstructures in Friction-Stir Welded Metals," *Journal of Materials Processing & Manufacturing Science* **7**(2) (1998), pp. 145-61.

[24] K. Sadananda, A. K. Vasudevan, R. L. Holtz, E. U. Lee, "Analysis of Overload Effects and Related Phenomena," *International Journal of Fatigue* **21**(Suppl.) (1999), pp. S232-46.

[25] K. Sadananda, A. K. Vasudevan, "Multiple Mechanisms Controlling Fatigue Crack Growth," *Fatigue & Fracture of Engineering Materials & Structures* **26**(9) (2003), pp. 835-45.

[26] W. Elber, "The Significance of Fatigue Crack Closure," in *Damage Tolerance in Aircraft Structures*, ASTM STP 486. Philadelphia, PA (1971), pp. 230–42.

[27] A. H. Noroozi, G. Glinka, S. Lambert, "A Study of the Stress Ratio Effects on Fatigue Crack Growth Using the Unified Two-Parameter Fatigue Crack Growth Driving Force**,"** *International Journal of Fatigue* **29**(9-11) (2007), pp. 1616-33.

[28] D. Kujawski, "A New $(\Delta K^{+}K_{max})^{0.5}$ Driving Force Parameter for Crack Growth in Aluminum Alloys," *International Journal of Fatigue* **23**(8) (2001), pp. 733-40**.**

[29] G. Maymon, "A 'Unified' and a $(\Delta K^{+} \bullet K_{max})^{1/2}$ Crack Growth Models for Aluminum 2024-T351," *International Journal of Fatigue* **27**(6) (2005), pp. 629-38.

[30] C.M. Pang, J.H. Song, "Crack Growth and Closure Behavior of Short Fatigue Cracks," *Engineering Fracture Mechanics* **47**(3) (1994), pp. 327-43.

[31] X. R. Wu, J. C. Newman, W. Zhao, M. H. Swain, C. F. Ding, E. P. Phillips, "Small Crack Growth and Fatigue Life Predictions for High-Strength Aluminum Alloys. Part I: Experimental and Fracture Mechanics Analysis," *Fatigue & Fracture of Engineering Materials & Structures* **21**(11) (1998), pp. 1289-306.

[32] M. H. Swain, J. C. Newman, Jr., E. P. Phillips, R. A. Everett, Jr., "Fatigue Crack Initiation and Small Crack Growth in Several Airframe Alloys," in *NASA Technical Memorandum 102598*, National Aeronautics and Space Administration, Hampton, VA (1990).

[33] G. Bussu, P. E. Irving, "The Role of Residual Stress and Heat Affected Zone Properties on Fatigue Crack Propagation in Friction Stir Welded 2024-T351 Aluminium Joints**,"** *International Journal of Fatigue* **25**(1) (2002), pp. 77-88.

[34] D. Booth, I. Sinclair, "Fatigue of Friction Stir Welded 2024-T351 Aluminium Alloy," in *Materials Science Forum* **396-402**, Trans Tech Publications Ltd., Switzerland (2002), pp. 1671-6.

[35] P. Prevéy, D. Hornbach, P. Mason, "Improving Corrosion Fatigue Performance of AA2219 Friction Stir Welds with Low Plasticity Burnishing," in *Proceedings from the 1st International Surface Engineering Congress*, ASM International, Materials Park, OH (2003), pp. 131-7.

[36] N. Jayaraman, P. Prevéy, M. Mahoney, "Fatigue Life Improvement of an Aluminum Alloy FSW with Low Plasticity Burnishing," in *Friction Stir Welding and Processing II*, The Minerals, Metals & Materials Society, Warrendale, PA (2003).

[37] P. Prevéy, M. Mahoney, "Improved Fatigue Performance of Friction Stir Welds with Low Plasticity Burnishing: Residual Stress Design and Fatigue Performance Assessment," *Materials Science Forum* **426-432** (2003), pp. 2933-40.

[38] T. P. Gabb, J. Telesman, P. Kantzos, P. S. Prevey, "Surface Enhancement of Metallic Materials," *Advanced Materials & Processes* **160**(1), pp. 69-72.

[39] R. P. Wei, J. D. Landes, "Correlation between Sustained-Load and Fatigue Crack Growth in High-Strength Steels," *Materials Research and Standards*, **9**(7) (1969), pp. 25-8.

[40] W. W. Gerberich, J. P. Birat, V. F. Zackay, "Superposition Model for Environmentally-Assisted Fatigue Crack Propagation," in *Corrosion Fatigue: Chemistry, Mechanisms, and Microstructure* (1972), p. 396-408.

[41] F. P. Ford, "Corrosion Fatigue Crack Propagation in Aluminum-7% Magnesium Alloy," *Corrosion* **35**(7) (1979), p. 281

[42] G. M. Bond, I. M. Robertson, H.K. Birnbaum, "The Influence of Hydrogen on Deformation and Fracture Processes in High-Strength Aluminum Alloys," *Acta Metallurgica* **35** (1987), pp. 2289-96.

[43] G. M. Scamans, R. Alani, P. R. Swann, "Preexposure Embrittlement and Stress Corrosion Failure in Aluminum-Zinc-Magnesium Alloys," *Corrosion Science* **16**(7) (1976), pp. 443-59.

[44] L. Christodoulou, H. M. Flower, "Hydrogen Embrittlement and Trapping in Aluminum-6% Zinc-3% Magnesium," *Acta Metallurgica* **28**(4) (1980), pp. 481-7.

[45] D. J. Duquette, *Mechanisms of Corrosion Fatigue of Aluminum Alloys*, Ft. Belvoir Defense Technical Information Center, Fort Bellvoir, VA (1981).

[46] R. Balasubramaniam, D. J. Duquette, K. Rajan, "Hydride Formation in an Aluminum-Lithium-Copper Alloy," *Acta Metallurgica et Materialia* **39**(11) (1991), pp. 2607-13.

[47] C. D. S. Tuck, "Evidence for the Formation of Magnesium Hydride on the Grain Boundaries of Al-Mg and Al-Zn-Mg Alloys During their Exposure to Water Vapor," in *Hydrogen Effects in Metals*, I. M. Bernstein and A. T. Thompson (eds.), The Metallurgical Society of AIME, Warrendale, PA, (1980), pp. 503-11.

[48] Z. M. Gasem, *Frequency Dependent Environmental Fatigue Crack Propagation in the 7xxx Alloy /Aqueous Chloride System*, Thesis (Ph. D.), University of Virginia, Charlottesville, VA (1999).

[49] R. W. Wei, P. S. Pao, R. G. Hart, T. W. Weir, G. W. Simmons, "Fracture Mechanics and Surface Chemistry Studies of Fatigue Crack Growth in an Aluminum Alloy," *Metallurgical and Materials Transactions A: Physical Metallurgy and Materials Science* **11A**(1) (1980), pp. 151-8.

[50] R. J. Gest, A. R. Troiano, "Stress Corrosion and Hydrogen Embrittlement in an Aluminum Alloy," *Corrosion* **30**(8) (1974), p. 274-9.

[51] N. J. Holroyd, D. Hardie, "Strain-Rate Effects in the Environmentally Assisted Fracture of a Commercial High-Strength Aluminum Alloy," *Corrosion Science* **21**(2) (1981), pp. 129-44.

[52] Ch. Zamponi, St. Sonneberger, M. Haaks, I. Mueller, T. Staab, G. Tempus, K. Maier, "Investigation of Fatigue Cracks in Aluminium Alloys 2024 and 6013 in Laboratory Air and Corrosive Environment," *Journal of Materials Science* **39**(23) (2004), pp. 6951-6.

[53] I. Haase, K. Nocke, H. Worch, G. Zouhar, G. Tempus, "An Investigation of the Fatigue Behaviour of the Aluminium Alloy AA 6013 T6 in a Corrosive Medium," *Praktische Metallographie* **38**(3) (2001), pp. 119-37.

[54] R.P. Gangloff, "Diffusion Control of Hydrogen Environment Embrittlement in High Strength Alloys," in *Hydrogen Effects on Material Behavior and Corrosion Deformation Interactions*, Minerals, Metals & Materials Society, Warrendale, PA, (2003), pp. 477-97.

[55] J.P. Hirth, "Effects of Hydrogen on the Properties of Iron and Steel," *Metallurgical Transactions A: Physical Metallurgy and Materials Science* **11A**(6) (1980), pp. 861-90.

[56] M. Kurkela, R. M. Latanision, "The Effect of Plastic Deformation on the Transport of Hydrogen in Nickel," *Scripta Metallurgica* **13**(10) (1979), pp. 927-32.

[57] R. D. Carter, E. W. Lee, E. A. Starke, Jr., C. J. Beevers, "The Effect of Microstructure and Environment on Fatigue Crack Closure of 7475 Aluminum Alloy," *Metallurgical Transactions A: Physical Metallurgy and Materials Science* **15A**(3) (1984), pp. 555-63.

[58] B. R. Kirby, C. J. Beevers, "Slow Fatigue Crack Growth and Threshold Behavior in Air and Vacuum of Commercial Aluminum Alloys," *Fatigue of Engineering Materials and Structures* **1**(2) (1979), pp. 203-15.

[59] A. K. Vasudevan, S. Suresh, "Influence of Corrosion Deposits on Near-Threshold Fatigue Crack Growth Behavior in 2XXX and 7XXX Series Aluminum Alloys," *Metallurgical Transactions A: Physical Metallurgy and Materials Science* **13**(12) (1982), pp. 2271-80.

[60] F.-S. Lin, E. A. Starke, Jr., "The Effect of Copper Content and Deformation Mode on the Fatigue Crack Propagation of Al-6Zn-2Mg-xCu Alloys at Low Stress Intensities," *Materials Science and Engineering* **45**(2) (1980), pp. 153-65.

[61] D. Li, R.P. Gangloff, G.H. Bray, M.V. Glazov, R.J. Rioja, "Aging Dependent Intrinsic Fatigue Crack Propagation in AA2024," *Advances in the Metallurgy of Aluminum Alloys*, M. Tiryakioglu (ed.), ASM International, Materials Park, OH (2001), pp. 105-18.

[62] A. J. Davenport, R. Ambat, M. Jariyaboon, B. J. Connolly, S. W. Williams, D. A. Price, A. Wescott, P. C. Morgan, "Corrosion of Friction Stir Welds in Aerospace Alloys," in *Proceedings - Electrochemical Society*, Electrochemical Society, Pennington, NJ (2004), pp. 403-412.

[63] M. Jariyaboon, A. J. Davenport, R. Ambat, B. J. Connolly, S. W. Williams, D. A. Price, "Corrosion of a Dissimilar Friction Stir Weld Joining Aluminum Alloys AA2024 and AA7010," *Corrosion Engineering, Science and Technology* **41**(2) (2006), pp. 135-42.

[64] K. S. Ferrer, R. G. Kelly, "Development of an Aircraft Lap Joint Simulant Environment," *Corrosion* **58**(5) (2002), pp. 452-9.

[65] *Standard Practice for Modified Salt Spray (Fog) Testing,* ASTM G 85 – 02, American Society for Testing of Materials (2002).

[66] J. B. Lumsden, M. W. Mahoney, G. Pollock, C. G. Rhodes. "Intergranular Corrosion Following Friction Stir Welding of Aluminum Alloy 7075-T651," *Corrosion* **55**(12) (1999), pp. 1127-35.

[67] L. Strecker, *Weldable Sealant Containing Electrically Conductive Fibers*, U.S. Patent No. 5,030,816 (1991).

[68] R. W. Clarke, *Weldable Sealant Forms*, U.S. Patent No. 4,195,215 (1980).

[69] J. L. Guthrie, H. F. Roberts, C. B. Lundsager, *Weldable Sealants for Metal and Method of Use*, U.S. Patent No. 4,559,373 (1985).

[70] D. C. Van Aken, J. A. Baumann, R. J. Lederich, R. Talwar, *Method and Sealant for Weld Joints*, U.S. Patent No. 6,905,060 (2005).

[71] B. Christner, *Welded joints with polymer sealant Welding of assembly with metal parts precoated with polymer sealant for corrosion prevention*, U.S. Patent No. 7,225,966 (2007).

[72] D. C. Van Aken, Y. Kato, *Sealant for Structural Member Joints and Methods of Using Same*, U.S. Patent App. No. 20070044406 (2007).

[73] S. Wu, *Polymer Interface and Adhesion*, Marcel Dekker, Inc., New York, NY (1982).

[74] D. R. Holmes, C. W. Bunn, D. J. Smith, "The Crystal Structure of Polycaproamide: Nylon 6," *Journal of Polymer Science* **17** (1955), pp. 159-77.

[75] S. Rosen, *Fundamental Principles of Polymeric Materials*, John Wiley & Sons, Inc., New York, NY (1993).

[76] K.-H. Illers, "Glass Transition and Cold Crystallization in 'even' and 'odd' ω-Amino-Acid Polyamdies," *Polymer* **18** (1977), pp. 551-3.

[77] H. Li, L. Wei, X. Wang, Y. Chen, "Investigation on the Influence of Water Absorption to the Mechanical Properties of Nylon 66 Materials**,"** *Gongcheng Suliao Yingyong* **36**(8) (2008), pp. 64-67.

[78] L. Avadanei, D. S. Vasilescu, S. Balint, A. Bordianu, "Effects of Water Absorption on Polyamides Characteristics," *Materiale Plastice* (Bucharest, Romania), **38**(1) (2001), pp. 34-38.

[79] E. S. Wilks (ed.), *Polymerization Processes, Synthetic Polymers,* vol. 1 of *Industrial Polymers Handbook,* Wiley-Vch Verlag, Weinheim, Germany (2001), pg. 271.

[80] R. M. Ogorkiewicz (ed.), *Engineering Properties of Thermoplastics,* Wiley-Interscience, London, England (1970), pp. 175-214.

[81] W. P. Slichter, "Crystal Structures in Polyamides Made from ω-Amino Acids," *Journal of Polymer Science* **36** (1959), pp. 259-66.

[82] G. G. Tibbetts, I. C. Finegan, C. Kwag, "Carbon Nanofiber Reinforced Thermoplastics for Enhanced Conductivity, Strength, and Tensile Modulus," in *Materials Research Society Symposium Proceedings*, Materials Research Society, Warrendale, PA (2002).

[83] P. A. Mahanwar, S. Bose, A. Tirumalai, "The Influence of Interfacial Adhesion on the Predicted Young's Modulus of Mica-Reinforced Nylon-6," *Polymer-Plastics Technology and Engineering*, **45** (2006), pp. 597-600.

[84] M. W. L. Wilbrink, A. S. Argon, R. E. Cohen, M. Weinberg, "Toughenability of Nylon-6 with $CaCO_3$ Filler Particles: New Findings and General Principles," *Polymer* **42**(26) (2001), pp. 10,155-80.

[85] A. Meddad, B. Fisa, "Stress - Strain Behavior and Tensile Dilatometry of Glass Bead-Filled Polypropylene and Polyamide 6," *Journal of Applied Polymer Science* **64**(4) (1997), pp. 653-65.

[86] L. P. Ziemianski, C. A. Pagano, M. W. Ranney, "Silanes in Elastomers: New Route to High Performance Pigmented Products," *Rubber World*, **163**(1) (1970), p. 53.

[87] L. E. Nielsen, "Mechanical Properties of Particulate-Filled Systems," *Journal Composite Material* **1**(1) (1967), pp. 100-19.

[88] L. E. Nielsen, R. F. Landel, *Mechanical Properties of Polymers and Composites*, Marcel Dekker, New York, NY (1994).

[89] O. R. Strauch, Otto R, "Spherical Glass Fillers (for Plastics)," *Society of Plastic Engineers Journal* **25**(9) (1969), pp. 38-43.

[90] R. F. Fedors, "Uniaxial Rupture of Elastomers," *Stereo Rubbers* (1977), pp. 679-804.

[91] Y.-C. Ou, Z.-Z. Yu, "Effects of Interfacial Adhesion on Microdamage and Rheological Behavior of Glass Bead Filled Nylon 6," *Polymer International* **37**(2) (1995), pp. 113-17.

[92] S. E. Berger, P. J. Orenski, M. W. Ranney, "Silane Coupling Agent for Reinforcing Mineral- Filled Nylon," in *Advances in Chemistry Series, Fillers Reinforced Plastics Symposium,* 134 (1974), pp. 73-85.

[93] A. J. Kinloch, *Adhesion and Adhesives*, Chapman and Hall, New York, NY (1987).

[94] W. D. Bascom, R. L. Cottington, C. R. Singleterry, "Dynamic Surface Phenomena in the Spontaneous Spreading of Oils on Solids," *Advances in Chemistry Series* **43** (1964), pp. 355-79.

[95] A. Einstein, "Motion of Suspended Particles in Stationary Liquids Required from the Molecular Kinetic Theory of Heat," *Annalen der Physik* **17** (1905), pg. 549.

[96] *Standard Practice of Calibration of Force-Measuring Instruments for Verifying the Force Indication of Testing Machines,* ASTM E 74 – 06, American Society for Testing of Materials (2006).

[97] *Standard Practice for Verification of Test Frame and Specimen Alignment Under Tensile and Compressive Axial Force Application,* ASTM E 1012 – 05, American Society for Testing of Materials (2005).

[98] *Standard Practice for Exposure of Metals and Alloys by Alternate Immersion in Neutral 3.5 % Sodium Chloride Solution,* ASTM G 44 – 99, American Society for Testing of Materials (1999).

[99] *Standard Test Method of Transition Temperatures and Enthalpies of Fusion and Crystallization of Polymers by Differential Scanning Calorimetry,* ASTM D 3418 – 08, American Society for Testing of Materials (2008).

[100] *Standard Test Method of Tensile Properties of Plastics,* ASTM D 638 – 08, American Society for Testing of Materials (2008).

[101] *Standard Test Methods for Stress Relaxation for Materials and Structures,* ASTM E 328 – 02, American Society for Testing of Materials (2002).

[102] *Standard Test Method for Tensile Properties of Adhesive Bonds,* ASTM D 897 – 08, American Society for Testing of Materials (2008).

[103] *Standard Practice for Surface Wettability of Coatings, Substrates and Pigments by Advancing Contact Angle Measurement,* ASTM D 7334 – 08, American Society for Testing of Materials (2008).

[104] E. Helfand, "Block Copolymers, Polymer-Polymer Interfaces, and the Theory of Inhomogeneous Polymers," *Accounts of Chemistry Research* **8**(9) (1975), pp. 295-9.

[105] H. T. Patterson, K. H. Hu, T. H. Grindstaff, "Measurement of Interfacial and Surface Tensions in Polymer Systems," *Journal of Polymer Science, Polymer Symposia* 34 (1971), pp. 31-43.

[106] D. Traini, P. Young, P. Rogueda, R. Price, "The Use of AFM and Surface Energy Measurements to Investigate Drug-Canister Material Interactions in a Model Pressurized Metered Dose Inhaler Formulation," *Aerosol Science and Technology* **40**(4) (2006), pp. 227-36.

[107] *Properties & Selection: Nonferrous Alloys & Special-Purpose Materials,* vol. 2 of *Metals Handbook,* 10th ed., American Society of Metals, Cleveland (1990), pp. 70-71, 166.

[108] T. L. Anderson, *Fracture Mechanics,* Taylor & Francis Group, LLC, Boca Raton, FL (2005), p. 111.

[109] D. M. Barnett, R. J. Asaro, "The Fracture Mechanics of Slit-Like Cracks in Anisotropic Elastic Media," *Journal of the Mechanics and Physics of Solids*, **20** (1972), pp. 353-66.

[110] H. Gao, M. Abbudi, D. M. Barnett, "Interfacial Crack-Tip Fields in Anisotropic Elastic Solids," *Journal of the Mechanics and Physics of Solids,"* **40** (1992), pp. 393-416.

[111] J. R. Rice, "A Path Independent Integral and the Approximate Analysis of Strain Concentration by Notches and Cracks." *Journal of Applied Mechanics* **35** (1968)*, pp. 145-153.*

[112] J. Hybart, T. R. White, "Surface Tension of Viscous Polymers at High Temperatures," *Journal of Applied Polymer Science* **3**(7) (1960), pp. 118-21.

[113] J. Comyn, "Diffusion of Water in Epoxides and the Durability of Adhesive Joints**,"** *Polymer Preprints (American Chemical Society, Division of Polymer Chemistry)* **24**(1) (1983), pp. 98-9.

[114] J. C. Del Real, M. C. De Santayana, J. Abenojar, M. A. Martinez, "Adhesive Bonding of Aluminium with Structural Acrylic Adhesives: Durability in Wet Environments," *Journal of Adhesion Science and Technology* **20**(6) (2006), pp. 1801-1818.

[115] M. Al-Harthi, R. Kahraman, B. Yilbas, M. Sunar, B. J. A. Aleem, "Influence of Water Immersion on the Single-Lap Shear Strength of Aluminum Joints Bonded with Aluminum-Powder-Filled Epoxy Adhesive," *Journal of Adhesion Science and Technology* **18**(15-16) (2004), pp. 1699-1710.

[116] A. K. Moidu, A. N. Sinclair, J. K. Spelt, "Adhesive Joint Durability Assessed Using Open-Faced Peel Specimens," *Journal of Adhesion* **65**(1-4) (1998), pp. 239-257.

[117] J. Cognard, "Influence of Water on the Cleavage of Adhesive Joints," *International Journal of Adhesion and Adhesives* **8**(2) (1998), pp. 93-9.

VITA

Kenneth Thomas Nathaniel Doering was born on June 4, 1986 in Albuquerque, NM. At a very young age, he moved to West St. Louis County where he lived until graduating high school. Upon graduation, he moved on to eventually earn a B.S. in Metallurgical Engineering from the University of Missouri – Rolla in December 2007. He then earned an M.S. in Metallurgical Engineering in May 2009 from the same school with a different name, Missouri University of Science and Technology.